

# THE BELL SYSTEM TECHNICAL JOURNAL

DEVOTED TO THE SCIENTIFIC AND ENGINEERING  
ASPECTS OF ELECTRICAL COMMUNICATION

Volume 55

December 1976

Number 10

Copyright © 1976, American Telephone and Telegraph Company. Printed in U.S.A.

## Steady-State Losses of Optical Fibers and Fiber Resonators

By D. MARCUSE

(Manuscript received May 24, 1976)

*We study the steady-state loss of a fiber with random, nearest-neighbor coupling and compare it with the mode with the lowest loss of a cavity formed from a section of the same type of fiber. We find that the loss of the cavity is not identical with the loss of the steady-state distribution of the fiber with random coupling. In fact, fiber and fiber resonator behave very differently if the fiber mode of highest order is made very lossy. The loss of the steady-state distribution of the fiber with random, nearest-neighbor coupling approaches a weighted average of the losses of its individual modes plus a contribution from the coupling coefficient that couples the highest-order mode to its neighbors. The cavity loss, on the other hand, becomes independent of the coupling coefficients and of the loss of the highest-order mode, provided this loss becomes much higher than the coupling strength. This behavior leads us to conclude that the loss of the cavity is a weighted average of the losses of all those modes whose coupling strength exceeds their (individual, uncoupled) loss coefficients. Two resonator modes with propagation constants  $\beta_1$  and  $\beta_2$  remain uncoupled unless they satisfy the condition  $\beta_1 - \beta_2 = 2\pi n/L$ , where  $n$  is an integer and  $L$  is twice the length of the resonator.*

### I. INTRODUCTION

We consider a multimode optical fiber with random imperfections. It is well-known that any type of imperfection built into a fiber causes coupling among its guided modes.<sup>1-3</sup> In a long fiber, the distribution of average power versus mode label approaches a steady state that

can be described by a steady-state loss coefficient and a unique distribution function.<sup>3</sup>

Now assume that we take a section of this fiber, place reflectors at either end, and observe the steady-state power distribution of this cavity. Without giving the matter much thought, we might expect the steady-state power distribution of the resonator to be identical to the steady-state power distribution of the long fiber. However, this is not the case. Mode coupling in a resonator has a very different effect on the steady-state power distribution and its loss coefficient than coupling in a long fiber. The reason for this difference in behavior is the fact that the wave traveling back and forth in the resonator experiences a periodic structure whose Fourier transform has a line spectrum. In a resonator of length  $L/2$ , two modes with propagation constants  $\beta_1$  and  $\beta_2$  are effectively coupled only if they satisfy the condition  $\beta_1 - \beta_2 = 2\pi n/L$ , where  $n$  is an integer. The losses and steady-state power distribution of the long fiber and the corresponding fiber resonator are very different. It is the purpose of this paper to clarify these differences.

We dramatize the difference of the fiber and the resonator by considering a fiber supporting only two guided modes. Furthermore, we assume that one of the two modes is relatively very lossy (in the absence of coupling), while the other mode has either no loss at all or very much lower loss. In a long fiber, the loss of the steady-state power distribution turns out to be the sum of the loss coefficient of the (uncoupled) low-loss mode plus the power-coupling coefficient of the two modes. This result is intuitively pleasing. It says that there are two independent loss mechanisms that reinforce each other additively—the loss of the first mode (in the absence of coupling to its high-loss companion) and the coupling of the low-loss mode to the high-loss mode. Since the high-loss mode carries practically no power, coupling of power to this mode appears directly as a loss coefficient.

Naively, it should be expected that the same behavior occurs in the fiber cavity. However, this is not true. In the resonator, the loss of the resonant field distribution is identical to the loss of the low-loss mode alone. Coupling between the two modes has no influence on the loss of the resonator, provided that the loss of the second mode is very high compared to the coupling coefficient. It is hard to understand this situation intuitively. In the periodic structure (the resonator), the field apparently manages to shape itself in such a way that it avoids carrying power in those regions that provide high loss. Since the structure is periodic, the field passes over the same region again and again, adjusting itself to the unfavorable loss situation. In the long fiber with random coupling, no such adjustment is possible. The

field does not have the chance to establish a normal mode and is confronted with a new, random-coupling situation in each section of the fiber. In this case, coupling to the high-loss mode simply subtracts power from the low-loss mode that is irretrievably lost.

The results presented in this paper are needed for the discussion of scattering losses in a fiber laser that is the subject of Ref. 4.

## II. TWO-MODE CASE

For a fiber supporting only two modes, the problem can be solved easily. We describe each mode by its amplitude coefficient  $a_1$  and  $a_2$ . The interaction of the two modes is described by the familiar coupled-wave equations<sup>5</sup> (self-coupling coefficients only modify the real parts of the propagation constants and are therefore omitted),

$$\frac{da_1}{dz} = -i\gamma_1 a_1 + K_{12} a_2 \quad (1)$$

$$\frac{da_2}{dz} = -i\gamma_2 a_2 + K_{21} a_1. \quad (2)$$

The complex propagation constants  $\gamma_{1,2}$  contain the loss coefficients  $\alpha_{1,2}$  of each mode in the absence of coupling,

$$\gamma_n = \beta_n - i\alpha_n \quad n = 1, 2. \quad (3)$$

The coupling coefficients obey the symmetry relation<sup>6</sup>

$$K_{21} = -K_{12}^*. \quad (4)$$

It is convenient to express the  $z$ -dependence of  $K_{12}$  explicitly ( $\hat{K}$  is real),

$$K_{12} = i\hat{K}f(z). \quad (5)$$

To first-order perturbation theory, it is only the Fourier component of  $f(z)$  at the spatial frequency  $\theta = \beta_1 - \beta_2$  that contributes to coupling between the modes.<sup>3</sup> This allows us to write (1) and (2) as

$$\frac{da_1}{dz} = -i\gamma_1 a_1 + i\hat{K}b a_2 e^{-i(\beta_1 - \beta_2)z} \quad (6)$$

$$\frac{da_2}{dz} = -i\gamma_2 a_2 + i\hat{K}b a_1 e^{i(\beta_1 - \beta_2)z}. \quad (7)$$

We have assumed that

$$f(z) = \sum_{\nu=1}^{\infty} 2b_{\nu} \cos \theta_{\nu} z, \quad \theta_{\nu} = \frac{2\pi}{L} \nu, \quad (8)$$

with real values of  $b_{\nu}$ , and have included in (6) and (7) only the terms in (8) that contribute to mode coupling, dropping the index on  $b_{\nu}$ .

We introduce new variables  $A_1$  and  $A_2$  by the definitions

$$a_1(z) = A_1(z)e^{-i(\beta_1 - \beta_2)z} \quad (9)$$

and

$$a_2(z) = A_2(z)e^{i(\beta_1 - \beta_2)z}, \quad (10)$$

and obtain, by substitution into (6) and (7),

$$\frac{dA_1}{dz} = -i\delta_1 A_1 + icA_2 \quad (11)$$

and

$$\frac{dA_2}{dz} = -i\delta_2 A_2 + icA_1, \quad (12)$$

with

$$\delta_n = \frac{1}{2}(\beta_1 + \beta_2) - i\alpha_n \quad n = 1, 2 \quad (13)$$

and

$$c = \hat{K}b. \quad (14)$$

Equations (11) and (12) represent two modes coupled by a constant-coupling coefficient. These equations are not exact representations of the starting equations (1) and (2), but they are good approximations. Comparison has been made of the results of this theory with the result of an exact theory of a two-mode model using a straight fiber with discrete offsets alternating periodically in opposite directions. The exact theory agrees with the approximation presented here, provided that the differential loss of the modes is small,

$$|\alpha_1 - \alpha_2| < \frac{4}{L}, \quad (15)$$

and that the following condition holds to an accuracy on the order of  $|\alpha_1 - \alpha_2|$ :

$$\beta_1 - \beta_2 = \frac{2\pi}{L} n, \quad (16)$$

with  $n$  indicating an integer. If (16) cannot be satisfied for any integer  $n$ , the two modes remain effectively uncoupled. Our derivation makes it clear that the coupling process is periodic with a period

$$L = n \frac{2\pi}{\beta_1 - \beta_2}. \quad (17)$$

A periodic structure of this type can be used to represent a resonant cavity. It is only necessary to envision the field traveling back and forth in the resonator; when we unfold the resonator of length  $L/2$ , the periodic structure results.

We now consider the normal modes of the coupled-equation system

(11) and (12) by asking for solutions of the type

$$A_n = B_n e^{-(i/2)(\beta_1 + \beta_2)z} e^{-\sigma z} \quad n = 1, 2, \quad (18)$$

with constant coefficients  $B_1$  and  $B_2$ . Substitution of (18) into (11) and (12) results in the equation system

$$(\sigma - \alpha_1)B_1 + icB_2 = 0 \quad (19)$$

and

$$icB_1 + (\sigma - \alpha_2)B_2 = 0. \quad (20)$$

The requirement that the determinant of the equation system (19) and (20) must vanish leads to the determination of the two eigenvalues,

$$\sigma^{(1)} = \frac{1}{2}(\alpha_1 + \alpha_2) - \frac{1}{2}\sqrt{(\alpha_2 - \alpha_1)^2 - 4c^2} \quad (21)$$

and

$$\sigma^{(2)} = \frac{1}{2}(\alpha_1 + \alpha_2) + \frac{1}{2}\sqrt{(\alpha_2 - \alpha_1)^2 - 4c^2}. \quad (22)$$

The amplitude coefficients can be expressed as

$$B_2^{(k)} = i \frac{\sigma^{(k)} - \alpha_1}{c} B_1^{(k)} \quad k = 1, 2. \quad (23)$$

The actual field amplitudes may now be expressed as a superposition of the two normal modes of the coupled system. Only the normal mode with the lower loss survives for  $z \rightarrow \infty$  so that the steady-state loss of the resonator is given by the eigenvalue (21).

It is interesting to distinguish two cases. For strong coupling,  $c \gg |\alpha_2 - \alpha_1|$ , we have, from (21),

$$\text{Re}(\sigma^{(1)}) = \frac{1}{2}(\alpha_1 + \alpha_2). \quad (24)$$

For weak coupling,  $c \ll |\alpha_2 - \alpha_1|$ , we have, instead,

$$\sigma^{(1)} \approx \alpha_1 + \frac{c^2}{\alpha_2 - \alpha_1}. \quad (25)$$

Next we consider the long fiber with two randomly coupled modes. It is possible to derive the solution for this case directly from the coupled wave equations (1) and (2). However, the same result is obtained from the corresponding coupled power equations<sup>8,7,8</sup> ( $P_n = \langle |a_n|^2 \rangle$ ),

$$\frac{dP_1}{dz} = -2\alpha_1 P_1 + h(P_2 - P_1) \quad (26)$$

and

$$\frac{dP_2}{dz} = -2\alpha_2 P_2 + h(P_1 - P_2). \quad (27)$$

The power coupling coefficient is<sup>8</sup>

$$h = K^2 \langle |F(\theta)|^2 \rangle, \quad (28)$$

with the Fourier transform of  $f(z)$  defined as<sup>3</sup>

$$F(\theta) = \frac{1}{\sqrt{L}} \int_0^L f(z) e^{i\theta z} dz = b\sqrt{L}. \quad (29)$$

The coefficient  $b$  is defined by (8) and (14) and  $L$  is the length of the periodic structure or twice the length of the resonator. According to (14), (28), and (29), the coupling coefficients  $c$  and  $h$  are thus related as

$$h = c^2 L. \quad (30)$$

A steady-state solution for the long fiber with random coupling is again obtained with the help of the trial solution,

$$P_n = Q_n e^{-2\rho z}. \quad (31)$$

We find, from (26) and (27),

$$\rho^{(1)} = \frac{1}{2}(\alpha_1 + \alpha_2 + h) - \frac{1}{2}\sqrt{(\alpha_2 - \alpha_1)^2 + h^2} \quad (32)$$

and

$$\rho^{(2)} = \frac{1}{2}(\alpha_1 + \alpha_2 + h) + \frac{1}{2}\sqrt{(\alpha_2 - \alpha_1)^2 + h^2}. \quad (33)$$

The smaller eigenvalue is the steady-state loss coefficient.<sup>3</sup> In the case of strong coupling,  $h \gg |\alpha_2 - \alpha_1|$ , we have, from (32),

$$\rho^{(1)} \approx \frac{1}{2}(\alpha_1 + \alpha_2) - \frac{(\alpha_2 - \alpha_1)^2}{4h}, \quad (34)$$

while we obtain, in the case of weak coupling,  $h \ll |\alpha_2 - \alpha_1|$ ,

$$\rho^{(1)} \approx \alpha_1 + \frac{1}{2}h - \frac{h^2}{4(\alpha_2 - \alpha_1)}. \quad (35)$$

The power coefficients are related in the following way:

$$Q_2 = \frac{h - 2\rho^{(1)} + 2\alpha_1}{h} Q_1. \quad (36)$$

### III. DISCUSSION OF THE TWO-MODE CASE

We are now ready to compare the steady-state losses of the long fiber and the fiber resonator. In case of strong coupling, we have approximately

$$\sigma^{(1)} = \frac{1}{2}(\alpha_1 + \alpha_2) \quad (37a)$$

for the resonator and

$$\rho^{(1)} = \frac{1}{2}(\alpha_1 + \alpha_2) \quad (37b)$$

for the long fiber. Strong coupling ties the two modes together so effectively that the steady-state losses are equal to the average losses of the uncoupled modes in either case. From (21) and (23), we find

$B_2 = B_1$  and from (36)  $Q_2 = Q_1$  if the coupling coefficients are very much larger than the loss coefficients. We thus see that both modes carry equal amounts of power in the strong coupling case. There is no difference in loss behavior between the resonator and long fiber if the coupling is strong.

The situation changes for weak coupling. From (25), we have in the limit  $c^2/\alpha_2 \rightarrow 0$  for the resonator

$$\sigma^{(1)} = \alpha_1, \quad (38)$$

while (35) yields for the long fiber

$$\rho^{(1)} = \alpha_1 + \frac{1}{2}h. \quad (39)$$

In the resonator, coupling to a relatively lossy mode has no effect on the loss of the steady-state field distribution. The solution of the exactly solvable model shows that this is true even if (15) and (16) are not satisfied. The resonator loss becomes equal to the loss of the low-loss mode as though coupling were absent. In the fiber with random coupling, (39) shows that the steady-state loss is equal to the sum of the inherent loss of the low-loss mode plus half the power coupling coefficient. Coupling to the high-loss mode thus expresses itself directly as a loss factor. The power ratios of the two modes are also of interest. From (23), (25), and (30), we find for the weak coupling (or high-loss) resonator case

$$\left| \frac{B_2}{B_1} \right|^2 = \frac{h}{4(\alpha_2 - \alpha_1)} \frac{4}{(\alpha_2 - \alpha_1)L}. \quad (40)$$

For the randomly coupled fiber we obtain, from (35) and (36),

$$\frac{Q_2}{Q_1} = \frac{h}{4(\alpha_2 - \alpha_1)}. \quad (41)$$

#### IV. THE MULTIMODE CASE

We have seen in the section on the two-mode case that we may consider coupled wave equations with constant coupling coefficients if we suitably redefine the mode amplitudes. In addition, we shall assume that only modes that are nearest neighbors are coupled in the resonator or long fiber. This assumption is justified by the observation that the Fourier components of the coupling function  $f(z)$  tend to drop off very rapidly with increasing spatial frequencies so that coupling of modes that are not nearest neighbors (such coupling is caused by Fourier components with higher spatial frequencies) is much weaker than nearest-neighbor coupling. In addition only modes satisfying (16) are coupled to each other. Consider the coupled equa-

tion system,

$$\frac{dA_\nu}{dz} = -i\gamma_\nu A_\nu + K_{\nu,\nu-1}A_{\nu-1} + K_{\nu,\nu+1}A_{\nu+1} \quad \nu = 1, 2, \dots, N. \quad (42)$$

We have shown for the two-mode case that we may assume the real parts of all  $\gamma_\nu$ s are identical,

$$\gamma_\nu = \beta - i\alpha_\nu. \quad (43)$$

A normal mode solution of (42) is obtained with the help of the trial solution,

$$A_\nu = B_\nu e^{-i\beta z} e^{-\alpha_\nu z}. \quad (44)$$

Substitution of (44) into (42) results in a homogeneous algebraic equation system whose determinant must vanish. For  $N = 6$ , the determinantal equation assumes the form

$$\begin{vmatrix} \alpha_1 - \alpha & -K_1 & 0 & 0 & 0 & 0 \\ K_1 & \alpha_2 - \alpha & -K_2 & 0 & 0 & 0 \\ 0 & K_2 & \alpha_3 - \alpha & -K_3 & 0 & 0 \\ 0 & 0 & K_3 & \alpha_4 - \alpha & -K_4 & 0 \\ 0 & 0 & 0 & K_4 & \alpha_5 - \alpha & -K_5 \\ 0 & 0 & 0 & 0 & K_5 & \alpha_6 - \alpha \end{vmatrix} = 0. \quad (45)$$

For strong coupling with  $K_\nu \gg \alpha_\mu$ ;  $\nu, \mu = 1, 2, \dots, 5$  but  $\alpha_6 \gg \alpha_\nu$  and  $\alpha_6 \gg K_\nu$ , the smallest real root of this equation may be approximated by

$$\alpha = \frac{\alpha_1 K_2^2 K_4^2 + \alpha_3 K_1^2 K_4^2 + \alpha_5 K_1^2 K_3^2 + K_1^2 K_3^2 K_5^2 / (\alpha_6 - \alpha_1)}{K_2^2 K_4^2 + K_1^2 K_4^2 + K_1^2 K_3^2}. \quad (46)$$

We have assumed that the guided mode of highest order,  $\nu = 6$  in this case, is coupled very strongly to the radiation modes so that its loss coefficient is much larger than that of all the other guided modes and also larger than the coupling coefficients among the guided modes. This assumption is usually made in the analysis of fibers with many coupled guided modes.<sup>3</sup> For the special case  $K_1 = K_2 = \dots = K_5 = \text{const.}$ , (46) simplifies to

$$\alpha = \frac{1}{3}(\alpha_1 + \alpha_3 + \alpha_5) + \frac{K^2}{3(\alpha_6 - \alpha_1)}. \quad (47)$$

For weak coupling,  $K_\nu \ll \alpha_\mu$ , we have the approximation

$$\alpha = \alpha_1 + \frac{K_1^2}{\alpha_2 - \alpha_1}. \quad (48)$$

Here we assumed that  $\alpha_1 < \alpha_2 < \dots < \alpha_6$ , in this case, (48) represents the smallest solution of (45).

The corresponding coupled power equations may be expressed in the form

$$\frac{dP_\nu}{dz} = -(2\alpha_\nu + h_{\nu-1} + h_\nu)P_\nu + h_{\nu-1}P_{\nu-1} + h_\nu P_{\nu+1}. \quad (49)$$

The trial solution

$$P_\nu = e^{-2\alpha z} Q_\nu \quad (50)$$

leads to the algebraic equation system

$$(2\alpha_\nu + h_{\nu-1} + h_\nu - 2\alpha)Q_\nu - h_{\nu-1}Q_{\nu-1} - h_\nu Q_{\nu+1} = 0. \quad (51)$$

The eigenvalue  $\alpha$  is obtained as the solution of a determinantal equation which, for six modes, assumes the form

$$\begin{vmatrix} (2\alpha_1 + h_1 - 2\alpha) & -h_1 & 0 & 0 & 0 & 0 \\ -h_1 & (2\alpha_2 + h_2 + h_1 - 2\alpha) & -h_2 & 0 & 0 & 0 \\ 0 & -h_2 & (2\alpha_3 + h_3 + h_2 - 2\alpha) & -h_3 & 0 & 0 \\ 0 & 0 & -h_3 & (2\alpha_4 + h_4 + h_3 - 2\alpha) & -h_4 & 0 \\ 0 & 0 & 0 & -h_4 & (2\alpha_5 + h_5 + h_4 - 2\alpha) & -h_5 \\ 0 & 0 & 0 & 0 & -h_5 & (2\alpha_6 + h_6 - 2\alpha) \end{vmatrix} = 0. \quad (52)$$

For strong coupling (in the sense used in the cavity case), we obtain the following approximation from (52) in the special case  $h_\nu = h = \text{const.}$ ,

$$\alpha = \frac{1}{15} (5\alpha_1 + 4\alpha_2 + 3\alpha_3 + 2\alpha_4 + \alpha_5) + \frac{h}{30} - \frac{h^2}{60\alpha_6}. \quad (53)$$

For weak coupling we find

$$\alpha = \alpha_1 + \frac{1}{2}h_1. \quad (54)$$

## V. DISCUSSION OF THE MULTIMODE CASE

If we consider that the losses  $\alpha_\nu$  are caused by random coupling between guided modes and radiation modes, we may assume the following dependence<sup>9,10</sup> on the mode label  $\nu$ :

$$\alpha_\nu = \alpha_1 \nu^2. \quad (55)$$

If the Fourier amplitudes  $b_\nu$  in (8) were independent of the spatial frequency, we would have<sup>3</sup>

$$K_\nu = K_1 \nu^2 \quad \text{and} \quad h_\nu = h_1 \nu^4. \quad (56)$$

However, the assumption of nearest-neighbor coupling becomes questionable in this case. It is natural to consider the case

$$K_\nu = K_1 = \text{const.} \quad \text{and} \quad h_\nu = h_1 = \text{const.}, \quad (57)$$

and in our discussion of numerical examples we also include the case of decreasing coupling strength between neighboring modes of higher

order,

$$K_\nu = \frac{K_1}{\nu} \quad \text{and} \quad h_\nu = \frac{h_1}{\nu^2}. \quad (58)$$

Numerical solutions of the eigenvalue equations (45) and (52) were obtained by computer. The relation between the coupling coefficients  $K_\nu$  and  $h_\nu$  is given by (30):

$$h_\nu = LK_\nu^2, \quad (59)$$

but for the purpose of comparing the long fiber with the fiber resonator it seems more realistic to choose instead

$$K_1 = \frac{1}{2}h_1, \quad (60)$$

because this choice yields the same ratios of coupling coefficients to attenuation coefficient for mode 1 and mode 2 according to (45) and (52).

Table I lists numerical values of the lowest eigenvalues of (45) and (52). It was found that, for strong coupling with  $K_\nu = \text{const.}$ , the lowest eigenvalue of (45) is of the form

$$\alpha = \alpha_r \pm i\alpha_i. \quad (61)$$

The imaginary part of this expression is simply a correction to the propagation constant of the normal mode solution, while the real part has the meaning of the loss of the normal mode of the cavity. However, since the solutions of the cavity loss coefficients are not real, our approximate solution (46) does not apply because the approximation (46) yields the smallest real eigenvalue of (45).

Table I shows that (with two exceptions) the cavity losses are generally lower than the losses of the corresponding fiber with random coupling. This fact is in agreement with the two-mode case. Furthermore, the numbers in the table show that an increase of the loss of mode 6 increases the steady-state loss of the fiber with random mode coupling while it decreases the loss of the fiber cavity. This behavior is in qualitative agreement with approximate formulas (47) and (53). In addition to the exact solutions of eigenvalue equations (45) and (52), Table I also contains entries for the approximate solutions obtained from one of the appropriate formulas (46), (47), (48), (53), or (54). In comparing the approximate and exact solutions for the cavity, we must remember that approximations (46) and (47) do not necessarily yield the eigenvalue with the lowest numerical value. In fact, only for the case  $K_\nu = K_1\nu^2$  and for small values of  $K_\nu = K_1 \ll \alpha$ , do the approximations apply to the solution with the lowest loss. However, comparison of the exact and approximate values in Table I makes it apparent that the approximation provides a

Table I—Loss values of the cavity mode with lowest loss and steady-state loss of the corresponding fiber with random coupling. Exact solutions of eigenvalue equations (45) and (52) are compared with approximate solutions

$h_\nu$	$K_\nu$	$\lambda K_1$	$\alpha_6$	$\alpha\lambda$			
				Exact		Approximate	
				Cavity	Fiber	Cavity	Fiber
$h_{1\nu^4}$	$K_{1\nu^2}$	$10^{-5}$	$\alpha_6 6^2$ $\alpha_5 10^3$	$4.484 \times 10^{-5}$ $1.923 \times 10^{-5}$	$8.626 \times 10^{-5}$ $1.022 \times 10^{-5}$	$1.95 \times 10^{-5}$	
$h_{1/\nu}$	$K_{1/\nu}$	$10^{-5}$	$\alpha_5 10^3$	$3.223 \times 10^{-5}$	$3.129 \times 10^{-5}$	$1.77 \times 10^{-5}$	
$h_1$	$K_1$	$10^{-7}$	$\alpha_5 10^3$	$1.003 \times 10^{-5}$	$1.097 \times 10^{-5}$	$1.00 \times 10^{-5}$	$1.10 \times 10^{-5}$
$h_1$	$K_1$	$10^{-6}$	$\alpha_5 10^3$	$1.361 \times 10^{-5}$	$1.758 \times 10^{-5}$	$1.00 \times 10^{-5}$	$2.00 \times 10^{-5}$
$h_1$	$K_1$	$10^{-5}$	$\alpha_6 6^2$ $\alpha_5 10^3$	$6.383 \times 10^{-5}$ $6.415 \times 10^{-5}$	$4.321 \times 10^{-5}$ $4.322 \times 10^{-5}$	$1.17 \times 10^{-5}$	$7.67 \times 10^{-5}$
$h_1$	$K_1$	$10^{-4}$	$\alpha_5 10^3$	$1.015 \times 10^{-5}$	$1.347 \times 10^{-5}$	$1.17 \times 10^{-5}$	$1.37 \times 10^{-5}$
$h_1$	$K_1$	$10^{-3}$	$\alpha_5 10^3$	$1.017 \times 10^{-5}$	$8.681 \times 10^{-5}$	$1.17 \times 10^{-5}$	$7.37 \times 10^{-5}$
$h_1$	$K_1$	$10^{-2}$	$\alpha_5 10^3$ $\alpha_5 10^3$	$1.050 \times 10^{-5}$ $2.931 \times 10^{-4}$	$8.159 \times 10^{-4}$ $7.112 \times 10^{-4}$	$1.30 \times 10^{-5}$	$6.73 \times 10^{-4}$

Note:  $\alpha_\nu = \alpha_{1\nu^2}$ ,  $\alpha_1 = 10^{-6}/\lambda$ ,  $K_1 = \frac{1}{2}h_1$ , and  $\nu \neq 6$ .

reasonable order-of-magnitude estimate of the loss values of the cavity modes and gives at least an upper bound to the exact values.

The approximate solutions for the fiber case with randomly coupled modes do apply to the solution with the lowest loss. Comparison of the exact and approximate values in Table I show that the approximations (53) and (54) are not very precise but again may be regarded as order-of-magnitude estimates.

Table II shows the complete solution of the eigenvalue equation (45) for the fiber cavity for a typical case:  $K_\nu = K_1 = 10^{-4}/\lambda$ ,  $\alpha_1 = 10^{-6}/\lambda$ ,  $\alpha_\nu = \alpha_{1\nu^2}$ ,  $\alpha_6 = \alpha_5 10^3$ . As in all cases with  $K_\nu = K_1 \gg \alpha_\nu$ ,

Table II—Complete solution of eigenvalue equation of the fiber cavity (45) for a particular case and comparison of the exact solution to approximation (47)

$i$	$\alpha_r$	$\alpha_i$	$\alpha_{\text{appr}}$
1	$1.018 \times 10^{-6}$	$1.726 \times 10^{-4}$	$1.180 \times 10^{-5}$
2	$1.018 \times 10^{-6}$	$-1.726 \times 10^{-4}$	
3	$1.162 \times 10^{-6}$	$1.001 \times 10^{-4}$	
4	$1.162 \times 10^{-6}$	$-1.001 \times 10^{-4}$	
5	$1.180 \times 10^{-6}$	0.0	
6	$2.500 \times 10^{-2}$	0.0	

Note:  $K_\nu = K_1 = 10^{-4}/\lambda$ ,  $\alpha_\nu = \alpha_{1\nu^2}$ ,  $\alpha_1 = 10^{-6}/\lambda$ , and  $\alpha_6 = \alpha_5 10^3 = 2.5 \times 10^{-2}$ .

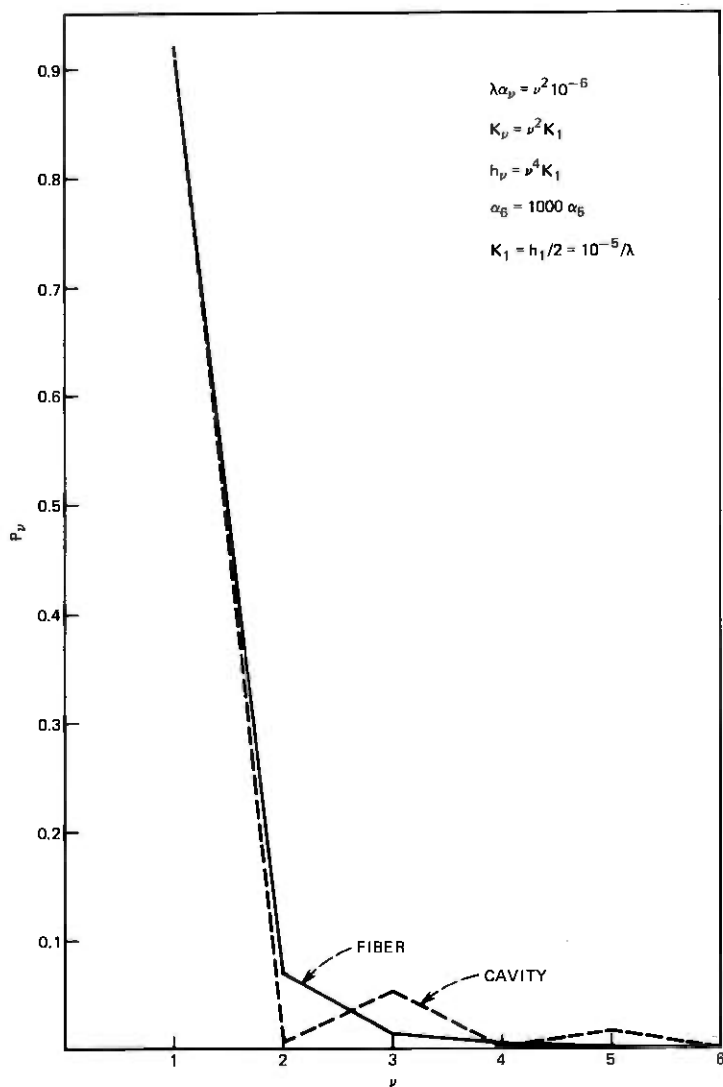


Fig. 1—Normalized power versus mode number distribution for the case of a fiber with random coupling (solid line) and the lowest loss mode of the fiber cavity (dotted line).  $K_\nu = K_1 \nu^2$ ,  $h_\nu = h_1 \nu^4$ ,  $K_1 = 0.5 h_1 = 10^{-6}/\lambda$ ,  $\alpha_\nu = \alpha_1 \nu^2$  with  $\alpha_1 = 10^{-6}/\lambda$ ,  $\alpha_6 = 1000 \alpha_5$ .

$\mu < 6$ , there are two sets of complex, conjugate solutions and two single, real solutions. Approximation (47) yields the smallest of the real solutions to a remarkable accuracy.

It is interesting to compare the distribution of power versus mode number for the cavity and fiber cases. Figure 1 (and all subsequent

figures) shows the normalized power  $P$ , as a function of the mode label  $\nu$ . For Fig. 1 we used  $K_\nu = K_1\nu^2$  for the fiber cavity and  $h_\nu = h_1\nu^4$  for the fiber with random-mode coupling with  $K_1 = h_1/2 = 10^{-5}/\lambda$ . This and all the other figures were computed with  $\alpha_\nu = 10^{-6}\nu^2/\lambda$ , for  $\nu = 1, 2, \dots, 5$ . In Fig. 1 we assumed  $\alpha_6 = \alpha_5 10^3$ . Even though the coupling strength is increasing for nearest neighbors with increasing mode number, mode 1 carries by far the most power. Of course, we have only plotted the power distribution for the mode with the lowest loss. In the cavity case, there are solutions with the maximum power in any one of the six modes. The coupled power problem of the fiber with random coupling also has six different solutions. However, only the solutions with the lowest loss value have physical significance<sup>3</sup> as the steady-state power distribution. This solution is shown in Fig. 1 and the subsequent figures.

Figure 2 was drawn for almost the same condition as Fig. 1, except that we used the law  $\alpha_\nu = \alpha_1\nu^2$  for all six values of  $\nu$ . This has the consequence that the loss of the mode of highest order,  $\nu = 6$ , is now much lower than in Fig. 1 so that more power is carried by the higher-order modes.

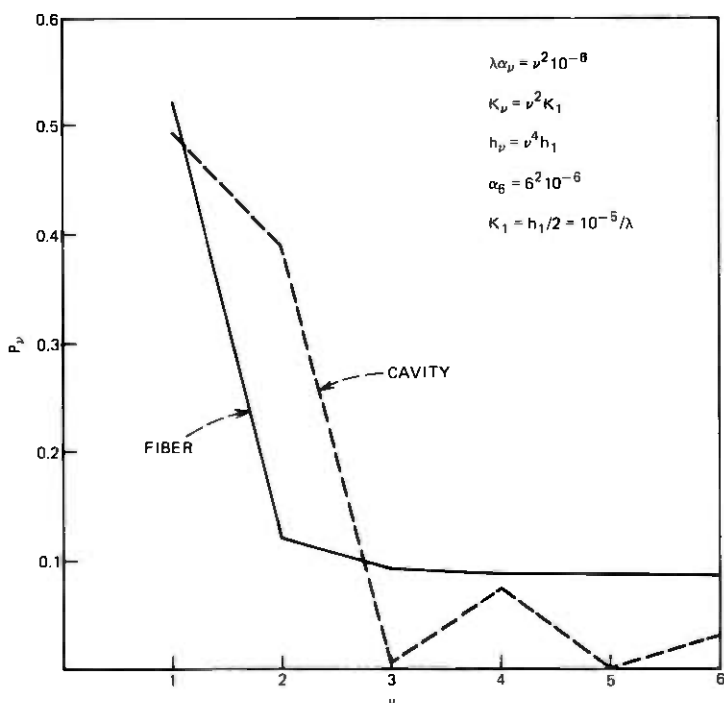


Fig. 2—Same as Fig. 1 but with  $\alpha_6 = \alpha_1 6^2$ .

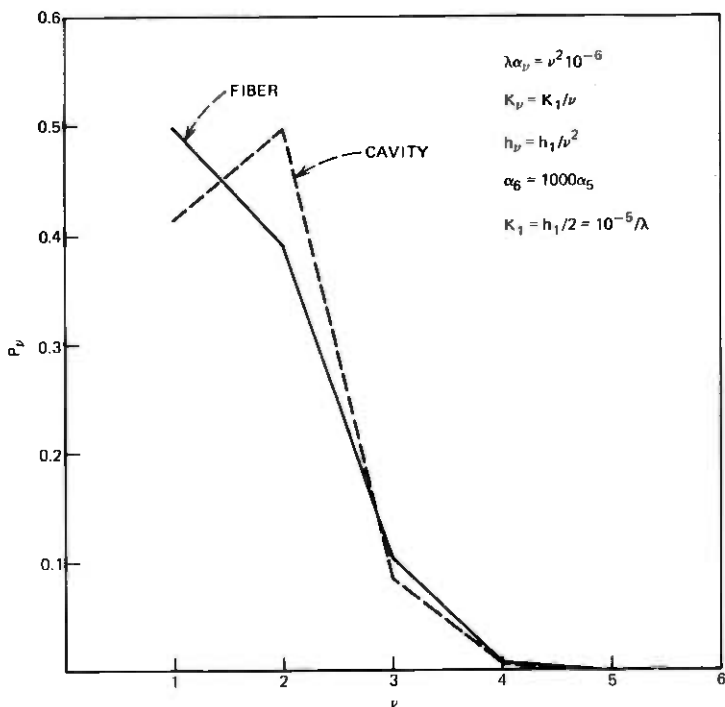


Fig. 3—Same as Fig. 1 but with  $K_n = K_1/\nu$ .

Figure 3 applies to the case  $K_n = K_1/\nu$ ,  $h_n = h_1/\nu^2$ , with  $K_1 = h_1/2 = 10^{-5}/\lambda$ . Contrary to the cases in Figs. 1 and 2, the coupling strength is now decreasing with increasing mode number. It is interesting to observe that the cavity as well as the fiber with random coupling now carries more power in modes 2 and 3. The cavity solution with the least loss now has higher loss than in the case in Fig. 1 (see Table I). The loss of the steady-state power distribution of the fiber is, however, reduced compared to the case in Fig. 1 (again see Table I).

The remaining Figs. 4 through 7 describe the case of constant coupling,  $K_n = K_1$  with different values of  $K_1$  and  $\alpha_6$ . We see that for very weak coupling most power resides in the modes with the lowest loss,  $\nu = 1$ . As the coupling strength is increased, more power is carried in higher-order modes. If we did not insist on making the last mode ( $\nu = 6$ ) very lossy, there would be equal power in all the modes of the fiber with random coupling. It is interesting to observe that there is a saturation effect; comparison of Figs. 6 and 7 shows that the power distribution remains unchanged for a further increase of the coupling strength. Another interesting phenomenon is the different shape of the power distribution for the cavity mode with the lowest

loss and the steady-state power distribution in the fiber with random coupling. Naively, one may have expected that the steady-state power distribution of the fiber would also apply to the cavity case. Figures 5 through 7 show that this is not the case. In spite of the fact that the cavity carries more power in the higher-order modes, Table I shows that the cavity losses are generally lower than the fiber losses. The cavity loss becomes high only when the highest-order mode has relatively low loss.

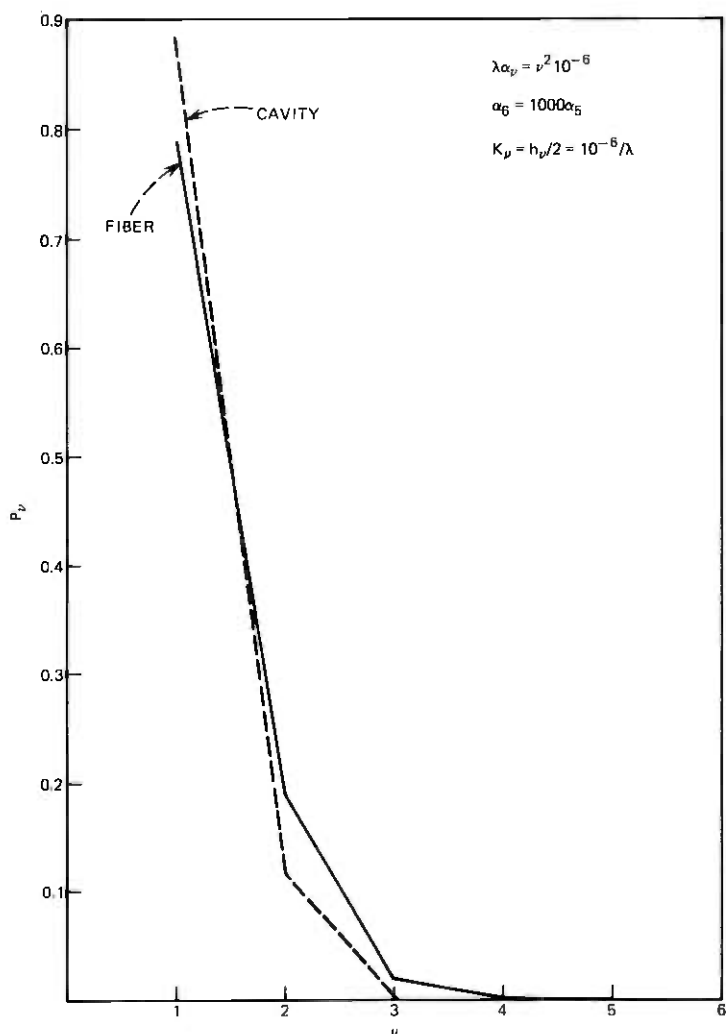


Fig. 4—Same as Fig. 1 but with  $K_\nu = K_1$ ,  $h_\nu = h_1$ ,  $K_1 = 0.5h_1 = 10^{-6}/\lambda$ .

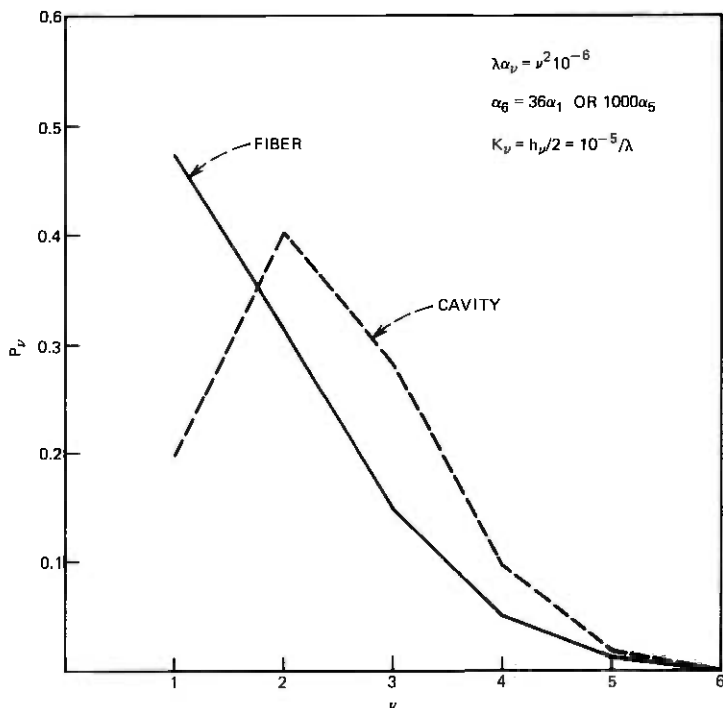


Fig. 5—Same as Fig. 4 but with  $K_1 = 0.5\lambda_1 = 10^{-5}/\lambda$ . These curves are practically independent of the loss value of  $\alpha_6$ ; the curves for  $\alpha_6 = 36\alpha_1$  and  $\alpha_6 = 1000\alpha_5$  are indistinguishable on the scale of this figure.

## VI. CONCLUSIONS

We have compared the losses and power distribution of a fiber with random coupling and of a cavity made of a section of the same fiber. We have shown that these two systems behave quite differently. While the losses of the fiber increase with an increase of the loss of the highest-order mode, the cavity losses decrease as the loss of the highest-order mode approaches infinity. This behavior has been studied with the help of exact numerical solutions of the eigenvalue equations of these systems for six modes and is also apparent from approximate solutions.

We may generalize our results for the fiber cavity as follows. We have seen that the losses of the solution with the lowest eigenvalue are higher than the loss of the lowest-order (uncoupled) mode. The approximate formula (46) or (47) shows that the cavity loss is an average of the losses of the individual, uncoupled modes. However, the last mode,  $\nu = 6$  in our examples, did not participate in this average since its loss far exceeded the coupling strength. This behavior

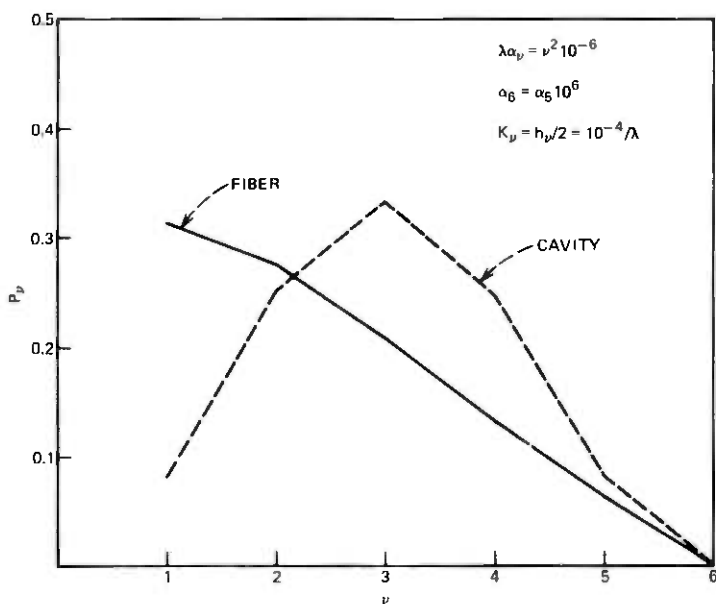


Fig. 6—Same as Fig. 4 but with  $K_1 = 0.5h_1 = 10^{-4}/\lambda$  and  $\alpha_6 = \alpha_5 10^6$ .

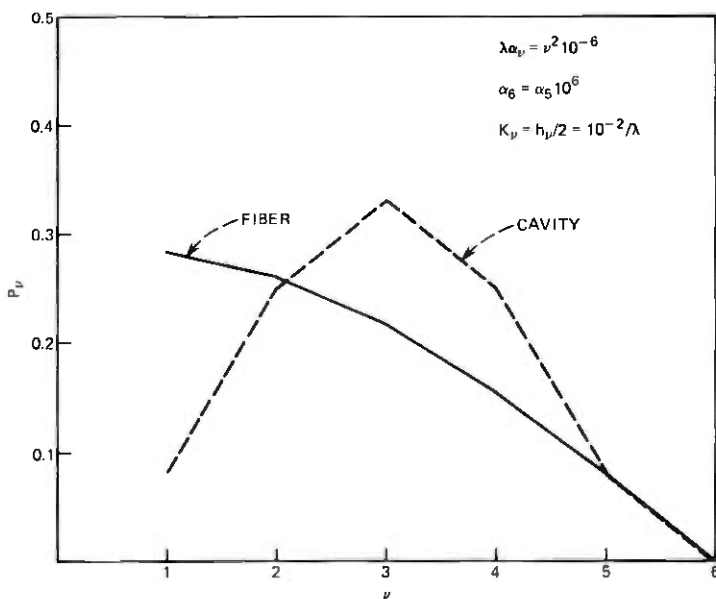


Fig. 7—Same as Fig. 6 but with  $K_1 = 0.5h_1 = 10^{-2}/\lambda$ .

leads us to conclude that the cavity losses are the average of the mode losses of all those modes whose (uncoupled) loss values are less than the coupling strength of neighboring modes. Modes whose losses exceed the coupling strength do not contribute appreciably to the cavity loss.

We have also indicated that two modes are coupled only if their propagation constants satisfy relation (16). The likelihood that this happens increases with increasing resonator length. In very short resonators, most modes remain effectively uncoupled just because they fail to satisfy condition (16). In long resonators, more modes have a chance to satisfy the additional coupling condition (16), but even here effective coupling ceases for modes whose losses exceed the coupling strength.

## VII. ACKNOWLEDGMENT

E. A. J. Marcatili contributed to this paper by asking the right questions and through several helpful discussions.

## REFERENCES

1. A. W. Snyder, "Excitation and Scattering of Modes on a Dielectric or Optical Fiber," *IEEE Trans. Microw. Theory Tech.*, *MTT-17*, No. 12 (December 1969), pp. 1138-1144.
2. A. W. Snyder, "Coupled Mode Theory for Optical Fibers," *J. Opt. Soc. Am.*, *62*, No. 11 (November 1972), pp. 1267-1277.
3. D. Marcuse, *Theory of Dielectric Optical Waveguides*, New York: Academic Press, 1974.
4. D. Marcuse, "Scattering and Absorption Losses of Multimode Optical Fibers and Fiber Lasers," *B.S.T.J.*, this issue, pp. 1463-1488.
5. S. E. Miller, "Coupled Wave Theory and Waveguide Applications," *B.S.T.J.*, *33*, No. 3 (May 1954), pp. 661-720.
6. Ref. 3, p. 179, eq. (5.2-17).
7. D. T. Young, "Model Relating Coupled Power Equations to Coupled Amplitude Equations," *B.S.T.J.*, *42*, No. 9 (November 1963), pp. 2761-2764.
8. H. E. Rowe and D. T. Young, "Transmission Distortion in Multimode Random Waveguides," *IEEE Trans. Microw. Theory Tech.*, *MTT-20*, No. 6 (June 1972), pp. 349-365.
9. Ref. 3, p. 138, eq. (4.2-25).
10. D. Marcuse, "Power Distribution and Radiation Losses in Multimode Dielectric Slab Waveguides," *B.S.T.J.*, *51*, No. 2 (February 1972), pp. 429-454.

# Scattering and Absorption Losses of Multimode Optical Fibers and Fiber Lasers

By D. MARCUSE

(Manuscript received May 24, 1976)

*We present an approximate theory of loss coefficients for modes of step-index fibers with various types of distortions and for fibers with lossy claddings. The fiber irregularities are assumed to be sinusoidal and random variations of the core-cladding interface. Formulas for the loss coefficients are presented and plotted for different values of the compound mode number  $M$ . For fiber lasers, we plot the loss coefficients as functions of the mirror tilt angles.*

*We consider as an example a Nd-YAG fiber laser with refractive index  $n_1 = 1.8$  and a core radius of  $a = 40 \mu\text{m}$  operating at a wavelength of  $\lambda = 1.06 \mu\text{m}$ . For this example, we find that radiation losses are caused by Fourier components of fiber irregularities in the spatial wavelength range between  $0.4$  and  $1.3 \mu\text{m}$ . Intrinsic losses may be as low as  $2\alpha = 10^{-3} \text{cm}^{-1}$ . It is thus desirable to limit scattering losses to values below  $10^{-3} \text{cm}^{-1}$ . This requirement imposes tolerance restrictions of  $0.01 \mu\text{m}$  on the permissible core radius fluctuations. For core radius fluctuations of this order of magnitude, mirror tilts should not exceed approximately 5 degrees. Cladding losses are not critical, but their influence on laser losses depends on the refractive index ratio of the core and cladding materials. Tolerable cladding losses may range from  $10$  to  $300 \text{cm}^{-1}$ .*

## I. INTRODUCTION

A cavity laser consists of an active medium that provides the required gain and a (usually open) external cavity furnishing the feedback for laser operation. A fiber laser also has gain and feedback, but instead of using the resonant modes of an open cavity it employs an optical fiber for guiding the radiation back and forth between the set of mirrors forming the cavity.<sup>1,2</sup> A fiber laser thus might be much narrower than a cavity laser since it need not allow space for the diffraction-limited beam to spread out in transverse direction. The width of the fiber laser is limited only by the loss of the fiber waveguide, which increases with decreasing fiber diameter.

In this paper we calculate the mode losses of step-index fibers and use them to estimate the losses of fiber lasers. The losses are caused by scattering from the rough fiber wall and by the presence of a lossy cladding. Figure 1 shows a schematic of the fiber laser. We assume that plane mirrors are placed at the end of the fiber that also contains the gain mechanism for the laser. Figure 1a shows a fiber laser with plane mirrors positioned exactly perpendicular to the fiber axis, whereas Fig. 1b shows a laser with slightly tilted mirrors so that the wave inside the fiber, indicated schematically by a light ray, interacts more strongly with the fiber wall. For simplicity, we assume that the mirrors and the medium inside the fiber do not cause scattering and that only the fiber walls are slightly rough. We also assume that the fiber is surrounded by a lossy cladding that causes power loss via the evanescent field tail of the guided wave penetrating into the cladding. However, we consider these various loss mechanisms separately, one at a time.

It is important to realize that wall roughness or other geometrical imperfections of the fiber geometry or inhomogeneities in the fiber material do not necessarily cause resonator losses. The electromagnetic field inside the cavity adjusts itself to any geometry and forms a normal mode. This normal mode of the cavity can be described as a superposition of coupled modes of the perfect waveguide. Henceforth, we shall refer to modes of the perfect structure as ideal modes or as perfect modes. The fiber imperfections provide the mechanism that

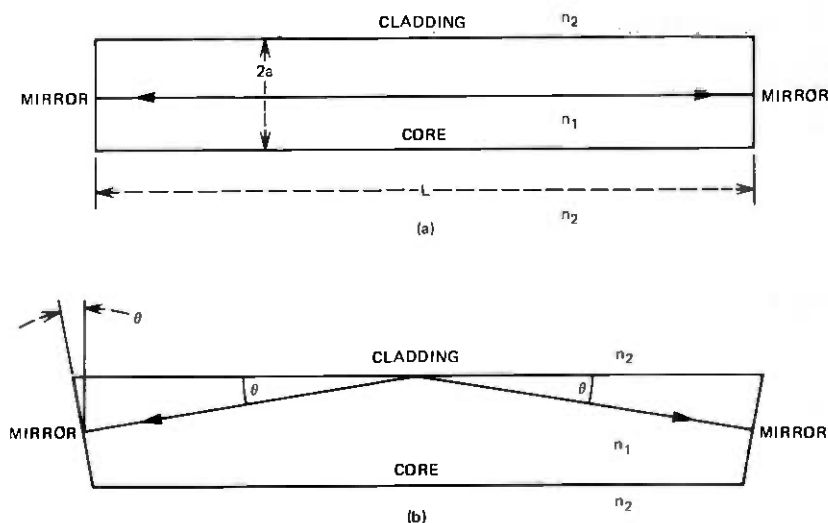


Fig. 1—Schematic of the fiber laser with (a) perpendicular mirrors and (b) tilted mirrors.

couples the perfect modes together. Coupling among the guided modes does not introduce losses by itself. However, the perfect modes of the fiber suffer losses individually (in the absence of coupling). These losses are either caused by dissipative mechanisms in the fiber core or in its cladding, or they may be caused by fiber imperfections on a scale different from those that couple the guided modes. We may assume that imperfections with Fourier components of high spatial frequencies couple each ideal fiber mode to the radiation field outside the fiber and act as a loss mechanism. In addition, there will probably be imperfections with large amplitudes but with low spatial frequencies that couple the ideal modes to each other.

In a companion paper<sup>3</sup> we discuss the influence of mode coupling on the losses of the normal modes of the fiber cavity. We found that coupling among these modes increases the cavity losses compared to the losses of the lowest-order ideal fiber mode because neighboring modes with higher losses take part in the superposition field that forms the cavity mode. We also found that strongly coupled modes result in a normal mode of the cavity whose loss is an average of the losses of the participating coupled modes. However, not all the ideal modes of the fiber take part in forming the normal mode of the fiber cavity. Modes whose individual losses (radiation losses as well as dissipation losses) are relatively higher than the coupling strength to neighboring guided modes do not take part in the loss-averaging process. Since the losses of the ideal fiber modes tend to increase in proportion to the square of their (compound) mode number, modes of high order are, of necessity, much lossier than modes of low order. On the other hand, it is expected that the coupling strength of neighboring guided modes decreases with mode number. Consequently, only modes with relatively low mode numbers participate in forming the normal modes of the cavity.

This theoretical expectation is confirmed by observation of laser radiation.<sup>2</sup> In fibers supporting a very large number of guided modes, only the modes of low order are excited as laser modes. Laser modes are identical with the normal modes of the resonant fiber cavity. It is thus clear that the loss of the normal mode of the laser (or fiber cavity) is an average value of the losses of the ideal modes that take part in forming the normal mode of the cavity. If only a very few fiber modes are taking part in forming the lasing mode, the loss (in the absence of pumping) of this cavity mode is simply the average loss of the few fiber modes that are effectively coupled to each other. In the presence of coupling among the guided modes, the loss of the resulting laser mode is thus somewhat higher than the loss coefficient of the fiber mode of lowest order, but mode coupling, even if strong

for the lowest-order fiber mode and its neighbor, does not increase the loss of the laser mode dramatically. The example studied in Ref. 3 suggests that the loss of the laser mode may be at most an order of magnitude higher than the loss of the fiber mode of lowest order. We found, furthermore, that two modes with propagation constants  $\beta_1$  and  $\beta_2$  can couple effectively only if the relation  $\beta_1 - \beta_2 = 2n\pi/L$  holds to an accuracy on the order of  $|\alpha_1 - \alpha_2|$ , where  $\alpha$  indicates the loss coefficient,  $n$  is an integer, and  $L/2$  is the resonator length.

So far, we have assumed that the mirrors at the end of the fiber resonator are perfectly perpendicular to the fiber axis. Mirror tilt can be taken into account in the following way. Consider a light ray that propagates parallel to the fiber axis and strikes the tilted mirror of the resonator. After reflection, the ray impinges on the fiber wall at an angle that is twice the angle of the mirror tilt. Because scattering losses are proportional to the square of the angle between the incident ray and the fiber wall, it is clear that this ray, which originally traveled parallel to the fiber axis, suffers relatively high scattering loss. On the other hand, a ray that strikes the tilted mirror at normal incidence will strike the fiber wall at the mirror tilt angle shown in Fig. 1b. Such a ray suffers less scattering loss. In fact, it would appear that the mirror tilt angle is the minimum angle at which rays passing back and forth through the cavity may strike the fiber wall. It is not obvious that there should be a ray path that closes on itself and still impinges at the tilted mirror at normal incidence. But the normal mode of a resonator has the tendency to minimize its losses. It will thus be composed of rays that make the lowest possible angle with the rough fiber walls. Consequently, we shall assume that the field in the resonator strikes the fiber wall at the mirror tilt angle. Instead of computing mode losses, we use the scattering losses of waves impinging on the rough dielectric interface at the mirror tilt angle to calculate the loss of a cavity with tilted mirrors. If both mirrors are tilted differently, the larger of the two angles should be used.

We limit our discussion to fibers whose diameter is much larger than the wavelength of the radiation inside the fiber core. This assumption permits us to use a pseudo-plane-wave analysis. For simplicity, it is furthermore assumed that the refractive index difference between core and cladding material is so slight that reflectivity differences caused by polarization can be ignored; TE and TM modes thus have the same losses. When we violate this assumption in some of our examples, it should be remembered that our loss values apply to TE polarization.

Several types of wall roughness will be considered. The simplest imperfection is a sinusoidal variation of the fiber radius. A more com-

plicated wall distortion preserves the circular shape of the fiber but allows the diameter to vary randomly as a function of the longitudinal  $z$  coordinate. Finally, we consider a type of wall roughness that assumes that the Fourier spectrum of the wall distortion function is constant over all spatial frequencies of interest and that variations occur in both dimensions on the fiber surface with certain short correlation lengths. Scattering losses are expressed as functions of the amplitudes of the sinusoidal distortion or the variance and correlation lengths of the random distortion functions. Mode losses in the fiber and losses in the fiber cavity with tilted mirrors are considered for the case of scattering losses and the case of losses introduced by the lossy cladding.

We find that cladding losses do not have a large influence on the wave loss in the fiber core, but scattering losses can be very serious if the amplitude of the wall roughness approaches the wavelength of the radiation.

Spherically curved mirrors could reduce the losses of fiber lasers with larger diameter if they reduce the field intensity at the fiber wall. However, this loss reduction would work only for perfectly straight fibers with perpendicular mirrors and very large radii. Our estimates of fiber losses associated with tilted plane mirrors are equally valid for fiber cavities with tilted curved mirrors if the tilt angle is large enough. For straight fibers with perpendicular but curved mirrors, our loss results can be regarded as an upper limit. It should also be clear that mirror tilt can be translated into an abrupt tilt of the fiber axis.

The analysis presented in this paper was performed to provide insight into the tolerance requirements of Nd-YAG fiber lasers.<sup>2</sup> Our numerical examples are thus geared to the parameters of this laser. The intrinsic losses of the fiber laser are on the order of  $10^{-3} \text{ cm}^{-1}$  so that additional losses caused by fiber irregularities or a lossy cladding should remain below this value.

Exact loss formulas may be expressed in terms of Bessel functions so that their numerical evaluation becomes tedious. For this reason, we are here deriving simplified formulas that allow reasonable order-of-magnitude estimates to be readily calculated with the help of a simple pocket calculator. Such handy approximations are often more useful than the formidable exact formulas and serve the purpose of providing insight into the relevant variables of the problem. All our loss formulas are immediately applicable to optical fibers that support many modes. Their application to the fiber laser is straightforward if we can be sure that there is no additional fiber irregularity with low spatial frequency coupling the guided modes among each other. However, even if mode coupling exists, it is known from theoretical<sup>3</sup>

and experimental<sup>2</sup> evidence that only modes of very low order participate in the lasing process. This information allows us to use the fiber loss results for the laser if we keep in mind that the loss prediction of the fiber mode of lowest order may somewhat underestimate the laser losses. For this reason, we base our discussion of laser losses on the mode with compound mode number  $M = 5$ . This loss estimate for the laser may, in fact, be pessimistic, but it provides the correct order of magnitude of the loss coefficient that may be used to derive tolerance requirements for the fiber laser.

## II. PLANE WAVE SCATTERING AT A PLANE INTERFACE

We base our loss analysis on the results of plane wave scattering at the rough planar interface between two dielectric media, as sketched in Fig. 2. Our analysis uses the theory of coupled modes. In this analysis, the incident plane wave is coupled to the continuum of modes of a medium that is divided into two half-spaces with a plane interface. The coupled mode theory is described in Ref. 4.

To first-order perturbation theory, the scattered power is computed as follows. First, we determine the amplitudes  $c_j(\sigma_x, \sigma_y)$  of the continuum modes that are excited by the incident plane wave interacting with the rough interface

$$c_j(\sigma_x, \sigma_y) = \int_{-(L_y/2)}^{L_y/2} dy \int_0^{L_x} K_{j\sigma} f(y, z) dz, \quad (1)$$

where the continuous variables  $\sigma_x$  and  $\sigma_y$  label the continuum modes,  $K_{j\sigma}$  is the coupling coefficient between incident wave and continuum modes, and  $\beta_i$  and  $\beta_s$  are the propagation constants ( $z$  components of the propagation vectors) of incident and scattered (continuum) waves.

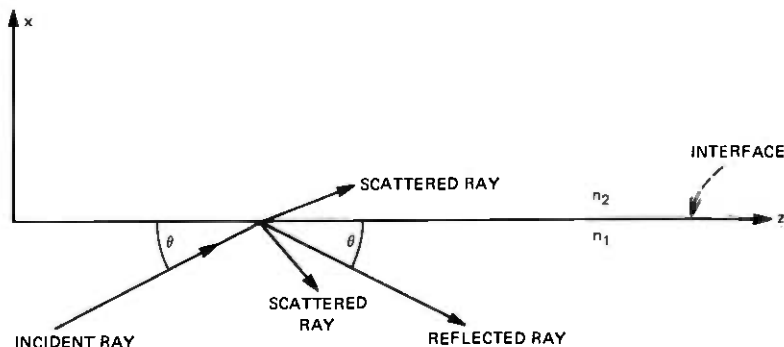


Fig. 2—Plane wave scattering at a plane, rough interface between two dielectric media with refractive indices  $n_1$  and  $n_2$ . The  $y$  axis is directed perpendicular to the plane of the figure.

It is assumed that the rough surface with distortion function  $f(y, z)$  extends only over an area  $L_y L_z$  in the  $y$  and  $z$  directions while the remainder of the infinite interface is perfectly flat. The coupling coefficient is defined as<sup>4</sup>

$$K_{j\sigma_i} = \frac{\omega \epsilon_0}{4iP} (n_1^2 - n_2^2) [\mathcal{E}_{\sigma_x, \sigma_y}^* \cdot \mathbf{E}_i]_{z=0}. \quad (2)$$

In this formula,  $\omega$  designates the angular frequency of the light waves,  $\epsilon_0$  is the dielectric permittivity,  $\mathbf{E}_i$  is the electric vector of the incident and specularly reflected and transmitted waves of the perfect interface, while  $\mathcal{E}_{\sigma_x, \sigma_y}$  indicates the electric field vector of the continuum mode. Label  $j$  designates the different types of continuum modes whose field expressions are given in the appendix and  $P$  in (2) is a power normalizing factor. The scattered power can now be calculated with the help of the formula<sup>4</sup>

$$P_{sc} = P \sum_j \iint_S |c_j(\sigma_x, \sigma_y)|^2 d\sigma_x d\sigma_y. \quad (3)$$

The summation extends over the different types of continuum modes, while the integration over the area  $S$  in the space  $\sigma_x, \sigma_y$  extends only over propagating continuum modes.

With the help of the mode fields listed in the appendix, we derive the following expressions for the scattered power. For a sinusoidal corrugation of the surface

$$f(y, z) = b \sin \Omega z, \quad (4)$$

we find

$$P_{sc} = \frac{b^2 S_x \kappa^2 k (n_1^2 - n_2^2) L_z L_y}{\beta_i (n_1 \sin \phi_1 + n_2 \sin \phi_2)}. \quad (5)$$

Here  $b$  is the amplitude of the sinusoidal deflection,  $S_x$  is the  $z$  component of the Poynting vector of the incident plane wave, and  $\kappa$  and  $\beta_i$  are, respectively, the  $x$  and  $z$  components of the propagation vector of the incident plane wave in the medium with index  $n_1$  whose magnitude is  $n_1 k$ . For sinusoidal corrugation, the scattered plane waves are emitted in definite directions whose angles are defined by<sup>4</sup>

$$\cos \phi_1 = \frac{\beta_i - \Omega}{n_1 k} \quad (6)$$

in medium 1 and by

$$\cos \phi_2 = \frac{\beta_i - \Omega}{n_2 k} \quad (7)$$

in medium 2.

Next we list the scattering formula for scattering from a random corrugation. There is no variation of the surface in the  $y$  direction,

but the variation in the  $z$  direction with variance  $\sigma^2$  is random with a correlation length  $D_z$  that is much shorter than the wavelength of light. The total amount of scattered power from an area  $L_y L_z$  is

$$P_{sc} = \frac{4}{n_1} L_y L_z S_z D_z \sigma^2 \kappa^2 k (n_1^2 - n_2^2) G_1 \left( \frac{n_1}{n_2} \right), \quad (8)$$

with

$$G_1 \left( \frac{n_1}{n_2} \right) = \frac{\sqrt{(n_1^2/n_2^2) - 1} - \frac{\pi}{2} + (n_1^2/n_2^2) \arcsin(n_2/n_1)}{\pi[(n_1^2/n_2^2) - 1]} \\ \approx 0.7162(n_2/n_1) - 0.6830(n_2/n_1)^2 + 0.4312(n_2/n_1)^3. \quad (9)$$

The polynomial was obtained as an empirical approximation of this function. Each component of the Fourier decomposition of the rough surface gives rise to two plane waves, one emitted into medium 1 and the other into medium 2. The directions of the two waves are related by Snell's law. If the angle (measured with respect to the surface) of the wave in medium 1, with the larger refractive index  $n_1$ , becomes so small that the angle of the wave in medium 2 becomes imaginary, no wave can escape into medium 2; but there is still a wave emitted into medium 1. Equation (8) contains the large-angle contributions from waves emitted into both media. However, at small scattering angles where the wave in medium 2 disappears, the scattered wave in medium 1 corresponds to a guided mode in a situation where medium 1 is the core of a fiber. Power scattered into guided mode directions is not lost, but becomes part of the "new" normal mode that establishes itself in the distorted fiber and is not included in (8).

Finally, we list the expression for the total scattered power when the interface is rough in  $y$  and  $z$  dimensions. The correlation length (much shorter than the wavelength) of the distortion in  $y$  direction is  $D_y$ ,

$$P_{sc} = \frac{4}{\pi} L_y L_z D_y D_z \sigma^2 S_z \kappa^2 k^2 (n_1^2 - n_2^2) G_2 \left( \frac{n_1}{n_2} \right). \quad (10)$$

In the previous two cases, radiation was escaping only in the  $x, z$  plane. In the case of a truly random surface distortion, radiation escapes isotropically in all directions. When we apply our present results to the case of fiber scattering, we want to distinguish between two types of radiation. Any ray direction not associated with a guided mode belongs to either a refracting or a tunneling leaky wave. Refracting leaky waves leave the fiber core because they impinge on the fiber boundary at an angle that cannot be contained inside the fiber by total internal reflection. Tunneling leaky waves consist of rays that should be trapped inside the fiber core by means of total internal

reflection.<sup>5,6</sup> However, tunneling leaky waves lose power by a mechanism that causes energy to tunnel through an evanescent wave region outside the fiber core to an external caustic from which they can escape. Refracting leaky rays are very lossy and can be considered radiative power. Tunneling leaky rays may have very low losses in fibers with large core diameters and may well be part of the "new" normal mode of the fiber cavity. It is thus desirable to be able to distinguish between power scattering into these two types of leaky rays. This distinction is made in the factor  $G_2(n_1/n_2)$  appearing in (10). We write

$$G_2 = G_{2r} + G_{2t}. \quad (11)$$

$G_{2r}$  incorporates only loss to refracting leaky rays, that is, rays scattered in those directions that, in a fiber, correspond to refracting leaky waves.  $G_{2t}$  incorporates the contribution from those scattering directions that, in a fiber, would correspond to tunneling leaky rays. Both expressions could be represented in closed form but, since the closed form formulas would be too unwieldy, we prefer to list them in the form of integrals:

$$G_{2r} \left( \frac{n_1}{n_2} \right) = \int_{\sqrt{1-(n_2^2/n_1^2)}}^1 \frac{v(1-v^2) + 2v^2\sqrt{v^2 - [1 - (n_2^2/n_1^2)]}}{(n_2^2/n_1^2)v + \sqrt{v^2 - [1 - (n_2^2/n_1^2)]}} dv$$

$$\approx 0.2666(n_2/n_1) - 0.05359(n_2/n_1)^2 + 0.3990(n_2/n_1)^3 \quad (12)$$

and

$$G_{2t} = \frac{1}{3} \sqrt{1 - (n_2^2/n_1^2)} - \frac{n_2}{3\pi n_1 [1 - (n_2^2/n_1^2)]}$$

$$\times \int_{(n_2/n_1)^2}^1 \frac{\sqrt{1-v}}{v\sqrt{v - (n_2^2/n_1^2)}} [2v + 1 - 3(n_2^2/n_1^2)] dv \quad (13a)$$

$$G_{2t} \approx 0.1364(n_2/n_1) + 0.7926(n_2/n_1)^2 - 0.2592(n_2/n_1)^3 \quad (13b)$$

The polynomials are again empirical approximations. The functions  $G_1$ ,  $G_{2r}$ , and  $G_2 = G_{2r} + G_{2t}$ , are plotted in Fig. 3. As a matter of curiosity, we note that, disregarding the differences between functions  $G_1$  and  $G_2$ , (8) and (10) become identical if we set the correlation length in the  $y$  direction equal to

$$D_y = \frac{\pi}{n_1 k} = \frac{\lambda_0}{2n_1}. \quad (14)$$

Of course, this is a purely formal relationship, since (10) does not apply for a correlation length on the order of the wavelength.

### III. LOSS DUE TO POWER DISSIPATION IN MEDIUM 2

In preparation for computing the fiber losses caused by a lossy jacket, we consider the plane wave reflection problem shown in Fig. 2 when

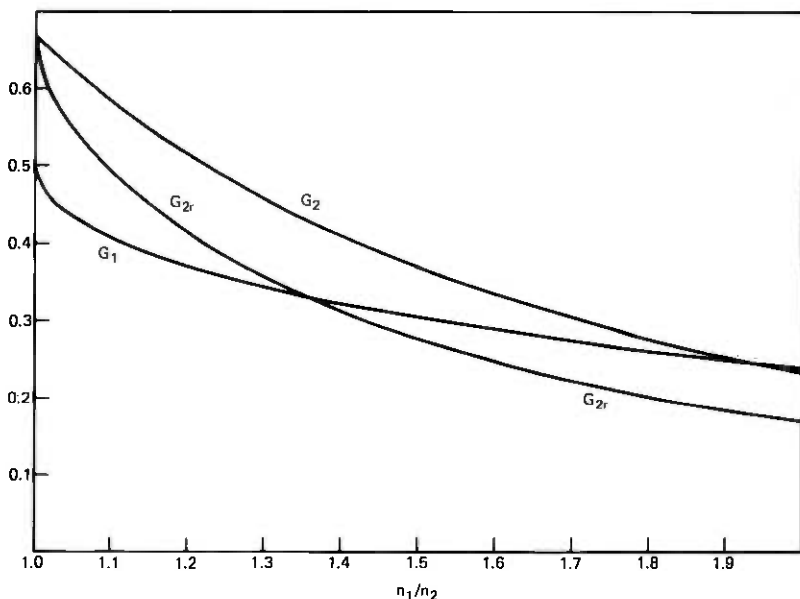


Fig. 3—The functions  $G_1$ ,  $G_2$ , and  $G_{2r}$  defined by (9) and (11) through (13) plotted versus  $n_1/n_2$ .

$n_1$  is lossless and the interface is perfectly plane, but medium 2 is lossy. The reflection coefficient for total internal reflection from the plane interface is expressed by the formula<sup>7</sup>

$$r = \frac{\kappa + i\gamma}{\kappa - i\gamma}, \quad (15)$$

with

$$\kappa = \sqrt{n_1^2 k^2 - \beta_i^2} \quad (16)$$

and

$$\gamma = \sqrt{\beta_i^2 - n_2^2 k^2}. \quad (17)$$

Using

$$n_2 = n_{2r} - in_{2i} \quad (18)$$

and the amplitude loss coefficient for plane wave propagation in medium 2,

$$\alpha_2 = n_{2i} k, \quad (19)$$

we obtain from (15), (17), and (18)

$$R = |r|^2 \approx 1 - \frac{4\alpha_2 n_{2r} \kappa}{(n_1^2 - n_{2r}^2) k^2}. \quad (20)$$

We have assumed that  $n_{2i} \ll n_{2r}$  and used  $\gamma^2 = (n_1^2 - n_{2r}^2) k^2$ , an approximation that holds for incident waves whose angle (with respect

to the interface) is far below the critical angle. When we apply our results to optical fibers, this assumption means that we limit ourselves to modes far from cutoff. The amount of dissipated power in an area  $L_y L_z$  is now

$$P_d = L_y L_z S_x (1 - R). \quad (21)$$

$S_x$  is the  $x$  component of the Poynting vector. We use the relation  $S_x = (\kappa/\beta_i) S_z$  and obtain, from (20) and (21),

$$P_d = \frac{2(2\alpha_2)n_2 L_y L_z S_x k^2}{n_1(n_1^2 - n_2^2)^{1/2} k^3}. \quad (22)$$

The real part of the refractive index has again been replaced by the symbol  $n_2$ , and we used the approximation  $\beta_i = n_1 k$ .

#### IV. APPLICATION TO MULTIMODE FIBERS

The guided-mode field in optical fibers can be approximated as<sup>4</sup>

$$E_y = A J_\nu(\kappa r) \cos \nu \phi e^{-i\beta z}. \quad (23)$$

The power density flowing in the  $z$  direction is thus given by

$$S_z = \frac{1}{2} \frac{P}{\pi a^2} \cos^2 \nu \phi, \quad (24)$$

where  $P$  is the total power carried by the guided mode. Since the fiber radius is  $a$ , we obtain the power density  $P/(\pi a^2)$ . The factor  $\frac{1}{2}$  appearing in (24) accounts for the fact that half the total power is carried by a wave traveling toward the core boundary while the other half travels away from the boundary after reflection. The factor  $\cos^2 \nu \phi$  follows in an obvious manner from (23). Averaging over the entire circumference of the fiber, we obtain

$$\bar{S}_z = \frac{1}{4} \frac{P}{\pi a^2}. \quad (25)$$

The mode losses are now obtained from the plane wave formulas of the last two sections by identifying  $L_y = 2\pi a$ , replacing  $S_x$  with  $\bar{S}_z$  of (25) and using the formula (for heat losses,  $P_{sc}$  is replaced by  $P_d$ )

$$2\alpha = \frac{P_{sc}}{L_z P}. \quad (26)$$

We can thus immediately compile the following list of power-loss coefficients for the various fiber loss mechanisms.

*Sinusoidal radius variation of amplitude  $b$ :*

$$2\alpha = \frac{b^2 k^2 (n_1^2 - n_2^2)}{2an_1(n_1 \sin \phi_1 + n_2 \sin \phi_2)}. \quad (27)$$

The angles  $\phi_1$  and  $\phi_2$  are defined by (6) and (7).

Random radius variation with correlation length  $D_r$  and variance  $\sigma^2$ :

$$2\alpha = \frac{2}{n_1 a} D_r \sigma^2 \kappa^2 k (n_1^2 - n_2^2) G_1 \left( \frac{n_1}{n_2} \right). \quad (28)$$

Random surface variation with correlation length  $D_\phi$  (formerly called  $D_y$ ) in the  $\phi$  direction and  $D_z$  in the  $z$  direction and variance  $\sigma^2$ :

$$2\alpha = \frac{2}{\pi a} D_\phi D_z \sigma^2 \kappa^2 k^2 (n_1^2 - n_2^2) G_2 \left( \frac{n_1}{n_2} \right). \quad (29)$$

Functions  $G_1$ ,  $G_2$ , and  $G_{2r}$  are plotted in Fig. 3. Whether  $G_2$  or  $G_{2r}$  is to be used depends on the length and size of the fiber. If tunneling leaky modes are only slightly attenuated in the length of fiber under consideration and can be regarded as guided modes, we must use  $G_{2r}$ ; if tunneling leaky waves are very lossy,  $G_2$  must be used; in intermediate cases, an average value may be appropriate. For a discussion of the losses of tunneling leaky waves, see Refs. 5 and 6. Finally, we list the power loss coefficient for a multimode fiber with lossy cladding (but lossless core) with cladding power-loss coefficients  $2\alpha_2$ :

$$2\alpha = \frac{(2\alpha_2)n_2\kappa^2}{n_1 a (n_1^2 - n_2^2)^{3/2} k^3}. \quad (30)$$

It remains to specify the values of  $\kappa$  that must be inserted into formulas (27) through (30). In fibers supporting only one or very few guided modes,  $\kappa$  would have to be obtained as the solution of the eigenvalue equation. However, our formulas hold only for large fibers supporting many modes that are mostly far from cutoff. In this case, it is possible to approximate  $\kappa$  as<sup>4</sup>

$$\kappa = \frac{\pi}{2a} (M - \frac{1}{2}). \quad (31)$$

The compound mode number  $M$  is a combination of the azimuthal mode number  $\nu$  and the radial mode number  $\mu$ ,

$$M = \nu + 2\mu = 2, 3, 4, \dots \quad (32)$$

If we are interested in the losses of a fiber cavity with tilted mirrors, Fig. 1b suggests that we use the expression

$$\kappa = n_1 k \sin \theta. \quad (33)$$

In this case, the field impinges on the fiber wall not at the natural mode angle applicable for perfectly straight fibers but at a larger angle  $\theta$  that is imposed by the gross deformation of the fiber or mirror

<sup>4</sup> Eq. (31) holds for small values of  $\nu$ . For large  $\nu$ , we must replace  $(\kappa a)^2 \rightarrow U^2 - \nu^2$  [see Ref. 4, p. 90, eq. (2.5-6)] and obtain  $U$  as the solution of  $J_\nu(U) = 0$ .

geometry. For fiber lasers, it seems reasonable to associate  $\theta$  with the mirror tilt angle. For fibers with abrupt tilts,  $\theta$  would be the fiber tilt angle.

Our derivation of formulas for the fiber loss coefficients was based on the properties of plane wave interaction with a plane interface. It is thus clear that our equations are only approximately valid. In particular, they do not incorporate interference effects between directly scattered rays and rays that leave the fiber after repeated reflections inside the fiber core. Such effects are particularly pronounced for scattering from purely sinusoidal core radius variations because, in this case, the radiation leaves at a definite angle and may be enhanced or reduced by interference effects.<sup>8</sup> Our equations give an average over the maxima and minima of the loss fluctuations as a function of scattering angle. The formulas for scattering from random surface effects or heat losses in the cladding are more reliable because diffuse scattering causes radiation to escape in all directions and interference effects tend to cancel out and are unimportant in the case of power dissipation in the cladding. The formulas derived here are handy order-of-magnitude approximations of the precise expressions containing Bessel functions.<sup>4,8</sup>

## V. DISCUSSION AND NUMERICAL RESULTS

In this section, we present loss coefficients in graphic form. We begin with a fiber with sinusoidal core radius variations of amplitude  $b$  and spatial frequency  $\Omega$ . Scattering losses occur only if the radiation can escape into the cladding. The spatial frequency range that results in scattering losses is thus obtained from (7) as

$$(n_1 - n_2)k < \Omega < (n_1 + n_2)k, \quad (34)$$

where we have assumed that  $\beta_i \approx n_1 k$ . If we introduce the length of the spatial period as  $\Lambda = 2\pi/\Omega$ , we obtain from (34) and  $k = 2\pi/\lambda_0$

$$\frac{\lambda_0}{n_1 - n_2} > \Lambda > \frac{\lambda_0}{n_1 + n_2}. \quad (35)$$

These formulas apply, of course, also to the spatial frequency range that contributes to random scattering, discussed below.

Figure 4 shows curves plotted from (27). On the horizontal axis, we have plotted the normalized spatial frequency  $\Omega/n_1 k$  and also the scattering angle  $\Phi_2$  at which the radiation escapes into medium 2. Beyond  $\Omega/n_1 k = 1$ , the curves form the mirror image of the section shown in the figure and were consequently omitted. Figure 4 was computed for YAG with  $n_1 = 1.8$  and  $n_2 = 1$ . The parameter of the curves in Fig. 4 is the compound mode number  $M$  defined by (32).

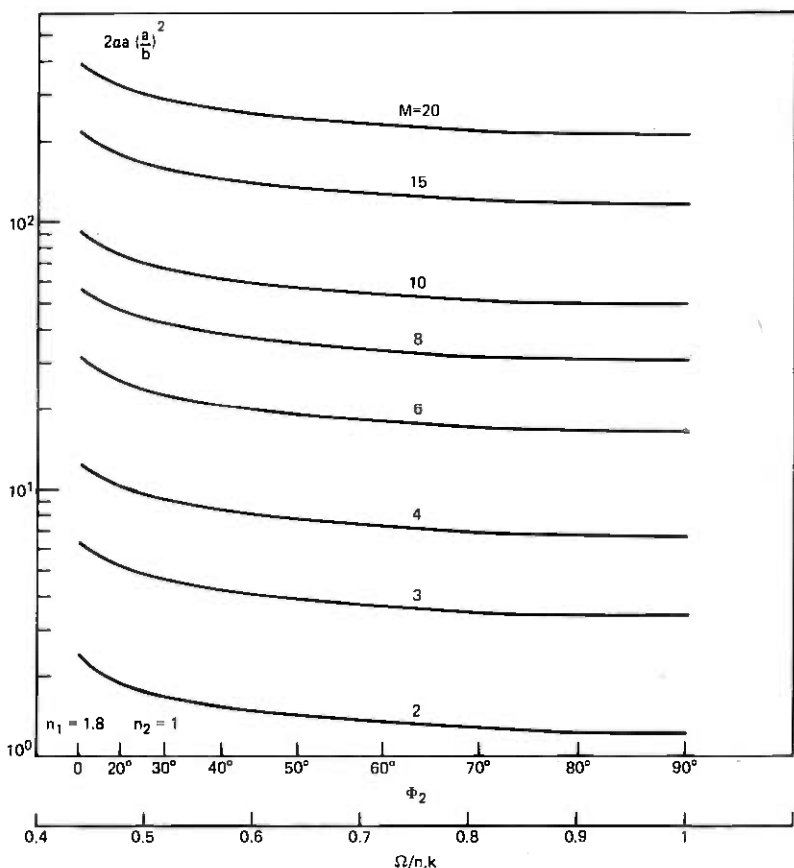


Fig. 4—Normalized scattering loss coefficient for a cavity with perpendicular mirrors (relative to the fiber axis) and sinusoidal core radius variation of amplitude  $b$  and spatial frequency  $\Omega$ .  $M$  is the compound mode number. For this set of curves,  $n_1 = 1.8$ ,  $n_2 = 1.0$ .

To obtain a feeling for the magnitude of the normalized loss coefficient and for the tolerance requirements, we assume that the fiber resonator has an inherent loss of  $2\alpha = 10^{-3} \text{ cm}^{-1}$  and a core radius of  $a = 40 \text{ }\mu\text{m}$ . Scattering loss begins to be of concern if its magnitude equals the already existing cavity losses. Allowing for the possibility that a few fiber modes of low order are tightly coupled by some fiber deformation of large amplitude but with a spatial frequency below range (34), we use an average value of  $2\alpha a^2/b^2 = 10$ . If we are willing to tolerate a loss of  $2\alpha = 10^{-3} \text{ cm}^{-1}$  for  $a = 40 \text{ }\mu\text{m}$ , we find as the maximum permissible ripple amplitude the value  $b = 2.5 \times 10^{-2} \text{ }\mu\text{m}$ .

Figure 5 shows curves that are similar to Fig. 4 except that we have

assumed that the YAG fiber now carries a cladding with refractive index  $n_2 = 1.5$ . It is apparent that the cladding causes a reduction of the scattering loss by roughly a factor of 2 so that we can now tolerate a ripple amplitude that is larger by  $\sqrt{2}$ .

Figure 6 still describes a cavity with a fiber with sinusoidal core radius variation, but in this case we have assumed that the mirrors are tilted by an angle  $\theta$ . The tilt of the mirrors causes the field inside the cavity to impinge on the fiber wall at an angle that is roughly equal to the tilt angle. It is interesting to consider the intrinsic mode angle to obtain a feeling for the severity of tilt angles introduced externally.

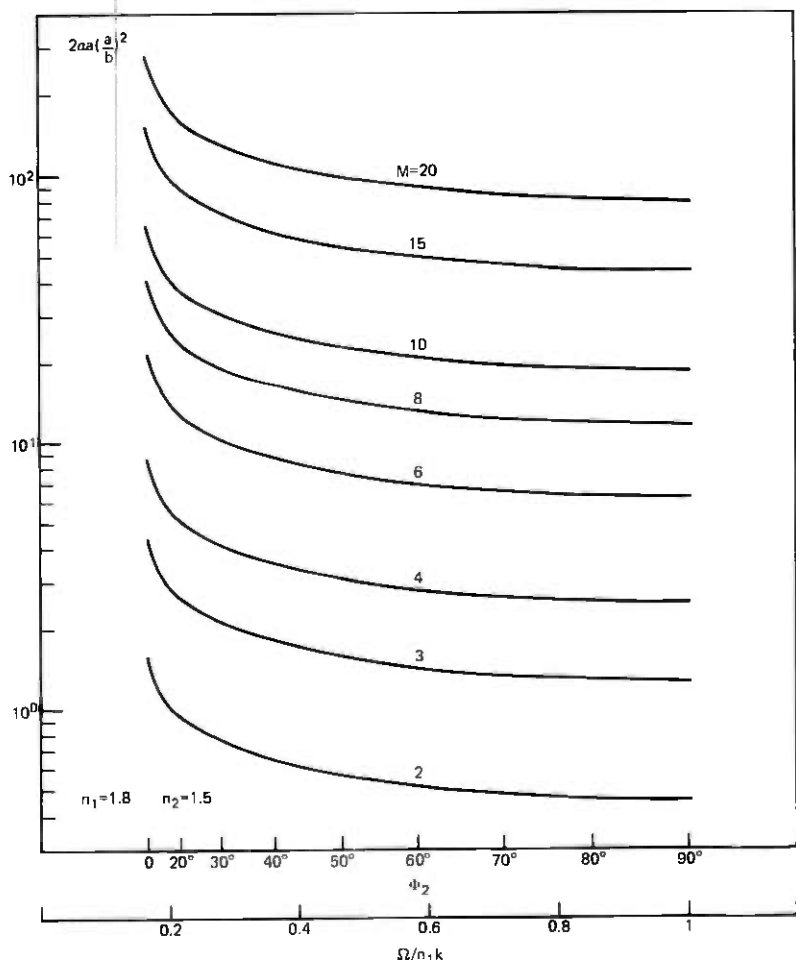


Fig. 5—Same as Fig. 4 but with  $n_2 = 1.5$ .

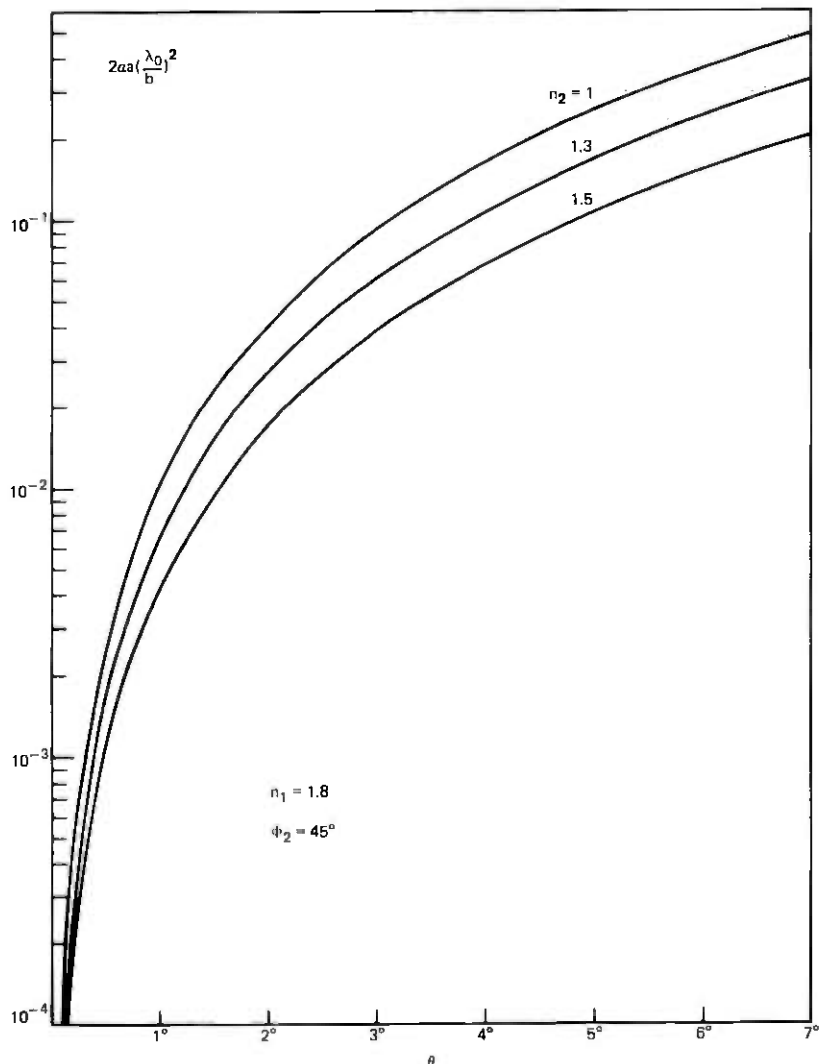


Fig. 6—Normalized scattering loss coefficient for a cavity with tilted mirrors, tilt angle  $\theta$ , and sinusoidal core radius variation of amplitude  $b$  and spatial frequency  $\Omega$  ( $n_1 = 1.8$  and  $\phi_2 = 45^\circ$ ).

By equating (31) and (33), we find for the mode angle

$$\theta_M = \arcsin \left( \frac{\pi(M - \frac{1}{2})}{2n_1ka} \right). \quad (36)$$

For  $a = 40 \mu\text{m}$ ,  $\lambda_0 = 1.06 \mu\text{m}$ , and  $n_1 = 1.8$ , we find  $\theta_M = 0.32$  degree for the fiber mode of lowest order, with  $M = 2$  and  $\theta_M = 2$

degrees for  $M = 10$ . We have assumed that mirror tilt can be controlled fairly accurately and extended our curves only to  $\theta = 7$  degrees. It is now more natural to normalize the loss coefficient as  $2\alpha a(\lambda_0/b)^2$ . At a tilt angle of  $\theta = 5$  degrees, we may expect for  $n_1/n_2 = 1.8$  the normalized loss  $2\alpha a(\lambda_0/b)^2 = 0.25$  according to Fig. 6. With  $2\alpha = 10^{-3} \text{ cm}^{-1}$ ,  $a = 40 \text{ } \mu\text{m}$  and  $\lambda_0 = 1.06 \text{ } \mu\text{m}$ , we find the ripple amplitude  $b = 4.2 \times 10^{-3} \text{ } \mu\text{m}$ , which is a more stringent tolerance requirement than the value found for straight mirrors.

Next we consider a cavity with a fiber with randomly varying core radius. The case of a cavity with perpendicular mirrors is plotted from (28) and (9) in Fig. 7. It is assumed that the rms amplitude of the random core radius variation is  $\bar{\sigma}$  and that the correlation length  $D_z$  is much shorter than the wavelength of light. If the cavity loss is an average value of fiber mode losses corresponding to  $M = 5$  in Fig. 7, we have  $2\alpha a^3 \lambda_0 / D_z \bar{\sigma}^2 = 200$ . With  $a = 40 \text{ } \mu\text{m}$  and  $2\alpha = 10^{-3} \text{ cm}^{-1}$ , we obtain  $D_z \bar{\sigma}^2 = 3.4 \times 10^{-5} \text{ } \mu\text{m}^3$ . For want of more information, we assume that  $\bar{\sigma} = D_z$ , so that we have  $D_z = \bar{\sigma} = 3.2 \times 10^{-2} \text{ } \mu\text{m}$ . This

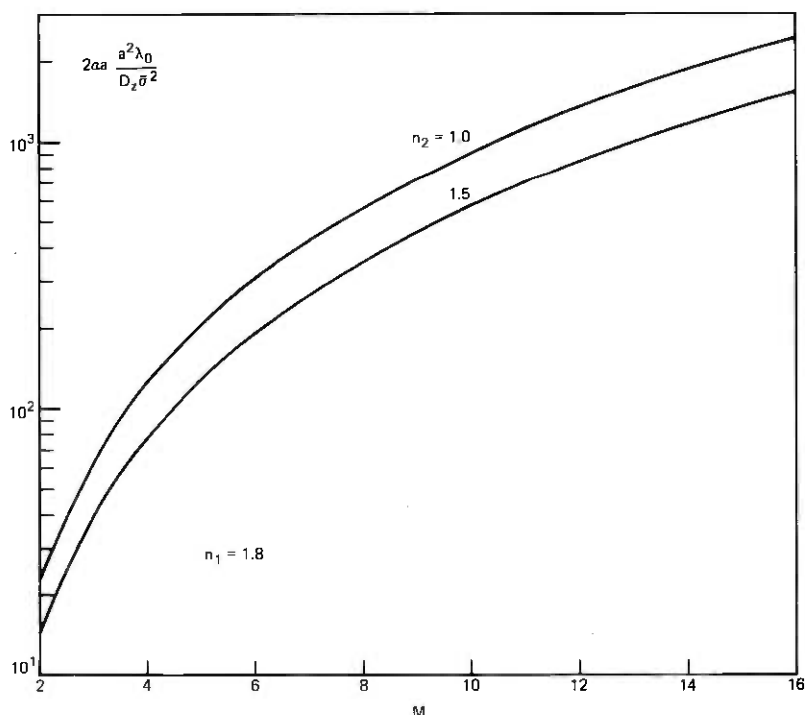


Fig. 7—Normalized scattering loss coefficient for a cavity with perpendicular mirrors and random core radius variations with variance  $\bar{\sigma}^2$  and correlation length  $D_z$ .  $M$  is the compound mode number,  $n_1 = 1.8$ .

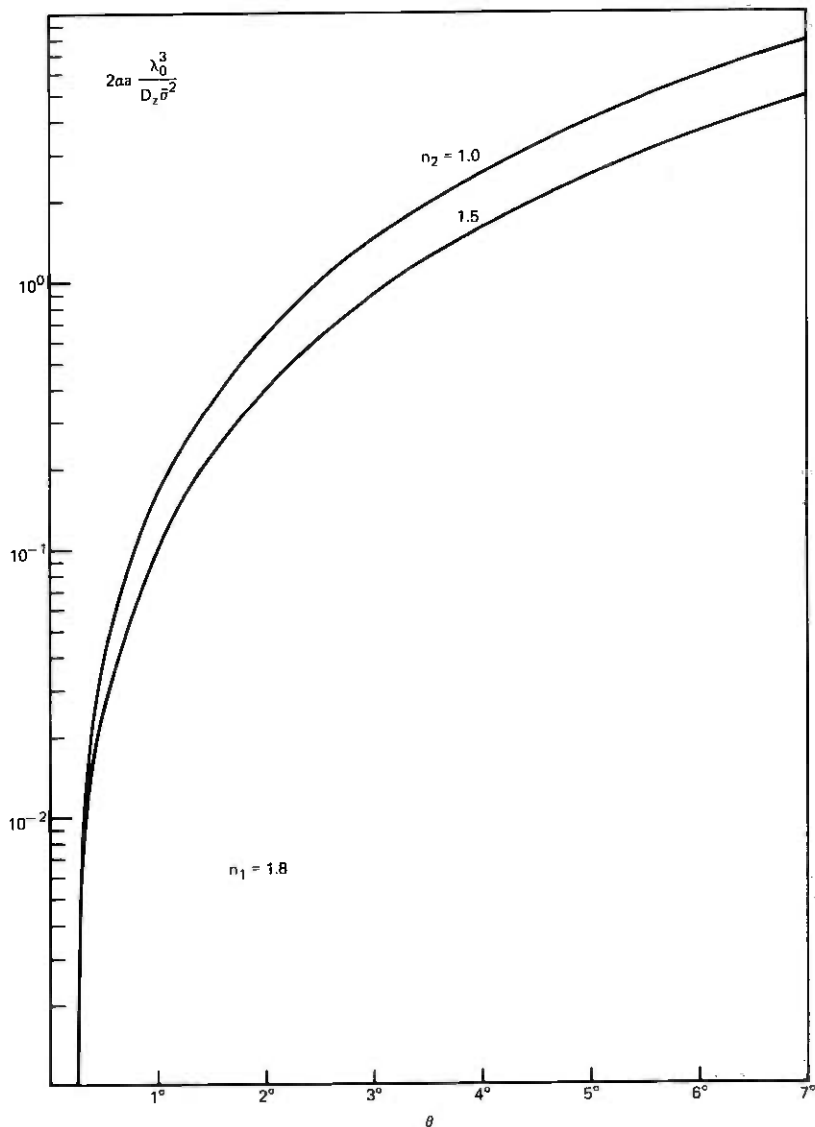


Fig. 8—Normalized scattering loss coefficient for a cavity with tilted mirrors, tilt angle  $\theta$ , and random core radius variation for  $n_1 = 1.8$ .

value is quite comparable to the value  $b = 2.5 \mu\text{m}$  that we found in the case of a sinusoidal core radius variation.

Figure 8 gives the normalized scattering loss for a cavity with random core radius variation for the case of tilted mirrors. For  $n_2 = 1$  and  $\theta = 5$  degrees, we find from Fig. 8  $2\alpha a \lambda_0^3 / D\sigma^2 = 4$ . With  $a = 40$

$\mu\text{m}$ , we obtain a loss of  $2\alpha = 10^{-3} \text{ cm}^{-1}$  for  $D_z\bar{\sigma}^2 = 1.2 \times 10^{-6} \mu\text{m}^3$  or  $D_z = \bar{\sigma} = 1.1 \times 10^{-2} \mu\text{m}$ .

Figures 9 and 10 pertain to fibers with random core-cladding interface perturbations. Figure 9 describes a fiber cavity with perpendicular mirrors. At  $M = 5$  we find, from Fig. 9,  $2\alpha a^3 \lambda_0^2 / D_\phi D_z \bar{\sigma}^2 = 600$ . With the usual values for loss, core radius, and light wavelength, we have  $D_\phi D_z \bar{\sigma}^2 = 1.2 \times 10^{-6} \mu\text{m}^4$  or  $D_\phi = D_z = \bar{\sigma} = 5.9 \times 10^{-2} \mu\text{m}$ . If we let the two correlation lengths equal the rms variation of the interface, we find that the tolerance requirements are a little less stringent for a totally random surface compared to a surface that maintains its circular cross section and only allows the radius to vary along  $z$ .

Figure 10 shows the normalized loss coefficient for random core-cladding interface perturbations (in two dimensions) for a cavity with tilted mirrors. For a mirror tilt of  $\theta = 5$  degrees, we obtain from Fig. 10 approximately  $2\alpha a \lambda_0^4 / D_\phi D_z \bar{\sigma}^2 = 12$ . With  $a = 40 \mu\text{m}$ , a loss of  $2\alpha = 10^{-3} \text{ cm}^{-1}$  is obtained for  $D_\phi D_z \bar{\sigma}^2 = 4.2 \times 10^{-7} \mu\text{m}^4$  or  $D_\phi = D_z = \bar{\sigma} = 2.5 \times 10^{-2} \mu\text{m}$ .

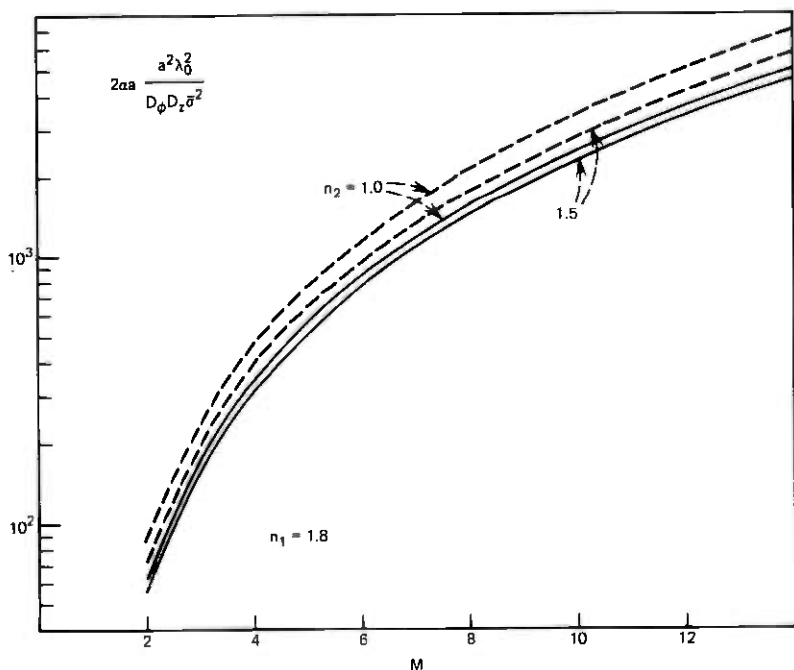


Fig. 9—Normalized scattering loss coefficient for a cavity with perpendicular mirrors and random core-cladding interface perturbations with correlation length  $D_\phi$  in azimuthal direction,  $D_z$  in  $z$  direction, and variance  $\bar{\sigma}^2$ . The solid lines apply to a fiber whose tunneling leaky waves may be regarded as lossless guided waves; the dotted lines belong to the case in which tunneling leaky waves are so lossy that they cannot be regarded as guided waves.  $M$  is the compound mode number,  $n_1 = 1.8$ .

The remaining figures, 11 and 12, describe the normalized loss coefficient for a geometrically perfect fiber core surrounded by a lossy cladding. The power loss coefficient of a plane wave traveling in the material of the cladding is  $2\alpha_2$ . Figure 11 gives the mode losses of the fiber as a function of the normalized frequency parameter

$$V = \frac{2\pi a}{\lambda_0} (n_1^2 - n_2^2)^{1/2}. \quad (37)$$

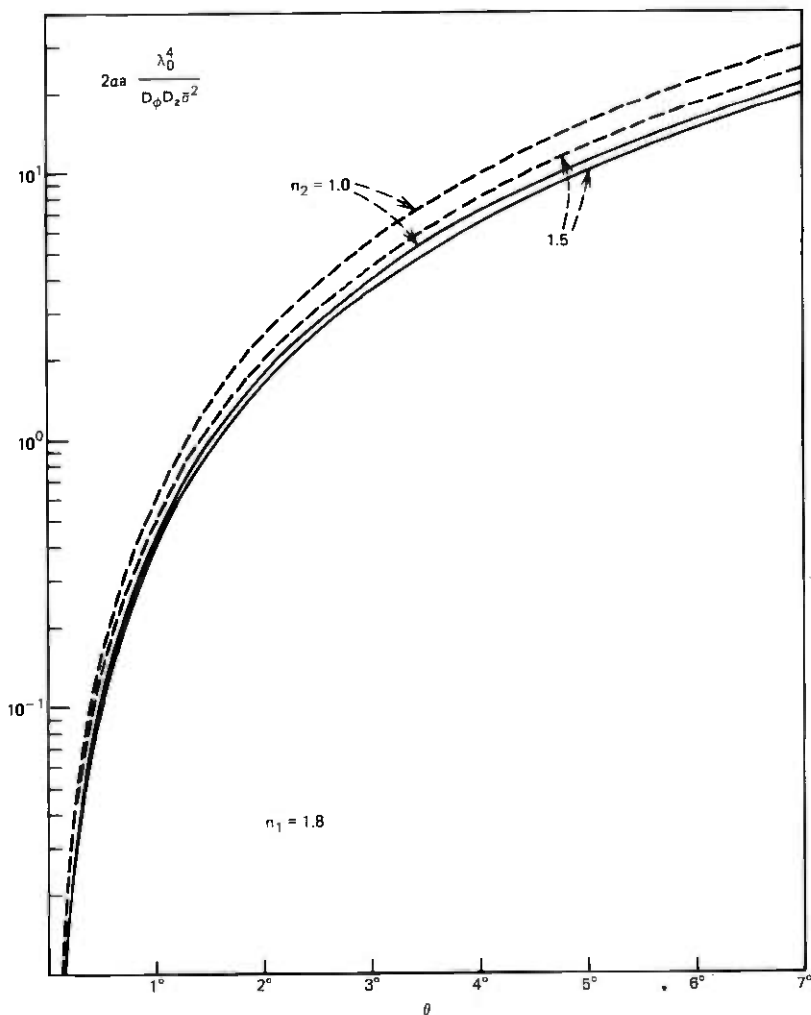


Fig. 10—Similar to Fig. 9 except that the cavity in this case has tilted mirrors with tilt angle  $\theta$ .

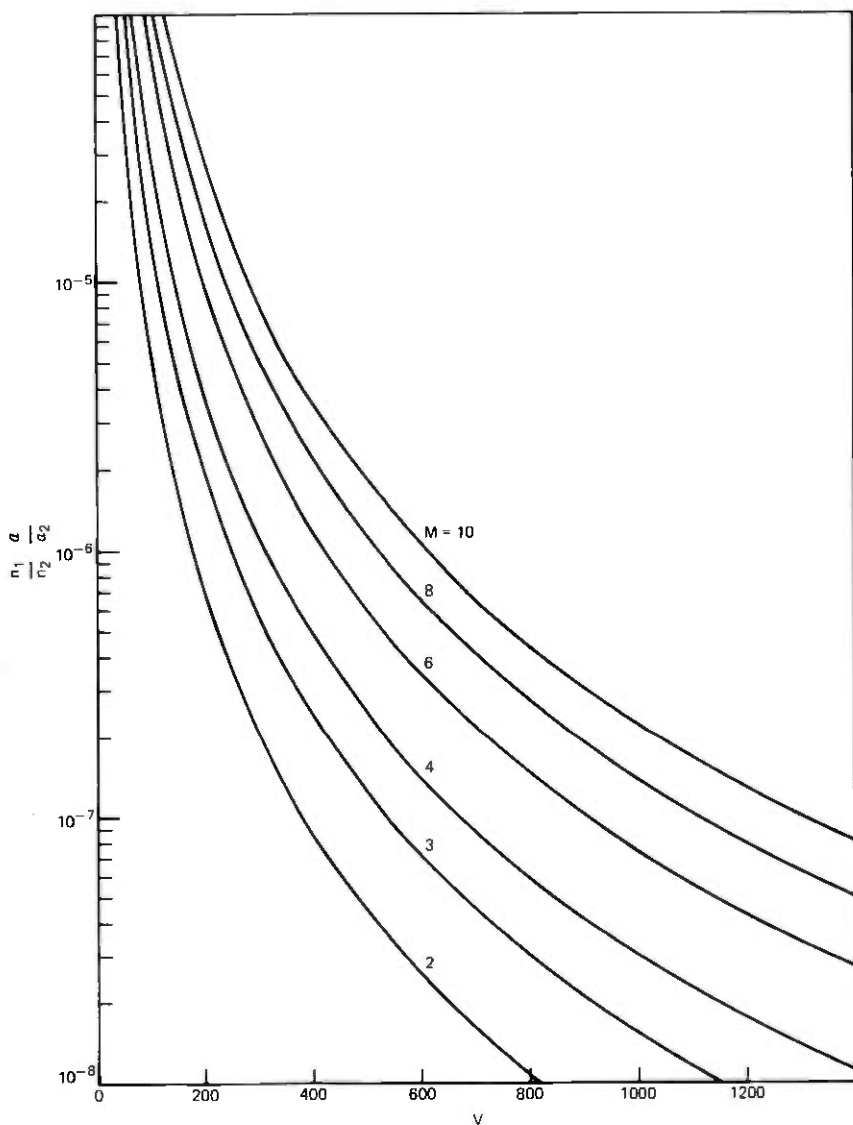


Fig. 11—Absorption loss coefficient of a fiber with lossy cladding (cladding loss coefficient  $\alpha_2$ ). This set of curves applies to the case of a cavity with perpendicular mirrors. The normalized frequency  $V$  is defined by (37).

For  $\lambda_0 = 1.06 \mu\text{m}$ ,  $a = 40 \mu\text{m}$ ,  $n_1 = 1.8$ , and  $n_2 = 1$ , we obtain  $V = 355$  from (37). For  $M = 5$ , we obtain from Fig. 11 approximately  $n_1 \alpha_1 / n_2 \alpha_2 = 10^{-6}$ . The mode losses are thus much less than

the cladding losses. For  $2\alpha = 10^{-3} \text{ cm}^{-1}$  and  $n_1/n_2 = 1.8$ , we could tolerate a cladding loss of  $2\alpha_2 = 1.8 \times 10^3 \text{ cm}^{-1}$ . If we use  $n_2 = 1.5$ , we have  $V = 236$  leading to  $n_1\alpha/n_2\alpha_2 = 4 \times 10^{-6}$  at  $M = 5$ . With  $n_1/n_2 = 1.2$ , we can now tolerate  $2\alpha_2 = 300 \text{ cm}^{-1}$ .

Figure 12 applies to a cavity with tilted mirrors and lossy jacket.

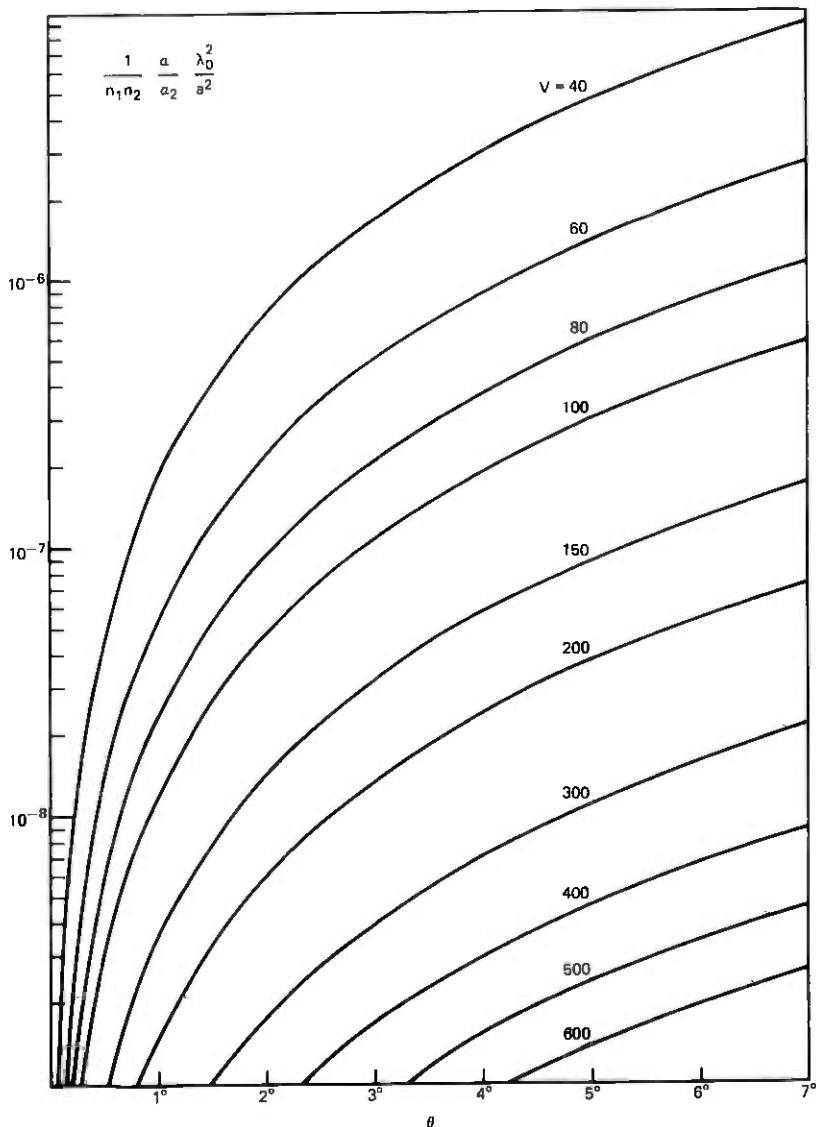


Fig. 12—Absorption loss coefficient of a fiber with lossy cladding (loss coefficient  $\alpha_2$ ). These curves apply to the case of a cavity with tilted mirrors, tilt angle  $\theta$ .

Table I—Results of numerical evaluations of cladding losses.  
The cladding loss,  $2\alpha_2$ , gives rise to a mode loss  
of  $2\alpha = 10^{-3} \text{ cm}^{-1}$

V	$n_1/n_2$	$2\alpha_2$	
		$M = 5, \theta = 0$	$\theta = 5^\circ$
355	1.8	$1.8 \times 10^3 \text{ cm}^{-1}$	$56 \text{ cm}^{-1}$
236	1.2	300	10.4

For  $\theta = 5$  degrees and  $V = 355$ , we find  $\alpha\lambda_0^2(n_1n_2\alpha_2a^2) = 7 \times 10^{-9}$ . With  $n_1 = 1.8$ ,  $n_2 = 1$ ,  $a = 40 \mu\text{m}$ , and  $2\alpha = 10^{-3} \text{ cm}^{-1}$ , we can tolerate  $2\alpha_2 = 56 \text{ cm}^{-1}$ . If  $V = 236$  and  $n_2 = 1.5$ , we can tolerate  $2\alpha_2 = 10.4 \text{ cm}^{-1}$ . These results are summarized in Table I.

## VI. CONCLUSIONS

We have studied the losses of fibers and fiber resonators that are caused by perturbations of the core-cladding interface and by absorption losses of the cladding material. Formulas for the loss coefficient were derived by using plane wave techniques, and representative examples were displayed in the form of normalized curves. The theory presented here is not precise, and its application to practical cases is hampered by lack of knowledge of coupling among the guided modes. We have seen in a previous paper<sup>3</sup> that mode coupling tends to increase the cavity losses above the minimum value of the fiber mode of lowest order. However, the loss increase due to mode coupling results only in an average loss of a few of the lower-order modes that are coupled particularly tightly. We have thus concentrated on an average loss corresponding to mode  $M = 5$  when we considered explicit loss values. Our results are useful to gain insight into the order of magnitude of fiber tolerances that must be maintained and into the amount of cladding losses that can be tolerated. We found that the tolerances of core-cladding interface perturbations are on the order of  $0.01 \mu\text{m}$ , while cladding losses can be allowed to be as high as  $10 \text{ cm}^{-1}$  in the worst case of a cavity with mirrors tilted by 5 degrees, or as high as  $300 \text{ cm}^{-1}$  in the case of a cavity with perfectly perpendicular mirrors. Mirror losses were lumped in with the "background losses" of the cavity, which were assumed to be  $2\alpha = 10^{-3} \text{ cm}^{-1}$  in all the numerical examples we have considered. All curves independent of mirror tilt can be used to obtain the losses of optical fibers because they show plots of fiber mode losses without being tied to an application to fiber resonators.

## VII. ACKNOWLEDGMENT

Many helpful discussions with J. Stone are gratefully acknowledged.

## APPENDIX

For the calculation of scattering losses of a plane wave impinging on an irregular dielectric interface, we need to know the radiation modes of a space consisting of two dielectric media with refractive indices  $n_1$  and  $n_2$  separated by a plane interface. There are several types of such radiation modes. In each case, we list only the  $E_x$  and  $H_x$  components of their electric and magnetic fields, since all other field components follow from these longitudinal components by differentiation.<sup>9</sup> The time dependence of the modes is understood to be of the form

$$e^{i\omega t}. \quad (38)$$

We place our coordinate system so that the interface between the media with  $n_1$  and  $n_2$  lies in the  $y$ - $z$  plane. We assume that  $n_1 > n_2$  and let the medium with index  $n_2$  be in the half space  $x > 0$ .

There are radiation modes whose fields decay exponentially in positive  $x$  direction for  $x > 0$ . These modes can be grouped further into modes with  $E_x = 0$  and  $H_x = 0$ .

(i) Evanescent modes with  $E_x = 0$ :

$$\left. \begin{aligned} \mathcal{E}_x &= A_1 e^{-\Delta x} e^{-i(\sigma_y y + \beta z)} \\ \mathcal{H}_x &= i \frac{\beta \Delta}{\omega \mu_0 \sigma_y} A_1 e^{-\Delta x} e^{-i(\sigma_y y + \beta z)} \end{aligned} \right\} \text{for } x \geq 0 \quad (39)$$

$$\left. \begin{aligned} \mathcal{E}_x &= A_1 \left( \cos \sigma_x x - i \frac{\Delta}{\sigma_x} \sin \sigma_x x \right) e^{-i(\sigma_y y + \beta z)} \\ \mathcal{H}_x &= i \frac{\beta \sigma_x}{\omega \mu_0 \sigma_y} A_1 \left[ \sin \sigma_x x - \frac{\Delta}{\sigma_x} \cos \sigma_x x \right] e^{-i(\sigma_y y + \beta z)} \end{aligned} \right\} \text{for } x \leq 0. \quad (40)$$

The parameters entering these equations are related by

$$n_1^2 k^2 = \sigma_x^2 + \sigma_y^2 + \beta^2 \quad (41)$$

and

$$n_2^2 k^2 = -\Delta^2 + \sigma_y^2 + \beta^2. \quad (42)$$

The fields are normalized with respect to a delta function,

$$\frac{1}{2} \iint (\mathcal{E}_x \mathcal{H}_y^* - \mathcal{E}_y \mathcal{H}_x^*) dx dy = P \delta(\sigma_x - \sigma'_x) \delta(\sigma_y - \sigma'_y), \quad (43)$$

so that we obtain for the amplitude coefficient

$$A_1^2 = \frac{2a^2 \omega \mu_0 \sigma_x^2 \sigma_y^2 P}{\pi^2 V^2 \beta (\beta^2 + \sigma_y^2)}, \quad (44)$$

with  $V$  defined by (37) and  $\mu_0$  indicating the magnetic permeability of vacuum.

(ii) Evanescent modes with  $H_x = 0$ :

$$\left. \begin{aligned} \mathcal{E}_z &= A_2 e^{-\Delta x} e^{-i(\sigma_y y + \beta z)} \\ \mathcal{H}_z &= i \frac{n_2^2 k^2 \sigma_y}{\omega \mu_0 \beta \Delta} A_2 e^{-\Delta x} e^{-i(\sigma_y y + \beta z)} \end{aligned} \right\} \text{for } x \geq 0 \quad (45)$$

$$\left. \begin{aligned} \mathcal{E}_z &= A_2 \left( \cos \sigma_x x + \frac{n_2^2 \sigma_x}{n_1^2 \Delta} \sin \sigma_x x \right) e^{-i(\sigma_y y + \beta z)} \\ \mathcal{H}_z &= i \frac{n_2^2 k^2 \sigma_y}{\omega \mu_0 \beta \Delta} A_2 \left( \cos \sigma_x x - \frac{n_1^2 \Delta}{n_2^2 \sigma_x} \sin \sigma_x x \right) e^{-i(\sigma_y y + \beta z)} \end{aligned} \right\} \text{for } x \leq 0. \quad (46)$$

Equations (41) and (42) still apply, and the amplitude coefficient is

$$A_2^2 = \frac{2\omega\mu_0 n_1^2 \sigma_x^2 \Delta^2 \beta P}{\pi^2 k^2 (n_2^2 \sigma_x^2 + n_1^4 \Delta^2) (\beta^2 + \sigma_y^2)}. \quad (47)$$

These first two types of modes are valid only in a limited range of  $\sigma_x$  and  $\sigma_y$  that is determined by the requirement that  $\Delta$ , defined by (42), must be a positive real quantity.

(iii) Full standing wave modes with  $E_x = 0$ :

$$\left. \begin{aligned} \mathcal{E}_z &= A_{3j} (\cos \rho_x x + R_j \sin \rho_x x) e^{-i(\sigma_y y + \beta z)} \\ \mathcal{H}_z &= i \frac{\beta \rho_x}{\omega \mu_0 \sigma_y} A_{3j} (\sin \rho_x x - R_j \cos \rho_x x) e^{-i(\sigma_y y + \beta z)} \end{aligned} \right\} \text{for } x \geq 0 \quad (48)$$

$$\left. \begin{aligned} \mathcal{E}_z &= A_{3j} \left( \cos \sigma_x x + \frac{\rho_x}{\sigma_x} R_j \sin \sigma_x x \right) e^{-i(\sigma_y y + \beta z)} \\ \mathcal{H}_z &= i \frac{\beta \sigma_x}{\omega \mu_0 \sigma_y} A_{3j} \left( \sin \sigma_x x - \frac{\rho_x}{\sigma_x} R_j \cos \sigma_x x \right) e^{-i(\sigma_y y + \beta z)} \end{aligned} \right\} \text{for } x \leq 0. \quad (49)$$

Equation (41) applies in this case, too, but (42) is replaced by

$$n_2^2 k^2 = \rho_x^2 + \sigma_y^2 + \beta^2. \quad (50)$$

The coefficient  $R_j$  is arbitrary, but it is convenient to choose two values  $R_1$  and  $R_2$  so that the two resulting modes become mutually orthogonal. We choose for convenience

$$R_1 = 0 \quad (51)$$

and

$$R_2 = \infty. \quad (52)$$

The corresponding amplitude coefficients are

$$A_{31}^2 = \frac{2\sigma_x \sigma_y^2 \omega \mu_0 P}{\pi^2 \beta (\sigma_x + \rho_x) (\beta^2 + \sigma_y^2)} \quad (53)$$

and

$$R_2^2 A_{32}^2 = \frac{2\sigma_x^2 \sigma_y^2 \omega \mu_0 P}{\pi^2 \beta \rho_x (\sigma_x + \rho_x) (\beta^2 + \sigma_y^2)}. \quad (54)$$

(iv) Full standing wave modes with  $H_x = 0$ :

$$\left. \begin{aligned} \mathcal{E}_x &= A_{4j} (\cos \rho_x x + S_j \sin \rho_x x) e^{-i(\sigma_y y + \beta z)} \\ \mathcal{H}_x &= -i \frac{\omega \epsilon_0 \sigma_y n_2^2}{\rho_x \beta} A_{4j} (\sin \rho_x x - S_j \cos \rho_x x) e^{-i(\sigma_y y + \beta z)} \end{aligned} \right\} \text{for } x \geq 0. \quad (55)$$

$$\left. \begin{aligned} \mathcal{E}_x &= A_{4j} \left( \cos \sigma_x x + \frac{\rho_x}{\sigma_x} S_j \sin \sigma_x x \right) e^{-i(\sigma_y y + \beta z)} \\ \mathcal{H}_x &= -i \frac{\omega \epsilon_0 \sigma_y n_1^2}{\sigma_x \beta} A_{4j} \left( \sin \sigma_x x - \frac{n_2^2 \sigma_x}{n_1^2 \rho_x} S_j \cos \sigma_x x \right) e^{-i(\sigma_y y + \beta z)} \end{aligned} \right\} \text{for } x \leq 0. \quad (56)$$

Equations (41) and (50) determine the relations among the components of the propagation constant. The ranges of  $\sigma_x$  and  $\sigma_y$  are limited to the regions where  $\rho_x$  is real and positive. This remark applies also to case (iii).

Two sets of mutually orthogonal modes result if we choose

$$S_1 = 0 \quad (57)$$

and

$$S_2 = \infty. \quad (58)$$

The amplitude coefficients are

$$A_{41}^2 = \frac{2\rho_x \sigma_x^2 \sqrt{\mu_0 / \epsilon_0} \beta P}{\pi^2 k (n_2^2 \sigma_x + n_1^2 \rho_x) (\beta^2 + \sigma_y^2)} \quad (59)$$

and

$$S_2^2 A_{42}^2 = \frac{2n_1^2 \sigma_x \rho_x^2 \sqrt{\mu_0 / \epsilon_0} \beta P}{\pi^2 n_2^2 k (n_2^2 \sigma_x + n_1^2 \rho_x) (\beta^2 + \sigma_y^2)}. \quad (60)$$

$\epsilon_0$  is the permittivity of vacuum.

## REFERENCES

1. P. W. Smith, "A Waveguide Gas Laser," *Appl. Phys. Lett.*, **19**, No. 5 (September 1971), pp. 132-134.
2. J. Stone, C. A. Burrus, A. G. Dentai, and B. I. Miller, "Nd:YAG Single-Crystal Fiber Laser: Room Temperature CW Operation Using A Single LED as an End Pump," *Appl. Phys. Lett.*, **29**, No. 1 (July 1976), pp. 37-39.
3. D. Marcuse, "Steady-State Losses of Optical Fibers and Fiber Resonators," *B.S.T.J.*, this issue, pp. 1445-1462.
4. D. Marcuse, *Theory of Dielectric Optical Waveguides*, New York: Academic Press, 1974.
5. A. W. Snyder and J. D. Love, "Tunneling Leaky Modes on Optical Waveguides," *Opt. Commun.*, **12**, No. 3 (November 1974), pp. 326-328.
6. A. W. Snyder, "Leaky-Ray Theory of Optical Waveguides of Circular Cross Section," *Appl. Phys.*, **4**, 1974, pp. 273-298.
7. D. Marcuse, *Light Transmission Optics*, New York: Van Nostrand Reinhold, 1972, p. 18, eq. (1.6-14).
8. D. Marcuse, "Radiation Losses of the HE<sub>11</sub> Mode of a Fiber with Sinusoidally Perturbed Core Boundary," *Appl. Opt.*, **14**, No. 12 (December 1975), pp. 3021-3025.
9. Ref. 7, pp. 12-13, eqs. (1.4-16) through (1.4-19).

## Novel Technique for Measuring the Index Profile of Optical Fibers

By J. A. ARNAUD and R. M. DEROSIER

(Manuscript received August 30, 1976)

*A novel technique for measuring the refractive index profile of optical fibers is demonstrated, which offers substantial advantages over alternative methods. The method consists of illuminating a small area of the fiber core and measuring the total transmitted power. The transmission of leaky modes is accounted for in the manner reported previously by other authors. The index profiles of germanium-doped fibers obtained by this technique are compared to interferometric measurements. The resolution is shown to be limited by wave optics effects to about  $\lambda_0(4n\sqrt{2\Delta})^{-1}$ , where  $\Delta \equiv \Delta n/n$ . The distortion of the index profile as the wavelength varies and wave-optics effects are investigated.*

### I. INTRODUCTION

The accurate measurement of index profiles at various wavelengths may help design multimode fibers whose transmission capacity would go well beyond what has been presently achieved. Indeed, numerical calculations and theoretical analyses<sup>1,2</sup> show that there exist index profiles (usually not power-law profiles), which, for quasi-monochromatic sources, provide transmission capacities of about  $1.6/\Delta^2$  Mb/s  $\times$  km, where  $\Delta \equiv \Delta n/n$ . Measured transmission capacities are about 10 times smaller. To determine the optimum profiles, it is indispensable to know the variation of  $dn/d\lambda_0$  (where  $\lambda_0$  is the operating wavelength) as a function of  $n$  for the class of materials considered with an accuracy of about 1 percent. The required variation of  $dn/d\lambda_0$  as a function of  $n$  can be obtained, in principle, from measurements on bulk samples (e.g., Ref. 3). We question, however, whether measurements on bulk samples are applicable to the fiber material with sufficient accuracy. For that reason and also because the fabrication and measurement of bulk samples is time-consuming, the direct measurement of index profiles at various wavelengths is highly desirable. Once the optimum profile applicable to the class of materials considered has been determined, we measure the departures of the profile  $n(r)$  of the fabricated

fiber from optimum. Very small deviations may degrade considerably the transmission capacity.

An interesting experimental technique for measuring circularly symmetric index profiles has been proposed by Gloge and Marcattili.<sup>4</sup> The index profile is obtained by measuring with a pin hole the radial distribution of intensity in fibers excited by Lambertian (e.g., thermal) sources. In a series of careful measurements, Sladen, Payne, and Adams<sup>5</sup> have shown that good agreement can be obtained between the intensity in the fiber core and the index profile obtained by interferometry provided the non-zero transmission of the leaky modes is accounted for. If this correction is made, the fiber samples need not be larger than about 1 meter, and may be as small as 1 cm.

The technique that we describe in the present paper, which we call the transmission technique, is related to the near-field technique discussed above, but it differs from it in many significant ways. Arnaud<sup>6</sup> has shown that, if we illuminate a small area of the fiber core (perhaps of the order of  $(\lambda_0^2$  at  $x, y$ , the total transmitted power is, for sufficiently long fibers, proportional to  $n^2(x, y) - n_c^2$ , where  $n(x, y)$  denotes the refractive index at  $x, y$ , and  $n_c$ , the cladding index. The proof is straightforward: The rays radiated from the illuminated area have an almost uniform distribution in the plane  $k_x, k_y$ , where  $k_x, k_y$  denote the transverse components of the wave vector  $\mathbf{k}$ . Because of the relation  $k_x^2 + k_y^2 + k_z^2 = k^2(x, y) \equiv (\omega/c)^2 n^2(x, y)$ , which holds between the rectangular components of  $\mathbf{k}$ , and because only rays whose  $k_z$  is larger than  $k_c$  are transmitted without loss, the power transmitted through long fibers is proportional to

$$k_x^2 + k_y^2 = k^2(x, y) - k_c^2 \equiv \text{index profile} \quad (1)$$

(see Fig. 1). The rays in the dotted area in Fig. 1b leak away if the fiber is sufficiently long. Otherwise their contribution to the total transmitted power needs to be subtracted in the manner reported in Ref. 5. If the spot size is less than  $\lambda_0$ , we may use as a source either a (coherent) laser or a (spatially incoherent) LED. If, however, the spot size is significantly larger than  $\lambda_0$ , it is essential to use near-Lambertian sources such as LEDs. Indeed, coherent beams of large cross section would excite predominantly paraxial rays. This would require introducing additional correction factors.

In the present paper, we discuss the principles and limitations of the method, and we present experimental results. The transmission method gives results that are, in principle, identical to the near-field measurements described in Ref. 5. The main advantage of the transmission method, compared with alternative methods, including the near-field technique, is that it is extremely easy to implement. The results are highly reproducible to better than one part in 1000.

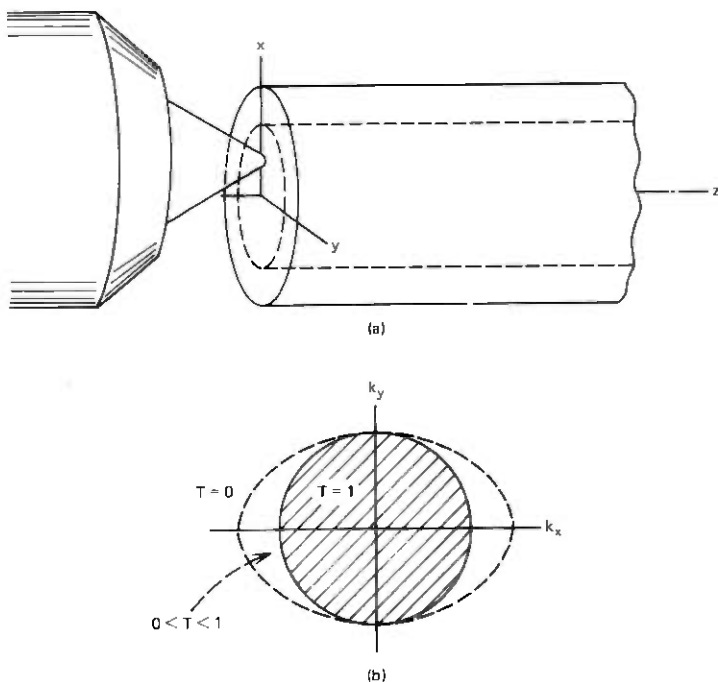


Fig. 1—(a) In the transmission method, the microscope objective illuminates a small area of the fiber end of the order of  $\lambda_0^2$ . (b) The intensity is assumed uniform in the  $k_x, k_y$  space. For long fibers, only the rays in the shaded area are transmitted. For short fibers, the rays in the dotted area may also be transmitted (leaky rays).  $T$  denotes the power transmission.

## II. EXPERIMENTAL CONDITIONS

To implement the proposed technique, all we need is an ordinary microscope, a high-radiance LED (or a laser), and a detector. The numerical aperture (NA) of the microscope objective should be at least twice as large as that of the fiber. One end of the fiber is properly broken or polished and centered approximately under the microscope objective at focus. When the microscope eyepiece is replaced by a LED, a small spot of infrared radiation illuminates the fiber end. As we have indicated in the introduction, the power detected at the other end of the fiber is proportional to  $n^2(x, y) - n_c^2$ , where  $n(x, y)$  denotes the index at the point  $x, y$  of the fiber where the light is focused, and  $n_c$  the cladding index. To obtain the index profile, we may scan either the fiber, with a total motion of about  $100 \mu\text{m}$ , or the source, with a total motion of about  $3 \text{ mm}$ . The arrangement shown in Fig. 2 incorporates a beam splitter (1) to allow the fiber to be observed during scanning. (A second beam splitter, which combines the light from two LEDs, is shown in Fig. 2. It is used only for dispersion measurements.) Some infrared LEDs radiate red light with sufficient intensity for direct visual

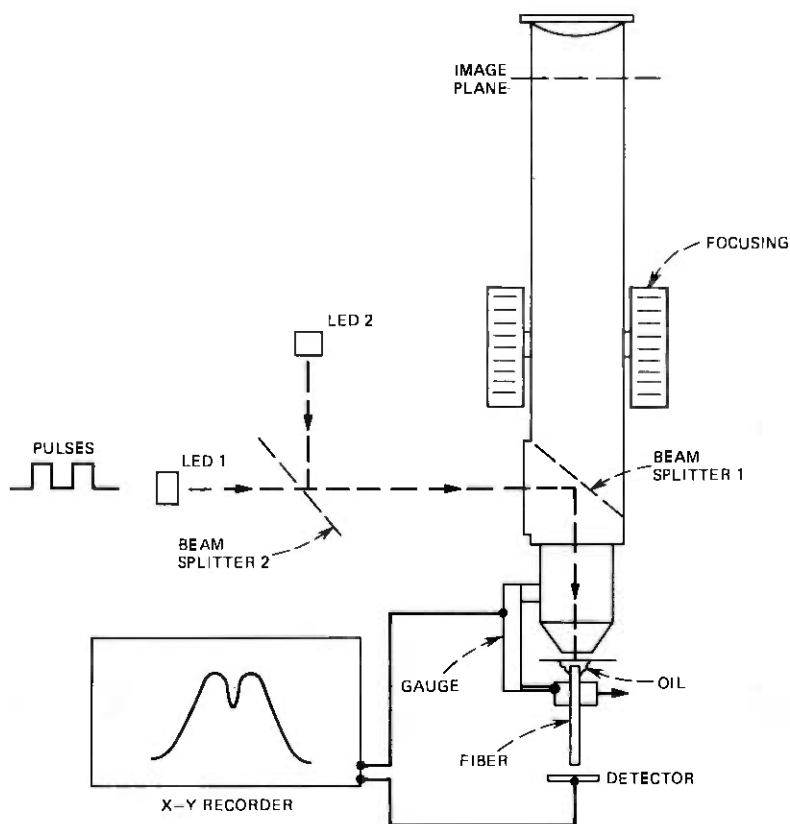


Fig. 2—Experimental setup of the transmission technique. The fiber is scanned mechanically and its motion is recorded with a gauge. Two LEDs are used for dispersion measurement.

observation. For LEDs at longer wavelengths, an image converter is necessary. Note that the focal length of microscope objectives may be slightly different for the red light and for the infrared light. In the arrangement in Fig. 2, it is convenient to have the distance between the LED source and the microscope objective equal to the distance between the focal plane of the eyepiece and the microscope objective. This avoids the need for refocusing when the objective is changed from low to high magnification. To obtain good resolution, it is desirable that the LED act as a point source; that is, that the apparent size of the LED, demagnified by the microscope objective, be smaller than the diffraction-limited spot  $\approx \lambda_o/NA$ , defined by the numerical aperture of the microscope objective. An apparent emissive diameter of  $25 \mu\text{m}$  (before demagnification) is adequate. The experimental setup is shown in Fig. 3. The LED source (not visible) is supported by the

*xyz* microscope stage at the left. The angular orientation of the fiber under the microscope objective can be varied. Figure 3 shows the differential micrometer that drives the fiber and the gauge that measures its displacement with respect to the microscope objective.

The advantages of the proposed technique compared to the more conventional near-field technique are many:

- (i) In the near-field method, the source is required to be Lambertian and uniform over the full cross section of the fiber core. As pointed out in Ref. 5, this condition is in fact difficult to

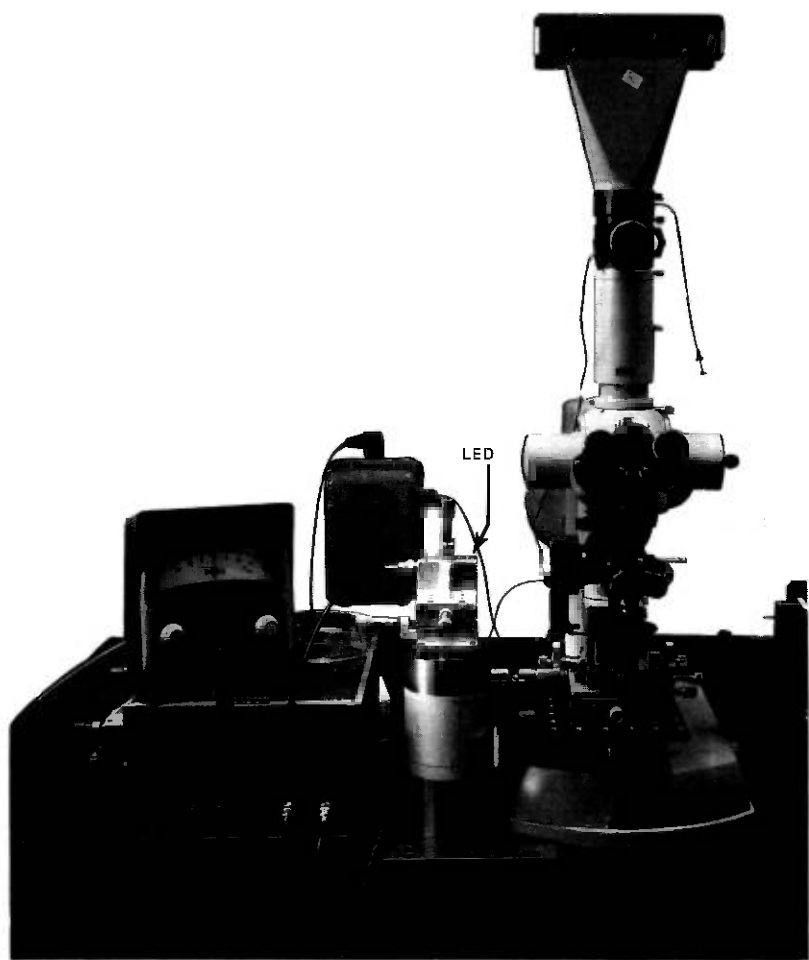


Fig. 3—Photograph of the experimental setup. The LED (not seen) is supported by the *xyz* stage on the left.

achieve with LEDs. The authors in Ref. 5 thus found it necessary to use thermal sources instead of LEDs. Thermal sources (e.g., tungsten wires) provide poor signal-to-noise ratios when the spectral width is restricted by narrowband interference filters. In the transmission method, we require the  $NA$  of the microscope objective to be significantly larger than that of the fiber (at least for coherent sources), but the requirement concerning the spatial uniformity of the source is relaxed. In some sense, the requirement of spatial uniformity is transferred from the source, where it is difficult to achieve, to the detector, where the condition is easily met.

- (ii) The optics are much simplified. Only a single microscope objective is needed instead of (typically) three. Thus, the signal-to-noise ratio is improved.
- (iii) Near-field measurements provide the shape of the index profile, but not the absolute value of  $\Delta n(r) = n(r) - n_c$ , where  $n_c$  denotes the cladding index. In the transmission method, we can calibrate  $\Delta n$  by measuring the intensity radiated axially by the microscope objective. This calibration technique will be discussed in more detail in the next section.
- (iv) The transmission method can be combined with the Fresnel-reflection technique (for a recent report of the Fresnel-reflection technique, see Ref. 7). To implement this modification, we replace the microscope eyepiece in Fig. 2 with a detector.

An important drawback that applies to both the transmission and near-field methods is encountered when the fiber exhibits a low-index region near the cladding. In that case, some modes (besides the so-called weakly leaky modes) are leaking very slowly, and the interpretation of the measurements becomes ambiguous. The resolution offered by these methods may be marginal when the fiber profile exhibits very fast fluctuations. Note also that, for noncircularly symmetric profiles, the correction factors for leaky rays have not been worked out. If the deviation from perfect circular symmetry is small, however, the correction factor given in Ref. 5 may be used.

### III. INCIDENT BEAM PATTERN AND INDEX CALIBRATION

To make precise measurements, the radiation from the microscope objective should approximately obey Lambert's law, at least for angles  $\alpha$  to the axis that are less than  $\sqrt{2}\Delta$ . To verify that this law is approximately obeyed, we translate the detector in front of the microscope objective at some distance  $d \gg \lambda_0$  from the focal point. Ideally, the variation of the detected power as a function of the distance  $r$  from

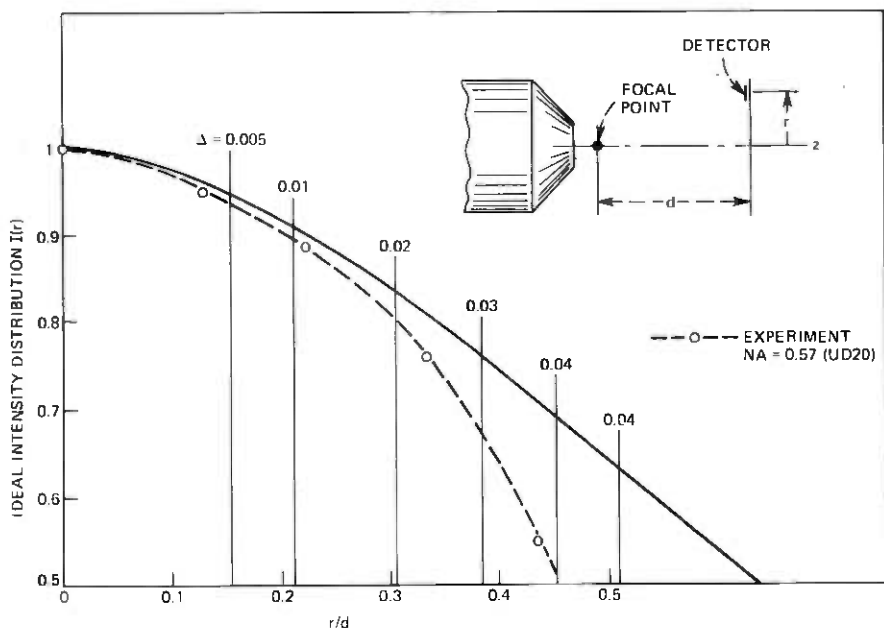


Fig. 4—The curve shown is the desired radiation pattern from the microscope objective. It is sufficient if this law be obeyed from  $r/d = 0$  to the value corresponding to the  $\Delta$  of the fiber (e.g.,  $r/d < 0.3$  if  $\Delta = 0.02$ ). The experimental points were measured using a Leitz UD 20,  $NA = 0.57$  microscope objective.

axis should be\*

$$P(r) = \cos^4 \alpha = (1 + r^2/d^2)^{-2}. \quad (2)$$

The desired variation of  $P$  with  $r$  in (2) is shown in Fig. 4. The maximum value of  $r/d$  corresponding to a particular  $\Delta$  is given by

$$r/d = (NA^{-1} - 1)^{-1/2} \quad (3a)$$

$$NA = n_o \sqrt{2\Delta}. \quad (3b)$$

The values of  $r/d$  are shown in Fig. 4 for typical values of  $\Delta$  and  $n_o = 1.45$ .

Let us now consider the problem of calibrating  $\Delta n$ . This is done by measuring the intensity radiated axially by the microscope objective.

\* This result can be obtained by inverting eq. (5.246) of Ref. 6 and noticing that when the radiation is uniformly dense in the  $k_x, k_y$  plane (the transverse components of the wave vector), it remains uniformly dense after refraction at any plane interface perpendicular to the  $z$  axis. To show that, set in eq. (4.167) of Ref. 6:  $dk_x/dz = dk_y/dz = 0$  (Descartes-Snell law) and find that  $f(k_x, k_y, x, z) = g(k_x, k_y)h(x, z)$  is a solution of the Liouville equation for any differentiable functions  $g$  and  $h$ . Thus, if  $f$  is independent of  $k_x$  and  $k_y$  at  $z = 0$ , as we have assumed (Lambert's law), it remains independent at  $k_x, k_y$  after any number of refractions.

Let the power detected in front of the microscope objective be denoted  $P_o$  and the power transmitted through the fiber for near-axial excitation be denoted  $P$ . If the detector radius is denoted  $\rho$  and its distance from the microscope objective focal point is  $d$ , the  $\text{NA} = n_o\sqrt{2\Delta}$  of the fiber is given by

$$\text{NA} = (\rho/d)\sqrt{P/\eta P_o}, \quad (4)$$

where

$$\eta = [4n_o/(n_o + 1)^2]^2 \quad (5)$$

accounts for the Fresnel reflection at both ends of the fiber. This expression for  $\eta$  is not rigorous, but it is sufficiently accurate for our application. With sufficient accuracy, we can set  $n_o = 1.45$ . Then,  $\eta = 0.93$ . Convenient values for  $d$  and  $\rho$  are  $d = 10$  mm and  $\rho = 1$  mm, respectively. We thus obtain from (4) and (5)

$$\text{NA} = 0.104\sqrt{P/P_o} \quad (6a)$$

$$\Delta = 0.00255(P/P_o). \quad (6b)$$

It is, of course, necessary to have good breaks at both ends of the fiber. We have assumed that the fiber loss is negligible; this is the case for most fibers if the length is 1 m or less.\*

A more conventional technique for evaluating  $\Delta$  consists of measuring the far-field pattern when the fiber is illuminated on or near axis. We have

$$\Delta = \frac{1}{2}(\text{NA}/n_o)^2, \quad (7)$$

where  $\text{NA}$  denotes the sinus of the maximum radiation angle in air, defined typically at the  $-3$  dB point from maximum intensity.

The core radius,  $a$ , of the fiber is best obtained by observing the fiber tip with a microscope. From the values of  $\Delta$ ,  $a$ , and  $\lambda_o$ , the  $V$ -number is calculated according to

$$V = (2\pi a/\lambda_o)\text{NA}. \quad (8)$$

#### IV. CORRECTION FOR LEAKY RAYS

If the fiber is not very long, the leaky modes excited by the source are not completely attenuated. They can be accounted for in the manner described in Ref. 5. Specifically, the index profile  $n^2(r) - n_c^2$  is obtained by dividing the detected power  $P(r)$  by the correction factor

\* With some high NA objectives ( $\text{NA} \approx 0.8$ ), spurious peaks are observed in the far-field pattern due to diffraction effects, even with LED sources. Thus, the calibration of  $\Delta$  should be made with lower NA objectives, e.g.,  $\text{NA} \approx 0.5$ . These spurious peaks do not appear to affect the profile measurements, but they prevented us from making a precise comparison between the two techniques described here for measuring  $\Delta$ .

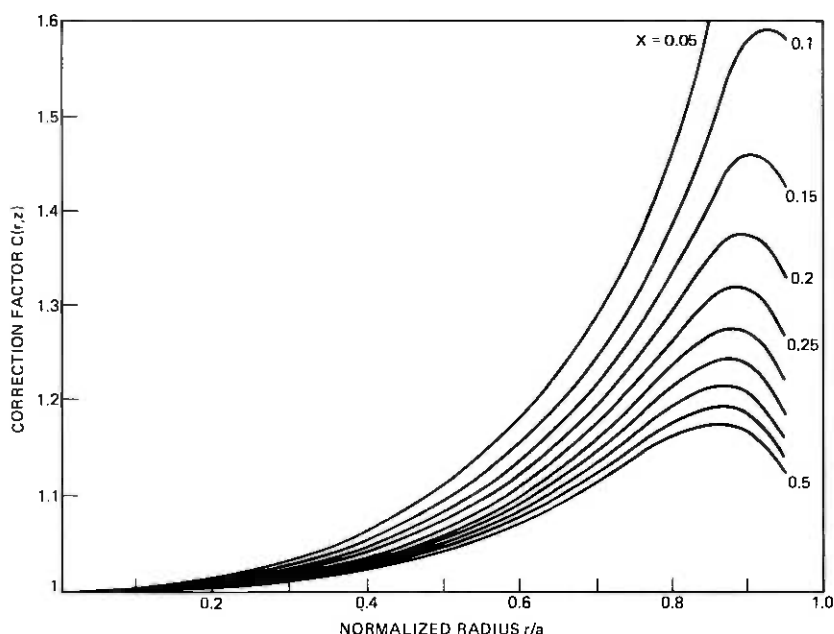


Fig. 5—Correction factor for leaky rays.<sup>5</sup> The  $X$  parameter is defined in the main text as  $X = V^{-1} \log_e(L/a)$ , where  $V$  denotes the  $V$ -number of the fiber,  $L$ , the fiber length, and  $a$ , the core radius. The measured power should be divided by  $C$ . These curves are applicable to near-square-law fibers.

$C(r)$  given in Fig. 5.<sup>5</sup> In this figure, the parameter  $X$  is defined as

$$X = V^{-1} \log_e(L/a), \quad (9)$$

where  $L$  denotes the fiber length, and  $V$  the fiber  $V$ -number defined in (8).

Note that the correction is negligible near the fiber axis, but may be as large as 30 percent at  $r \approx 0.8a$  for typical fiber lengths. Strictly speaking, the correction factor depends on the profile of the fiber. The curves in Fig. 5 are applicable to near square-law profiles. However, the correction factor turns out not to be very sensitive to the exact profile. Thus, for most high-transmission capacity fibers, the square-law-profile correction factor may be sufficiently accurate. If greater accuracy is required, we may use an iteration procedure. Because this procedure is rather involved, it will not be discussed here.

## V. REFRACTIVE-INDEX PROFILE MEASUREMENTS

The measurement technique described in previous sections has been applied to graded-index fibers. Let us first make a few general comments concerning the experimental technique and the results. The

results obtained are highly reproducible to better than one part in 1000 even after a few hours if the fiber tip is protected by a glass plate and an index-matching fluid. The axial index dip characteristic of germanium- (or phosphor-oxide-) doped fibers is very useful to define the fiber center and achieve optimum focusing.

### 5.1 Comparison with near-field and interferometric measurements

Near-field measurements<sup>5</sup> were made on a graded-index fiber. The setup is shown schematically in Fig. 6a. A Burrus-type high-radiance LED with an apparent emissive diameter of  $50\ \mu\text{m}$  is imaged with unity magnification on the end of the fiber under test with a pair of microscope objectives ( $20\times$ ,  $\text{NA} = 0.4$ ). The other end of the fiber is imaged with a microscope objective ( $40\times$ ,  $\text{NA} = 0.65$ ) on a scanned small-area detector. The magnification, measured with a reticle, is equal to 54. Focusing is adjusted to make the details of the index profile as sharp as possible. The variation of detected power as a function of the transverse displacement of the detector is shown in

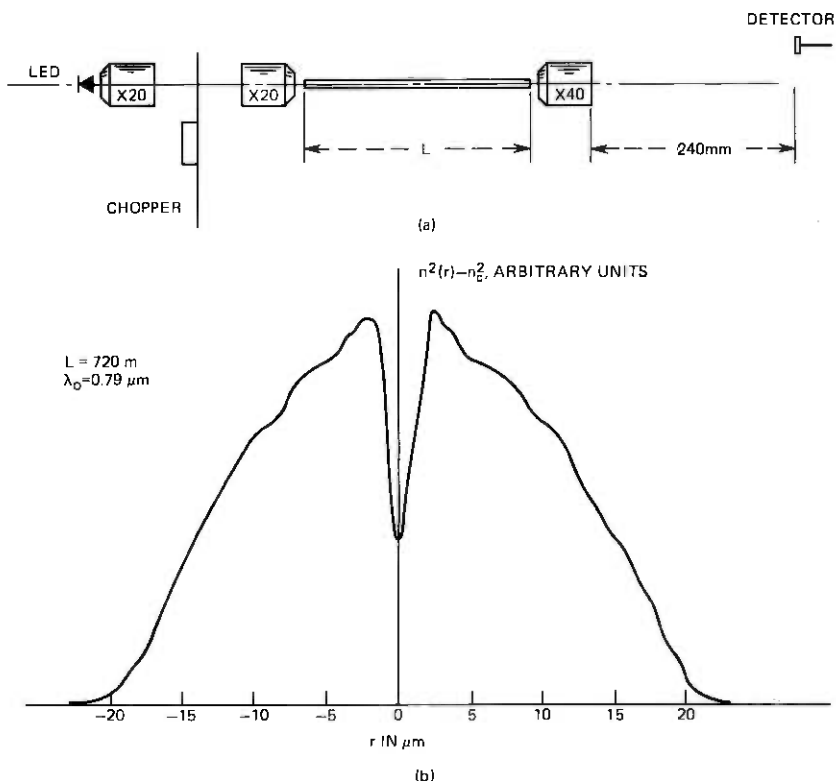


Fig. 6—Near-field measurement on a germanium-doped, graded-index fiber.

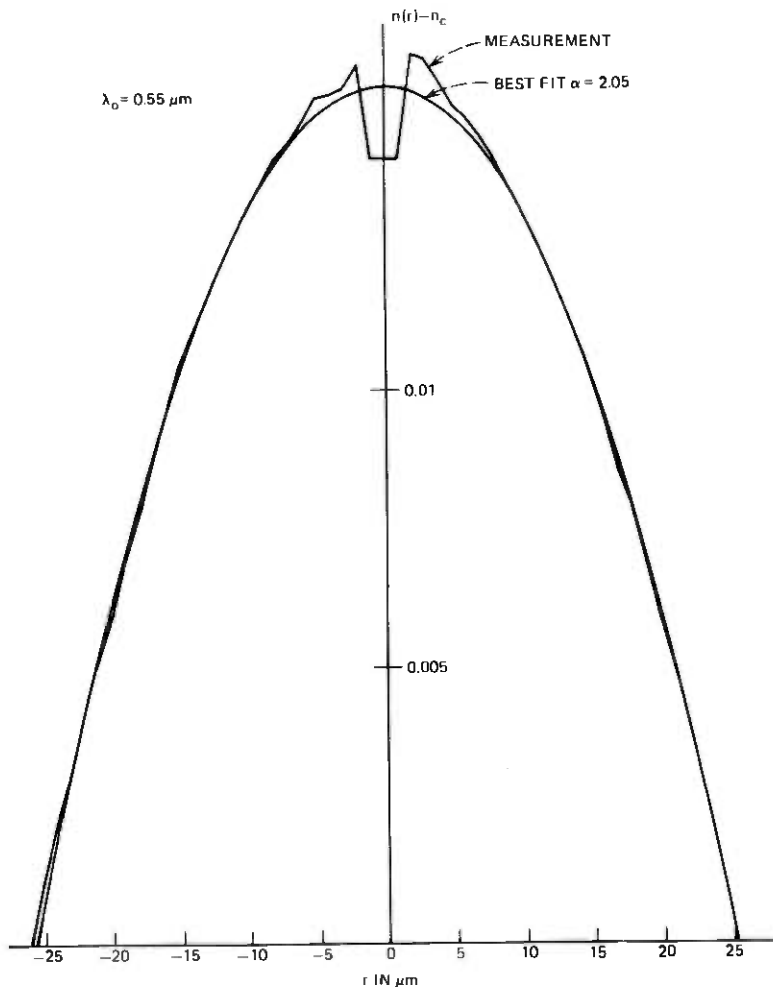


Fig. 7—Interferometric profile of the fiber in Fig. 6,  $\lambda_0 = 0.55 \mu\text{m}$ .  $NA = 0.21$ ,  $\Delta = 0.0107$ .<sup>8</sup>

Fig. 6b for a fiber length  $L = 720 \text{ m}$ . For such long lengths, the leaky-ray correction is small. Because of evaporation of germanium during the collapse of the preform, the material on axis is probably almost pure silica. The observed reduction of  $\Delta n$  is, at most,  $\frac{2}{3}$ . This discrepancy reflects the inherent limitation in resolution of near-field and transmission techniques. We attribute small oscillations on each side of the central dip to wave-optics effects. They are qualitatively similar to the ones calculated for a dielectric slab in Appendix A. The slow modulation reflects the presence of diffused steps. The interferometric measurement<sup>8</sup> is shown in Fig. 7.

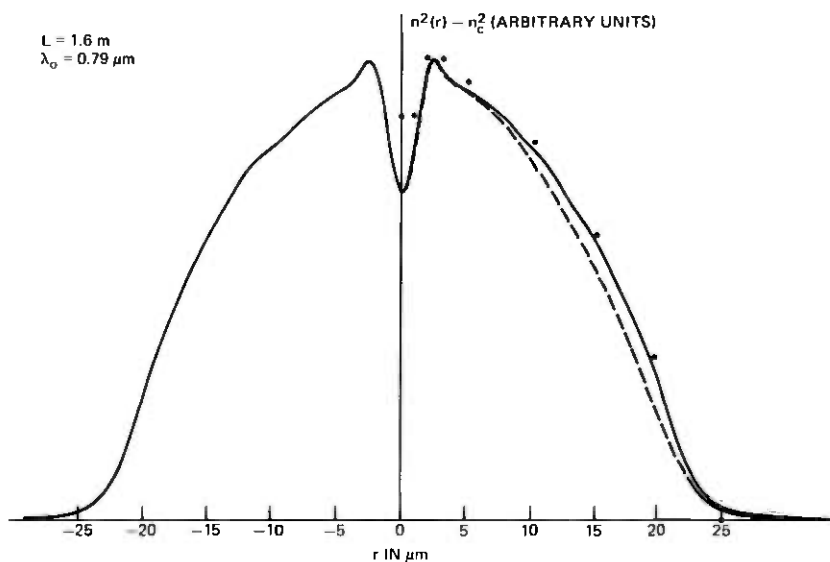


Fig. 8—Profile of the fiber in Figs. 6 and 7 obtained with the transmission technique. Uncorrected: solid line. Corrected for leaky rays: dashed line. Interferometric measurements from Fig. 7: dots. The measured  $\Delta$  at  $\lambda_0 = 0.79 \mu\text{m}$  is 0.0104.

The index profile obtained with our transmission technique is shown in Fig. 8. The  $\Delta$  of the fiber was measured from the far-field pattern, as described in Section III. We measured  $\Delta = 0.0104$ , in good agreement with the value obtained by interferometry. From a core radius  $a = 24 \mu\text{m}$ , we calculate from (8) a  $V$ -number:  $V = 40$ . The fiber length is 1.6 m. Thus, the  $X$ -parameter in (9) is  $X = 0.28$ . The corrected profile, obtained by dividing the measured power by the correction factor  $C$  in Fig. 5, is shown as a dashed line in Fig. 8. The result of interferometric measurements is shown by dots for comparison. Aside from the depth of the central dip, a significant difference between the dashed curve (corrected transmission profile) and the dots (interferometric measurement). Such a discrepancy may be in part attributed to the lack of perfect circular symmetry of the fiber.

### 5.2 Measurement of the lack of circular symmetry

The (uncorrected) transmission profile of germanium-doped fiber was measured in two perpendicular azimuthal directions, labeled  $0^\circ$  and  $90^\circ$ , respectively. These two profiles are shown in Fig. 9 as solid lines and dashed lines, respectively. The measured  $\Delta$  and  $NA$  parameters are given in the figure caption. We conjecture that, for the small deviations from circular symmetry exhibited by the fiber investigated, the correction factor in Fig. 5 is applicable.

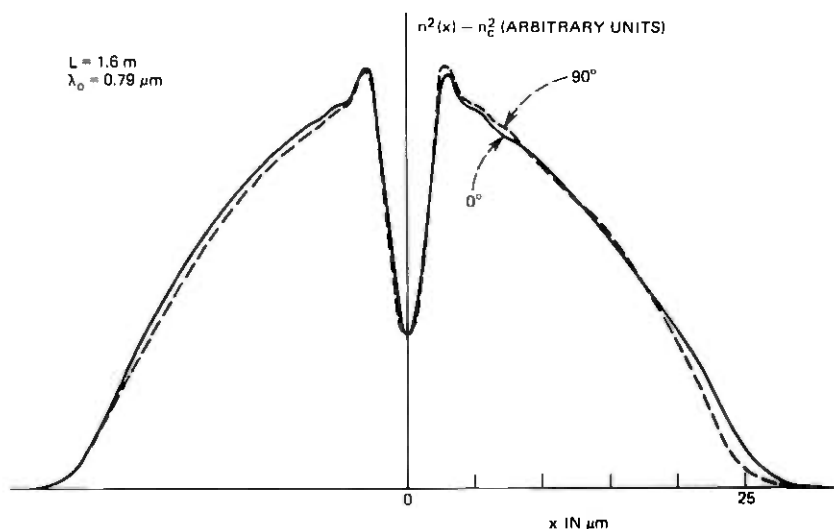


Fig. 9—Uncorrected profile of a germanium-doped, graded-index fiber in two azimuthal planes ( $0^\circ$  and  $90^\circ$ ). The measured  $NA$  is 0.202,  $\Delta = 0.00974$ ,  $L = 1.6$  m.

### 5.3 Measurement of a double-hump profile fiber

An attempt was made by MacChesney<sup>9</sup> to suppress the central index dip of germanium-doped fibers by increasing the amount of germanium halides during the final stage of fabrication of the preform. The profile of a fiber of that type was measured by interferometry<sup>8</sup> and by our transmission technique. Both techniques clearly show that there is a large *peak* of index near the center of the fiber. However, the transmission technique shows that the dip in the center did not disappear (hence, the name "double-hump" given to the profile of that fiber). This central dip is not seen on the interferogram. The combination of a peak and a dip is unlikely to improve the fiber transmission. A much better compensation of the central dip will be reported later in this paper.

### 5.4 Measurement of noncircularly symmetric profiles

The theoretical result in (1) shows that the transmission technique is applicable, in principle, to noncircularly symmetric profiles, as well as to circularly symmetric profiles. A preform that accidentally collapsed flat<sup>10</sup> has been pulled at our request into a fiber and measured. The uncorrected profiles are shown in Fig. 10. Because the correction for the leaky rays has not been made, the curves in Fig. 10 are only indicative of the index profile.

$\lambda_o = 0.79 \mu\text{m}$   
 NA OBJECTIVE = 0.85  
 $L = 2.45 \text{ m}$   
 NA FIBER = 0.38

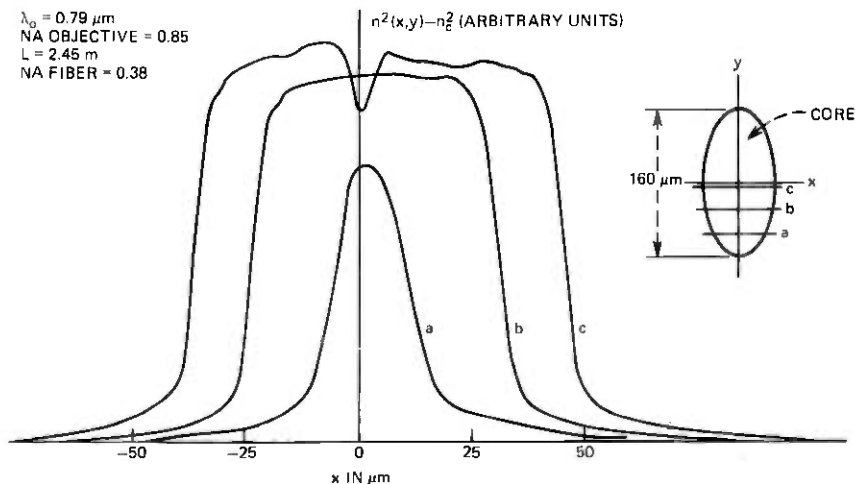


Fig. 10—Profile of a fiber with near-elliptical core (uncorrected).

### 5.5 Profile distortion

One of the most interesting and intriguing questions is whether index profiles get significantly distorted as the wavelength varies (independently of possible changes of scale). Fleming's measurements on bulk samples of germanium-doped silica<sup>3</sup> clearly indicate that profiles get distorted significantly as the wavelength varies. This effect, however, has not been observed before on fibers. We report here preliminary measurements of profile distortion. The necessary formulas are relegated to Appendix B.

Figure 11 shows the profiles measured with the transmission method at two wavelengths:  $\lambda_o = 0.79 \mu\text{m}$  and  $\lambda_o = 0.9 \mu\text{m}$ , on a germanium-doped, graded-index, large NA fiber. Note first that the resolution (indicated by the depth of the central dip) is slightly poorer at the longer wavelength. When the scanning is made slightly off-center to avoid the central dip and the two profiles are normalized to unity on axis, the differences between the two profiles are found to be extremely small yet significant. To exhibit this difference with good accuracy, we have combined the light from the two LEDs with beam splitter in Fig. 2 number 2. Square pulses are applied to the LEDs. The positive parts of the pulses drive one LED and the negative parts drive the other. The levels are adjusted to have equal detected powers on the fiber axis, and therefore, zero signal on the lock-in amplifier. The difference between the two normalized profiles is plotted in Fig. 12 (curve b). More precisely, we have plotted in Fig. 12 the "profile distortion"  $d \equiv \lambda_o \partial \eta / \partial \lambda_o$ , where  $n \equiv N/2\Delta$  and  $N \equiv 1 - n^2/n_o^2$ , as a function of  $r/a$ . The accuracy of this curve is difficult to ascertain at

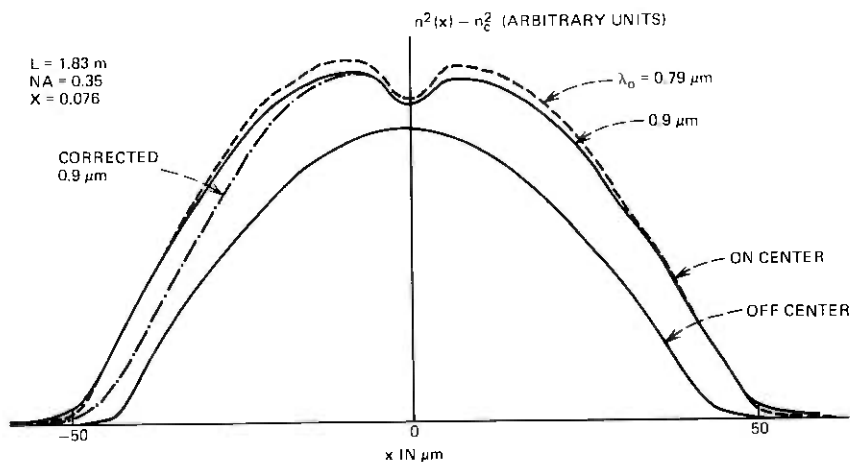


Fig. 11—Profile of a germanium-doped, graded-index fiber at two wavelengths (a):  $\lambda_0 = 0.79 \mu\text{m}$ , (b)  $\lambda_0 = 0.9 \mu\text{m}$ , (c)  $\lambda_0 = 0.79$ , scanning slightly off-center (obtained with the transmission technique and an objective NA = 0.85).

the moment. Part of the observed change of the shape of the index profile may be attributed to the dependence of the leaky-ray correction factor on wavelength.

The variation of  $d$  as a function of  $r/a$  can also be calculated from Fleming's measurements on bulk samples, as explained in detail in Appendix B. The result of this calculation is shown in Fig. 12 (curve a). There is no close agreement between curve a and curve c. However, they are comparable in magnitude. Thus, measurement of very slight changes of profile with wavelength, such as are shown in Fig. 12, are of great practical importance.

## VI. CONCLUSION AND PROPOSALS FOR FUTURE WORK

We have proposed and demonstrated a novel technique for measurement of the index profile of multimode fibers. Conceptually, this technique is related to the near-field technique previously demonstrated by Sladen et al.<sup>5</sup> (near-field technique). From a practical point of view, however, our technique is quite different, since it does not require Lambertian sources. In particular, lasers can be used. We have found that the measured profiles are highly reproducible, to better than one part in 1000 over periods of hours. Index profile measurements can be obtained in a few minutes including fiber-end preparation. The agreement between our technique and interferometric measurements leaves something to be desired. The discrepancy, however, may be attributed to the lack of perfect circular symmetry of the fibers investigated. Theoretical considerations show that the res-

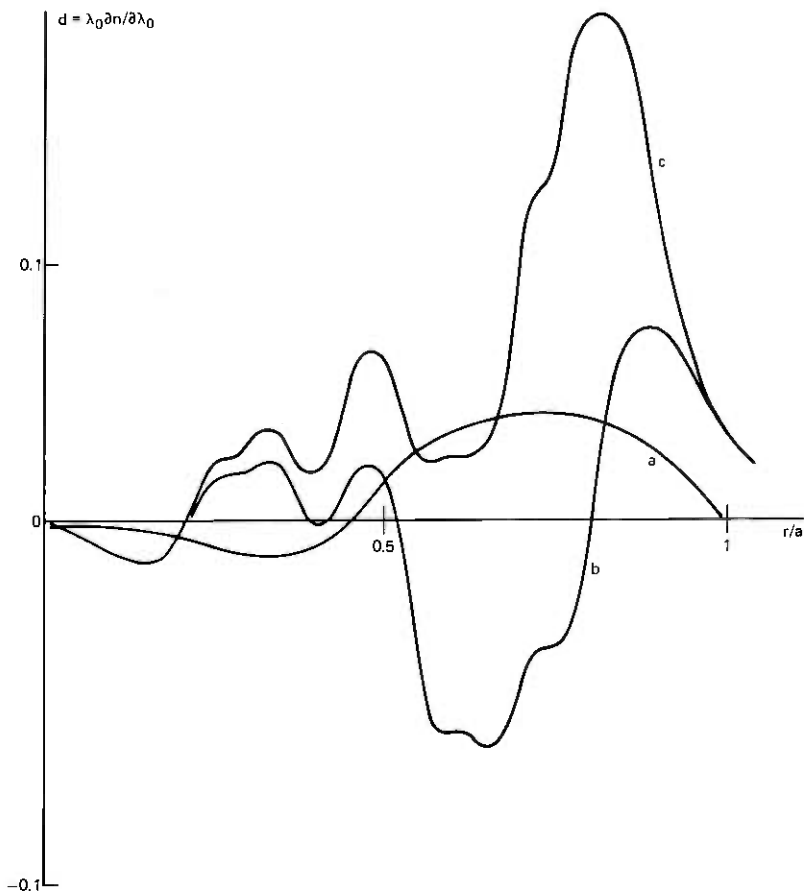


Fig. 12—Profile distortion. Curve (a) is calculated from Fleming's measurements on bulk samples as reported in Ref. 3 (Fig. 1, curve labeled  $\lambda = 0.9 \mu\text{m}$ ). Curve (b) is the difference between the normalized profiles at  $\lambda_0 = 0.79$  and  $0.9 \mu\text{m}$ . Curve (c) is the same as curve (b) corrected for the leaky rays.

olution is about  $\lambda/4\sqrt{2\Delta}$ . For a typical value  $\Delta \approx 0.015$ , this resolution is about the free-space wavelength  $\lambda_0 \approx 1 \mu\text{m}$ . This appears to be sufficient for most practical purposes.

Comparison of depths of central-index dips suggests that the transmission technique (and the near-field technique as well) provides better resolution than interferometric techniques. We have presented preliminary evidence for the distortion of the index profile as the wavelength varies (profile distortion), an effect that was inferred previously only from measurements on bulk samples. Theories that neglect profile distortion may be in considerable error.

We shall now make a few suggestions for improvement of the

measurement technique. Oil-immersed microscope objectives would be useful to prevent interference effects between the objective and the fiber tip when monochromatic laser sources are used. The processing of the experimental data can be considerably improved if the lock-in amplifier and the gauge have digital readouts. The correction factor  $C$ , given approximately in Fig. 5, should be recalculated and supplied in digital form. A better approach would consist of calculating  $C$  from the apparent measured profile and iterating. These iterations, presumably, can be effected with modest computing time. Noncircularly symmetric profiles can be corrected, in principle, but the correction problem has not been solved yet. Finally, we attempt to deconvolve the wave-optics effects (discussed in Appendix A) that are most conspicuous in regions where the index varies rapidly. The possibility of performing this deconvolution is intriguing, but the analytical problem remains, to our knowledge, unresolved. The case of fibers with an index barrier between the core and the cladding requires further analysis.

Among all the index-profile measurement techniques that have been proposed so far, the transmission technique that we have described here appears to be the easiest to implement and the most reliable. Improvement in data processing should make the results quite accurate in most cases.

## APPENDIX A

### Wave Optics Effects

The result (given in the main text) that the intensity distribution in the cross section of long multimode fibers is proportional to  $k^2(x, y) - k_s^2$ , where  $k(x, y) \equiv (\omega/c)n(x, y)$  denotes the core wave number and  $k_s \equiv (\omega/c)n_c$  the cladding wave number, is based on ray optics (WKB approximation) and on the assumption that rays whose axial wave number ( $k_z$ ) is less than  $k_s$  are radiating away and do not contribute to the total intensity. Because the number of trapped modes carried by real fibers is finite, the intensity distribution does not follow the fine details of the index profile. This is because the optical field cannot vary in transverse directions faster than  $(\sin k_{z \max} x)$  where  $k_{z \max} = (\omega/c)n_o \sqrt{2\Delta}$  denotes the maximum value of the transverse wave number,  $n_o$  the index on axis, and  $\Delta \approx \Delta n/n$ . According to the above formula, the smallest distance between nodes and peaks of the irradiance in the fiber core is

$$\Delta x \approx \lambda_o / (4n_o \sqrt{2\Delta}). \quad (10)$$

Equation (10) provides an estimate of the resolution afforded by the

method. For example, if  $\lambda_0 = 1 \mu\text{m}$ ,  $n_0 = 1.45$ , and  $\Delta = 0.01$ , the resolution is, according to (10),  $\Delta x \approx 1.25 \mu\text{m}$ .

To get a more precise estimate of the error at discontinuities of the index profile, let us consider, as a model, an oversized dielectric slab. When the origin of the  $x$  axis is taken at one of the slab boundaries, the normalized field of  $H$ -modes of order  $m$  is (see, for example, Ref. 6 with a slight change of notation)

$$E_m(x) = \begin{cases} -\frac{1}{\sqrt{2}} \sin(Y_m X - \arcsin Y_m), & X \leq 0, \\ \frac{1}{\sqrt{2}} \exp(-\sqrt{1 - Y_m^2} X), & X \geq 0, \end{cases} \quad (11)$$

where

$$Y_m = (m + 1)(\pi/2)V^{-1} \quad (12)$$

and  $X$ ,  $V$  are normalized distances and frequencies

$$X = k\sqrt{2\Delta}x \quad (13a)$$

$$V = k\sqrt{2\Delta}d. \quad (13b)$$

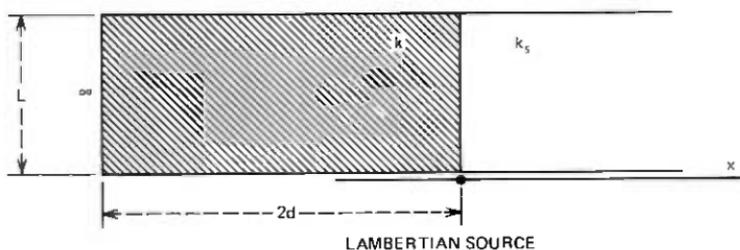
For trapped modes, we require

$$Y_m < 1. \quad (14)$$

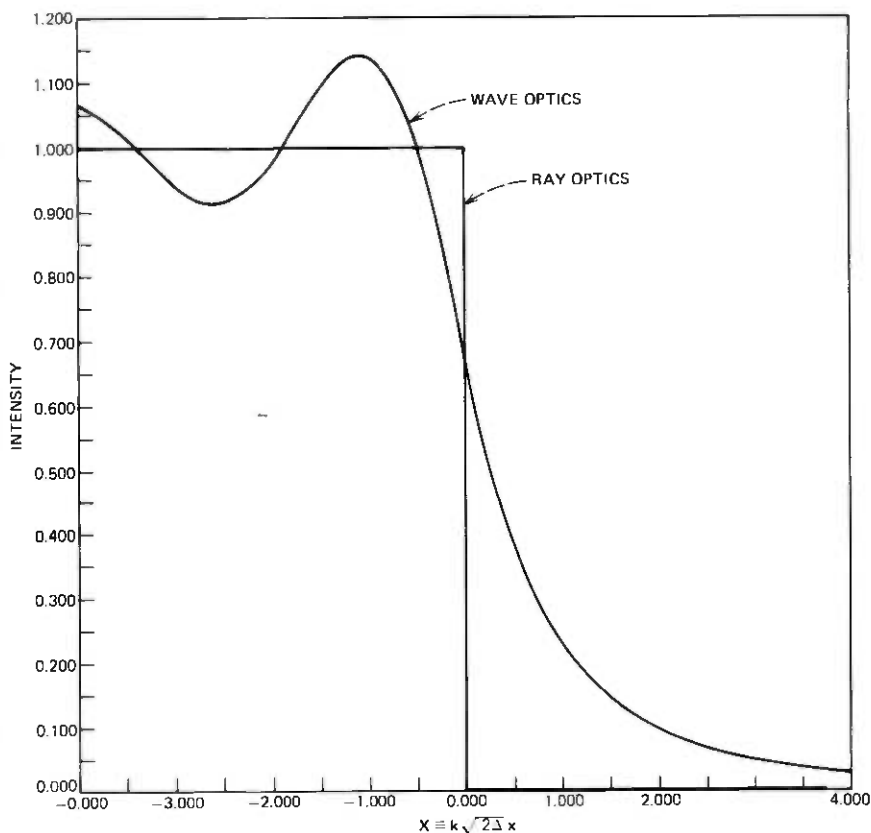
When the fiber is excited by a Lambertian source, the intensity  $I(x)$  in the slab cross section is obtained by adding the intensities,  $E_m^2(x)$ , of all the trapped modes. Because the slab is highly oversized, we can replace the summation over  $m$  by an integral. We obtain

$$I(x) = \begin{cases} 2 \int_0^{\pi/2} \sin^2(\sin \theta X - \theta) \cos \theta d\theta & X \leq 0 \\ 2 \int_0^{\pi/2} \sin^2 \theta \exp(-2 \cos \theta X) \cos \theta d\theta, & X \geq 0. \end{cases} \quad (15)$$

For  $X \rightarrow -\infty$  and  $X \rightarrow +\infty$ , we have as expected,  $I = 1$  and  $I = 0$ . At the discontinuity ( $X = 0$ ), an elementary integration of (15) gives  $I = \frac{2}{3}$ . The intensity profile defined in (15) is shown in Fig. 13. We notice an overshoot of the irradiance equal to 14 percent. This overshoot is somewhat similar to the Gibbs effect encountered with Fourier series. If we keep the slab thickness a constant but increase the optical frequency, the region where the irradiance departs significantly from the ray-optics value becomes narrower and narrower. The amplitude of the overshoot, however, remains the same. The curve in Fig. 13 provides understanding of the limitation in resolution of the method discussed in the main text. This limitation is caused by wave-optics effects that have been ignored in eq. (1).



(a)



(b)

Fig. 13—Wave-optics effect in highly multimoded slab (a). The curve in (b) exhibits the departure from ray optics. Note the overshoot of 14 percent, which is independent of wavelength.

## APPENDIX B

### Profile Distortion

In this Appendix we derive formulas relating to the change of shape of the index profile of a fiber as the wavelength varies (independently

of a possible change of scale). These formulas relate the distortions measured directly on the fiber to measurements on bulk samples.

Let us assume that we have normalized the profiles to unity at  $r = 0$ . The ordinate of the curve is  $1 - \eta$ , where  $\eta = N/2\Delta$ ,  $N(r) \equiv 1 - n^2(r)/n_o^2$  and  $2\Delta = 1 - n_c^2/n_o^2$ . From the normalized profiles at two closely spaced wavelengths, we evaluate the profile distortion  $d(r)$

$$d(r) \equiv \lambda_o \partial \eta / \partial \lambda_o. \quad (16a)$$

This may be written as

$$d = C^{-1}[\lambda_o(\partial P/\partial \lambda_o) + P(X/C)(\partial C/\partial X)], \quad (16b)$$

where  $P(r, \lambda_o)$  is the normalized (but uncorrected) fiber transmission,  $C(r, X)$  the leaky-ray correction factor, and  $X$  is the parameter defined in (9).

$C$  and the differential correction term  $(X/C)(\partial C/\partial X)$  can be obtained from Fig. 5.

Let us now consider the curve  $S(n)$  where  $S \equiv -\lambda_o n \partial n / \partial \lambda_o$  that can be obtained from measurements on bulk samples. From the value of  $\Delta$  and the cladding index  $n_o$ , we calculate the index on axis  $n_c$ . It is not difficult to show [e.g., from eq. (14) of Ref. 11] that the distortion parameter  $d$  defined in (16) is related to the dispersion parameter  $S$  defined above by

$$d(\eta) = [D_o/\Delta(n_o^2 + S_o)][s(\eta) - \eta s(1)], \quad (17)$$

where we have defined

$$D_o \equiv 1 - (\lambda_o/n_o)(\partial n_o/\partial \lambda_o), \quad (18)$$

and

$$s \equiv S(n) - S(n_o) \quad (19)$$

is considered a function of  $\eta$ . In particular,  $s(1) \equiv S(n_c) - S(n_o)$ . It is clear, from its definition and from (17), that

$$d(0) = d(1) = 0. \quad (20)$$

## REFERENCES

1. E. A. J. Marcatili, private communication.
2. J. A. Arnaud, unpublished work.
3. J. A. Arnaud and J. W. Fleming, "Pulse Broadening in Multimode Optical Fibers with Large  $\Delta n/n$  Numerical Results," *Electron. Lett.*, **12**, No. 7 (April 1976).
4. D. Gloge and E. A. J. Marcatili, "Multimode Theory of Graded Core Fibers," *B.S.T.J.*, **52** (November 1973), pp. 1563-1578.
5. F. M. E. Sladen, D. N. Payne, and M. J. Adams, "Determination of Optical Fiber Refraction Index Profiles by a Near-Field Scanning Technique," *Appl. Phys. Lett.*, **28**, No. 5 (March 1, 1975), p. 255.
6. J. A. Arnaud, *Beam and Fiber Optics*, New York: Academic Press, 1976.
7. J. Stone and H. E. Earl, "Surface Effects and Reflection Refractometry of Optical Fibers," *Opt. Quant. Elec.*, **8** (1976), pp. 459-463.
8. H. M. Presby, private communication.
9. J. B. MacChesney, private communication.
10. J. B. MacChesney and P. B. O'Connor, private communication.
11. J. A. Arnaud, "Numerical Evaluation of the Impulse Response of Multimode Optical Fibers," unpublished work.

## Wavelength Dependence of Frequency-Response Measurements In Multimode Optical Fibers

By L. G. COHEN, H. W. ASTLE, and I. P. KAMINOW

(Manuscript received May 24, 1976)

*A newly developed technique for directly measuring fiber dispersion in the frequency domain as a function of wavelength is described. Spectrally filtered white light from a xenon arc lamp is sinusoidally modulated in the range 0 to 1 GHz by an electrooptic modulator and injected into a fiber. The procedure is to vary the modulation frequency and measure the corresponding sideband output power with a photomultiplier and spectrum analyzer. Ratio measurements between the test fiber and a short reference fiber give the baseband frequency response. A number of germanium- and boron-doped fibers have been examined. The least dispersive borosilicate graded-index fiber has a 1 dB bandwidth of 1 GHz, after 1.07 km of propagation at  $\lambda = 908$  nm. The width broadens gradually with increasing wavelengths up to  $\lambda = 1100$  nm.*

### I. INTRODUCTION

Optical fiber waveguides are potentially useful for transmitting analog signals as well as digital pulses in communication systems. The information-carrying capacity of such a waveguide is determined by its impulse response in the time domain or equivalently in the frequency domain by the spectral transfer function, which is the Fourier transform of the impulse response. Most of the previous studies<sup>1</sup> of fiber dispersion have analyzed the fiber response to short laser pulses. In these studies we are limited to wavelengths for which pulsed laser sources are available. The frequency domain method described here allows accurate measurements of fiber response to be made over a wide range of wavelengths using an incoherent broadband source, such as a xenon arc lamp.

The simplicity of the method rests on the observation<sup>2</sup> that for an incoherent optical carrier the fiber response behaves quasi-linearly in power. The implication for the optical power  $p(t)$  and its transform

$P(\omega)$  is

$$P_{\text{out}}(\omega) = G(\omega) \times P_{\text{in}}(\omega) \quad (1)$$

or

$$p_{\text{out}}(t) = g(t) * p_{\text{in}}(t), \quad (2)$$

where  $G(\omega)$  is the power transfer function of the baseband frequency  $\omega$ ,  $g(t)$  is the power impulse response and  $*$  denotes convolution. This quasi-linear behavior results when fluctuations in the optical carrier frequency are sufficiently large and rapid. Thus, the phase of an incoherent optical source of width  $\Delta\lambda = 1$  nm fluctuates on average through one cycle in  $3 \times 10^{-12}$  s for  $\lambda = 1000$  nm, but the characteristic time required to observe intensity modulation of the carrier at frequencies less than 10 GHz is greater than  $10^{-10}$  seconds. Hence, the power-linearity approximation holds for most practical measurement methods utilizing sources whose spectral bandwidth ( $\Delta\lambda$ ) is greater than 1 nm. Although (1) and (2) have been derived rigorously by Personick,<sup>2</sup> we present a simple physical derivation later in this paper.

Modern multimode fibers are fabricated with smoothly graded refractive index profiles that have a maximum on the core axis and decrease gradually with an approximately power law variation until they merge into the cladding region. The optimal profile, at a particular wavelength, is the one for which the group velocity variation from ray to ray most nearly compensates for the corresponding path length variation.<sup>3</sup> Dispersive refractive index differences between material constituents ( $\text{B}_2\text{O}_3$  and  $\text{SiO}_2$  for borosilicate fibers;  $\text{GeO}_2$  and  $\text{SiO}_2$  for germanium-doped fibers) causes modal group velocities to depend not only on the index profile but also on the wavelength (profile dispersion). Consequently, the exponential parameter,  $\alpha$ , which characterizes the optimal profile, may deviate from  $\alpha = 2$  and is wavelength dependent.<sup>4-6</sup> Recent experimental investigations have shown that graded-index fibers can reduce intermodal dispersion by almost two orders of magnitude from what it would be in a step ungraded-index multimode fiber.<sup>7</sup>

This paper describes a newly developed technique for directly measuring fiber baseband frequency response in spectrally filtered incoherent light. The spectral test set is particularly suitable for wavelength-dependent studies over a wide range of wavelengths without resorting to a multitude of monochromatic mode-locked laser sources. Instead of injecting pulses to measure a fiber's impulse response, we inject an incoherent cw optical carrier that is intensity-modulated by a frequency-tunable sinusoidal signal. Then, we compare the intensities of the sine wave envelopes at the input and output ends of the fiber. Sideband power is detected by a photomultiplier and displayed on a spectrum analyzer. The receiver dynamic range is sufficient to

measure transmission through kilometer-long fibers with an accuracy of  $\pm 10$  percent over an electrical bandwidth of dc to 1 GHz and is equivalent to measuring  $2\sigma \approx 0.1$  ns full rms impulse response widths. Measurement precision is better in the frequency domain than the time domain, because the deconvolution process, for removing signal distortion caused by the limited detector bandwidth, is simply an arithmetic division of output by input frequency response rather than a cumbersome deconvolution integral of pulse shapes. One shortcoming of the present technique is that we do not measure the input to output phase change of the sinusoidal modulation and therefore cannot construct the impulse response directly from the power frequency response data. However, approximate mathematical methods are available for determining the phase from the magnitude of a transfer function. Measurement of the phase change may also be feasible. Nevertheless, unless the phase distortion is extreme, the information capacity of the fiber will be indicated by the magnitude of the transfer function.

Previous dispersion measurements in the frequency domain were made by comparing the best spectra of longitudinal modes from a free-running laser before and after transmission through a fiber<sup>8</sup>, by externally modulating a laser<sup>9</sup> or by directly modulating a light-emitting diode (LED).<sup>10</sup> One disadvantage of the technique described in Ref. 8 is that the fiber frequency response can only be measured at discrete frequencies corresponding to integral multiples of the longitudinal mode spacing of the laser (100-MHz increments for a 1.5-m cavity length). The other techniques were used to make frequency response measurements only at one wavelength from dc to several hundred MHz and had less dynamic range than our system. Personick et al. used wide bandwidth LED light ( $\Delta\lambda \approx 40$  nm at  $\lambda = 900$  nm) to measure primarily material dispersion effects in a 1-km fiber.<sup>10</sup> Our technique uses narrow spectral width incoherent light to measure primarily intermodal dispersion effects in kilometer-long fibers.

### 1.1 Technique and apparatus

The measuring apparatus is illustrated in Fig. 1. The xenon arc lamp output passes through one of a set of narrowband interference filters and is focused into a LiTaO<sub>3</sub> electrooptic intensity modulator. The modulated beam is then refocused into either the fiber under test or a short length (2 m) of reference fiber. The fiber output is then detected by a sensitive broadband photomultiplier and the baseband modulation components are displayed by a spectrum analyzer. The component at modulating frequency  $\omega$  from the reference fiber is taken as  $P_{in}(\omega)$  and the component from the test fiber as  $P_{out}(\omega)$ .

The LiTaO<sub>3</sub> modulator was designed<sup>11</sup> for use with a 1.06- $\mu$ m laser

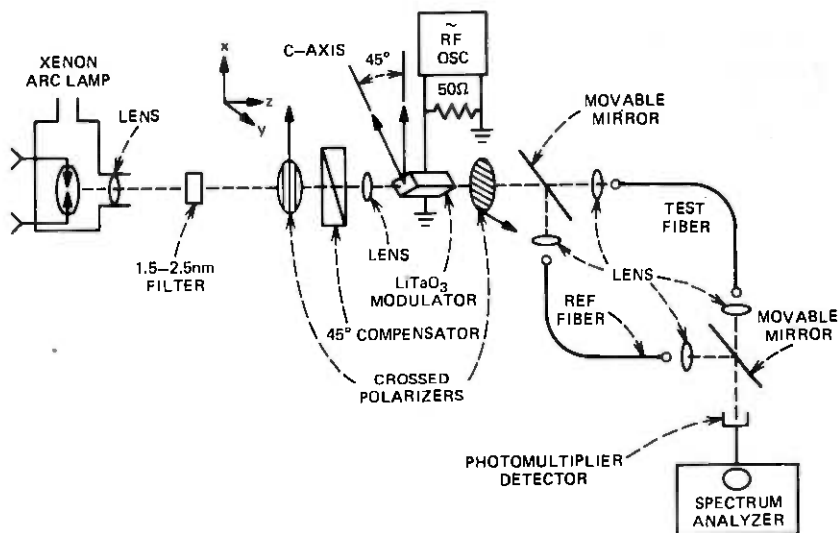


Fig. 1—Experimental arrangement for making spectral dispersion measurements in the frequency domain.

and has too small an aperture-to-length ratio to pass the focused incoherent beam completely. Nevertheless, it has proved adequate for these early measurements, while a more-suitable modulator was being built. The  $\text{LiTaO}_3$  rod is 0.25 mm by 0.25 mm by 10 mm and its low-capacity coaxial housing allows for modulation frequencies above 1 GHz. Typically, 3 W of drive power from the rf sine wave generator is needed to provide 40-percent modulation. An Ehringhaus compensator biases the modulator in its linear region at the operating wavelength. The intensity transmitted by the  $\text{LiTaO}_3$  crystal and compensator placed between crossed polarizers is proportional to  $\sin^2 \Gamma/2$ , where  $\Gamma$  is the phase retardation of crystal and compensator, consisting of a dc bias plus time-dependent term. Dispersion of the optical bias over the spectral width  $\Delta\lambda$  of the input filter is an important consideration in system performance. For  $\text{LiTaO}_3$  at  $\lambda = 800$  nm,

$$d\Gamma_{dc}/d\lambda = \frac{2\pi L}{\lambda} (dB/d\lambda - B/\lambda) \approx -1.9 \times 10^{-2} \pi L, \quad (3)$$

where  $\Gamma_{dc}$  is the phase retardation bias,  $\lambda$  is the wavelength in nm,  $L$  is the modulator length in mm, and  $B$  is the difference between extraordinary and ordinary refractive indices. For  $L = 10$  mm and  $\Delta\lambda = 1.5$  nm, the bias point is smeared by as much as  $0.29\pi$  radians (neglecting the smaller effect of opposite sign due to the compensator). Thus, wavelengths at the spectral band edges will have somewhat

different modulation indices and phases compared with the band center. It was found that bias ranges  $\Delta\Gamma_{dc}$  corresponding to  $\Delta\lambda > 10$  nm could give erroneous results, for example,  $P(\omega)/P(0) > 1$ .

Observed fiber output power levels are on the order of 1 nanowatt. The Varian VPW-154/2 static crossed-field photomultiplier tube\* is particularly suitable for our broadband low light level application. Due to the crossed electric and magnetic fields formed by applied voltages and integral magnets, detected photoelectrons travel a cycloidal path and are multiplied by six dynodes before being collected at the anode. These short tightly focused electron paths result in the high 0 to 2.5-GHz detection bandwidth necessary for our measurements. The tube has an InGaAsP photocathode sensitive to far infrared wavelengths up to 1100 nm and its six dynode stages provide  $3 \times 10^5$  gain. The resultant anode sensitivities yield high signal-to-noise ratios with 10-KHz spectrum-analyzer bandwidths. Additional problems of rf interference from the high-power rf oscillator picked up on the spectrum analyzer were eliminated by carefully shielding the modulator circuitry and the photomultiplier housing.

## 1.2 Frequency domain measurements

Input-to-output power-transfer functions have been measured from dc to 1 GHz in a variety of germanium and boron-doped kilometer-length fibers. Wavelength-dependent measurements were made by filtering the white arc lamp light through a series of interference filters whose center wavelengths ranged from  $\lambda = 650$  nm to  $\lambda = 1100$  nm. To reduce modulator errors and material dispersion effects,<sup>12</sup> the filter bandwidths were less than: 1.5 nm for  $650 \text{ nm} < \lambda < 908$  nm, 2.4 nm for  $920 \text{ nm} < \lambda < 980$  nm, and 10 nm for  $1040 \text{ nm} < \lambda < 1100$  nm.

The least-dispersive test fiber was a graded borosilicate fiber with  $\alpha \sim 1.8$ , which had a 1-dB bandwidth of 1 GHz after 1.07 km of propagation at  $\lambda = 908$  nm. Figure 2a illustrates its sideband output power normalized to dc,  $P(f)/P(0)$ , plotted versus modulating frequency for six wavelengths in the range  $650 \text{ nm} < \lambda < 1100$  nm. The frequency bandwidth increases with increasing wavelength. This trend is clearer in Fig. 3a, which shows relative sideband power plotted versus 14 wavelengths for a fixed modulation frequency,  $f = 990$  MHz. The 25-percent increase in bandwidth in the range  $650 \text{ nm} < \lambda < 1100$  nm is partially due to material dispersion effects, which decrease as the wavelength increases. Material dispersion should cause a 1-dB amplitude roll-off after 1 GHz for 1.5-nm source spectral

\* Varian/LSE Division, Palo Alto, California.

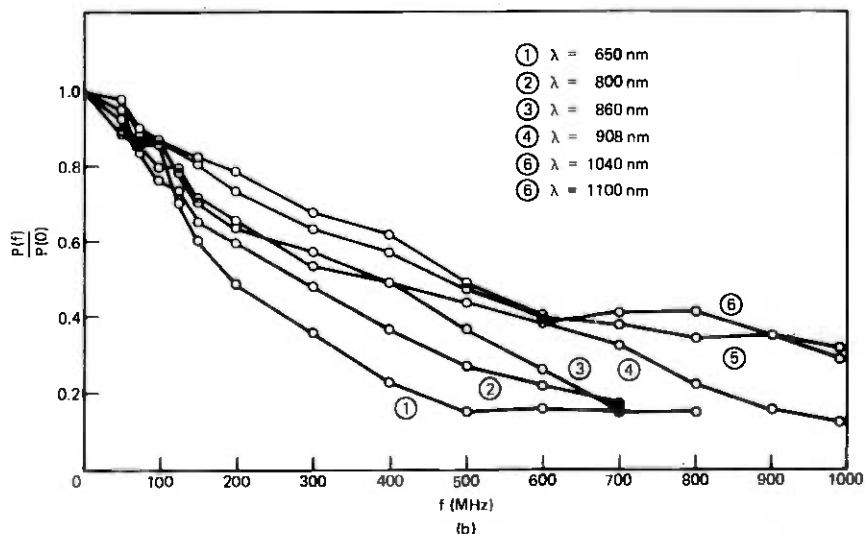
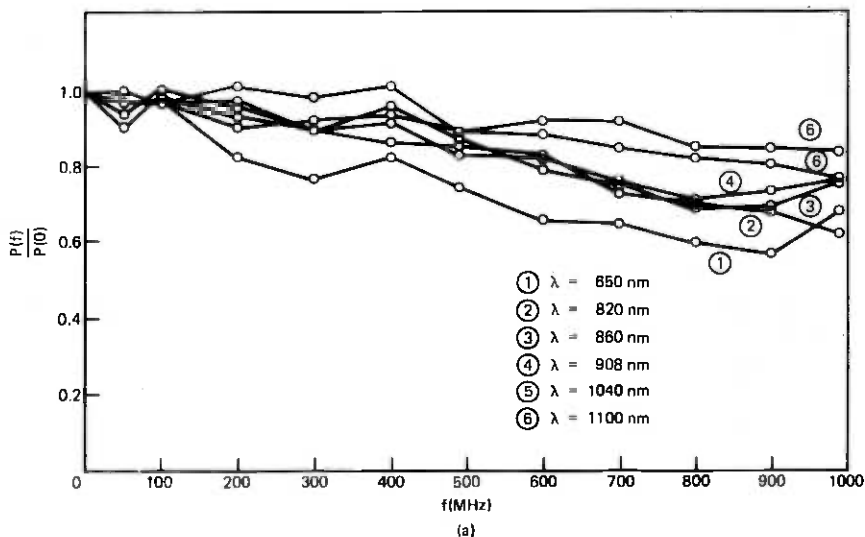


Fig. 2—Power transfer function amplitude vs. modulation frequency with optical wavelength as parameter. (a) Boron-doped graded-core fiber. (b) Germanium-doped graded-core fiber.

bandwidths centered about wavelengths between  $650 \text{ nm} < \lambda < 750 \text{ nm}$ . If the sideband amplitudes were increased by 1 dB between  $650 \text{ nm} < \lambda < 750 \text{ nm}$  to compensate for material dispersion, then the resultant data points in Fig. 3a would be independent of wavelength for  $650 \text{ nm} < \lambda < 1100 \text{ nm}$ .

Figure 2b illustrates power transfer functions for a graded germanium-doped fiber with  $\alpha \sim 1.9$ , which does not have a near-optimal profile for minimum modal dispersion. As a result, it has a relatively narrow 1-dB bandwidth of 150 MHz after 0.9 km of propagation at a wavelength of 908 nm. Material dispersion effects should be negligibly small here because amplitude roll-offs are much faster than in Figs. 2a and 3a. Hence, profile dispersion is responsible for the wavelength dependence of the bandwidth broadening in this fiber. The wavelength-dependent broadening is much greater for this germanium-doped fiber than for the previously described boron-doped fiber. Figure 3b shows relative sideband power plotted versus 14 wavelengths for a fixed modulation frequency,  $f = 100$  kHz. The bandwidth more than doubles for  $650 \text{ nm} < \lambda < 1100 \text{ nm}$ . Comparison of curves a and b in Fig. 3 suggests that wavelength variation of profile dispersion is significantly greater in germanium-doped fibers than in boron-doped fibers. This observation is qualitatively consistent with recent refractive index profile measurements by interference microscopy on thin polished fiber samples.<sup>13</sup>

### 1.3 Equivalence of impulse and frequency domain measurements

We can prove (1) and (2) neglecting material dispersion for the simple case of a multimode fiber transmitting an incoherent optical beam without mode mixing as follows. Although a general proof is given by Personick,<sup>2</sup> the following proof is more relevant to our

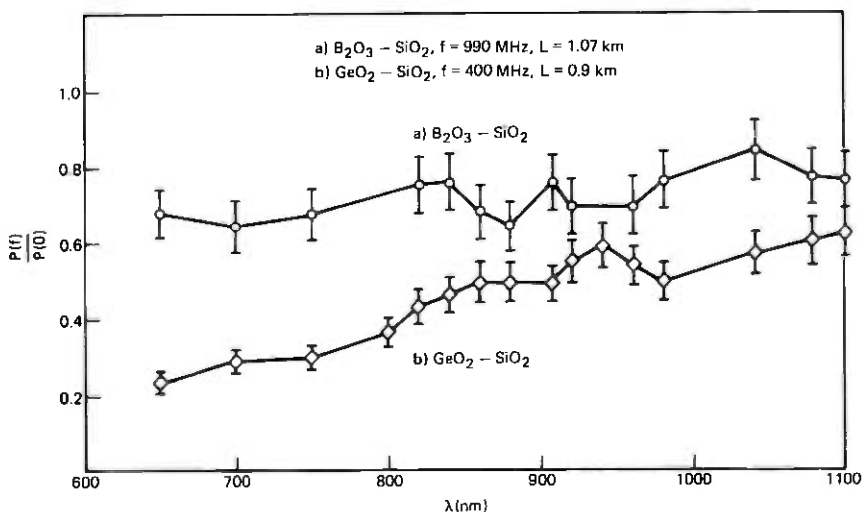


Fig. 3—Power transfer function amplitude vs. optical wavelength with modulation frequency as parameter. (a) Boron-doped graded-core fiber. (b) Germanium-doped graded-core fiber.

measurement technique. Assume an input amplitude pulse defined by

$$e_{in}(t) = v(t)e^{i\omega_o t}, \quad (4)$$

and corresponding power pulse defined by

$$p_{in}(t) = |v(t)|^2, \quad (5)$$

where  $\omega_o(t)$  is the fluctuating frequency of the incoherent optical carrier and  $v(t)$  is the envelope of a short pulse with peak at  $t = 0$ . If the input pulse excites  $N$  modes of the fiber such that the fractional power in the  $\nu$ -th mode is  $|c_\nu|^2$ , then the output is

$$e_{out}(t) = \sum_{\nu=1}^N c_\nu v(t - \tau_\nu) e^{i\omega_o(t - \tau_\nu)} \quad (6)$$

$$p_{out}(t) = \sum_{\nu=1}^N \sum_{\mu=1}^N c_\nu c_\mu^* v(t - \tau_\nu) v^*(t - \tau_\mu) e^{i\omega_o(\tau_\mu - \tau_\nu)}, \quad (7)$$

where  $\tau_\nu$  is the delay for  $\nu$ -th mode and

$$\sum_{\nu=1}^N |c_\nu|^2 = 1. \quad (8)$$

Now  $p_{out}(t)$  is measured by a detector with response time  $T_1$  that is usually comparable with the output pulse width, say  $T_2 > 10^{-10}$  s. The incoherent optical carrier at  $\lambda \approx 10^3$  nm with  $\Delta\lambda \sim 1$  nm has a frequency bandwidth  $\Delta\omega_o = 2\pi c\Delta\lambda/\lambda^2 \approx 2\pi \times 3 \times 10^{11}$  Hz that can be regarded as arising from a random frequency modulation of the carrier with modulation frequency  $\omega_m$  and deviation frequency  $\omega_d$  both roughly equal to  $\Delta\omega_o$ . But,  $d\omega_o/dt = \omega_m\omega_d \approx (\Delta\omega_o)^2$  for an FM signal. Then, the phase factor  $\omega_o(\tau_\mu - \tau_\nu)$  will fluctuate through a phase range  $\Delta\phi$  of at least

$$\Delta\phi = (d\omega_o/dt)(\tau_\mu - \tau_\nu)T_1 \approx (\Delta\omega_o)^2(\tau_\mu - \tau_\nu)T_1 \\ \approx (\Delta\omega_o)^2 T_1 T_2 / N \text{ radians} \quad (9)$$

during the characteristic measuring time  $T_1$  for an  $N$ -mode fiber. If  $(\tau_\mu - \tau_\nu)$  is the minimum delay difference between adjacent, equispaced modes, then  $T$  need not be smaller than  $N(\tau_\mu - \tau_\nu)$ , a lower bound on the output pulse width as assumed in (9). Thus, we find  $\Delta\phi > 100\pi$  for  $N = 100$  and  $T_1 = T_2 > 10^{-10}$  s, so that all terms in (7) for  $\nu \neq \mu$  vanish on averaging over  $T$ . In the present experiment,  $T = 10^{-4}$  s as determined by the spectrum analyzer bandwidth so that  $\Delta\phi \gg 100\pi$ . Spatial incoherence of the input beam further reduces the crossterms in (7).

The observed power is then

$$p_{\text{out}}(t) = \sum_{\nu=1}^N |c_{\nu}|^2 |v(t - \tau_{\nu})|^2, \quad (10)$$

and if we let  $|v(t)|^2$  be the unit impulse  $u_0(t)$ , we have the impulse response

$$g(t) = \sum_{\nu=1}^N |c_{\nu}|^2 u_0(t - \tau_{\nu}). \quad (11)$$

The Fourier transform of the impulse response yields

$$\begin{aligned} G(\omega) &= \int_{-\infty}^{\infty} g(t) e^{-i\omega t} dt \\ &= \sum_{\nu=1}^N |c_{\nu}|^2 e^{-i\omega \tau_{\nu}}, \end{aligned} \quad (12)$$

where  $\omega$  is the frequency of the envelope of the modulated carrier and  $G(\omega)$  is the complex power transfer function.

Next, consider a sinusoidally intensity-modulated incoherent carrier incident on the fiber. This is the experimental method used here. We wish to show it to be equivalent to the impulse response method. For sufficiently small modulation index  $m$ , the electrooptically modulated input to the fiber is

$$e_{\text{in}}(t) = (1 + m \cos \omega t)^{\frac{1}{2}} e^{i\omega_0 t} \quad (13)$$

$$p_{\text{in}}(t) = (1 + m \cos \omega t). \quad (14)$$

Since we employ a spectrum analyzer in the measurements, we are concerned only with the term at the fundamental frequency  $\omega$  in (14). As before, the input excites  $N$  modes of the fiber and the output is

$$e_{\text{out}}(t) = \sum_{\nu=1}^N c_{\nu} e^{i\omega_0(t-\tau_{\nu})} [1 + m \cos \omega(t - \tau_{\nu})]^{\frac{1}{2}} \quad (15)$$

$$\begin{aligned} p_{\text{out}}(t) &= \sum_{\mu=1}^N \sum_{\nu=1}^N c_{\nu} c_{\mu}^* e^{i\omega_0(\tau_{\mu}-\tau_{\nu})} \\ &\quad \times [1 + m \cos \omega(t - \tau_{\nu})]^{\frac{1}{2}} [1 + m \cos \omega(t - \tau_{\mu})]^{\frac{1}{2}}. \end{aligned} \quad (16)$$

But we can use our earlier argument for the random carrier to eliminate all terms for  $\nu \neq \mu$  in (16). If we retain only the term at the fundamental frequency, we obtain the observed power

$$p_{\text{out}}(t) = m \sum_{\nu=1}^N |c_{\nu}|^2 \cos \omega(t - \tau_{\nu}) = \text{Re} \left\{ m \sum_{\nu=1}^N |c_{\nu}|^2 e^{-i\omega \tau_{\nu}} e^{i\omega t} \right\}. \quad (17)$$

Then, with  $\tau_\nu = 0$  for  $p_{in}(t)$ ,

$$\frac{P_{out}(\omega)}{P_{in}(\omega)} = G(\omega) = \sum_{\nu=1}^N |c_\nu|^2 e^{-i\omega\tau_\nu} \quad (18)$$

as in (12), which completes the proof of equivalence for no mode mixing. With mode mixing,  $\tau_\nu$  becomes a continuum,<sup>2</sup> and we must simply replace the sum in (12) and (18) by an integral over the range of  $\tau$ , i.e.,

$$G(\omega) = e^{-i\omega\tau_0} \int_{-T_a}^{T_b} |c(\tau')|^2 e^{-i\omega\tau'} d\tau' = |G(\omega)| e^{-i\omega\tau_0} e^{i\theta}, \quad (19)$$

where

$$\tau = \tau_0 + \tau', \quad (20)$$

and  $\tau_0$  is the (large) average delay,  $\tau'$  is the deviation from  $\tau_0$ , and  $-T_a < \tau' < T_b$  is the range of allowed modal delay. In a similar way for (18), we can let

$$\tau_\nu = \tau_0 + \tau'_\nu. \quad (21)$$

At present our measurements yield only  $|G(\omega)|$ . The phase angle  $\theta(\omega)$  is required to obtain the impulse response  $g(t)$  from

$$g(t) = \frac{1}{2\pi} \int_{-\infty}^{\infty} G(\omega) e^{i\omega t} d\omega. \quad (22)$$

Direct measurement of  $\theta(\omega)$  is difficult because a 1-km long fiber contains many modulation wavelengths. However, if we assume that the fiber behaves like a minimum phase network, i.e.,  $G(j\omega)$  has no zeros in the right half of the complex plane, then we can calculate  $\theta(\omega)$  from  $|G(\omega)|$ . The average delay factor  $e^{-i\omega\tau_0}$  is not a minimum phase function.<sup>14</sup> However,  $G(\omega)e^{i\omega\tau_0}$  in (18) and (19) appears to exhibit approximate minimum phase behavior in some, but not all cases. In the next section we illustrate the approximate minimum phase behavior as obtained from a comparison of the  $g(t)$  calculated from  $|G(\omega)|$  with the measured  $g(t)$  for a particular fiber. A later publication will treat the minimum phase approximation in more detail.

On the other hand, the measured  $g(t)$  is real so that  $G(\omega)$  may be obtained directly from pulse measurements using (12) without any assumptions as we also show below.

#### 1.4 Correlation with time domain measurements

The impulse response  $g(t)$  was measured by injecting narrow impulses ( $2\sigma = 0.4$  ns) from a GaAs laser and observing the broadened output. Time domain measurements were fast-Fourier-transformed to produce the solid curves shown in Fig. 4a and b for the boron and germanium-doped fibers described in Figs. 2 and 3. Time domain data

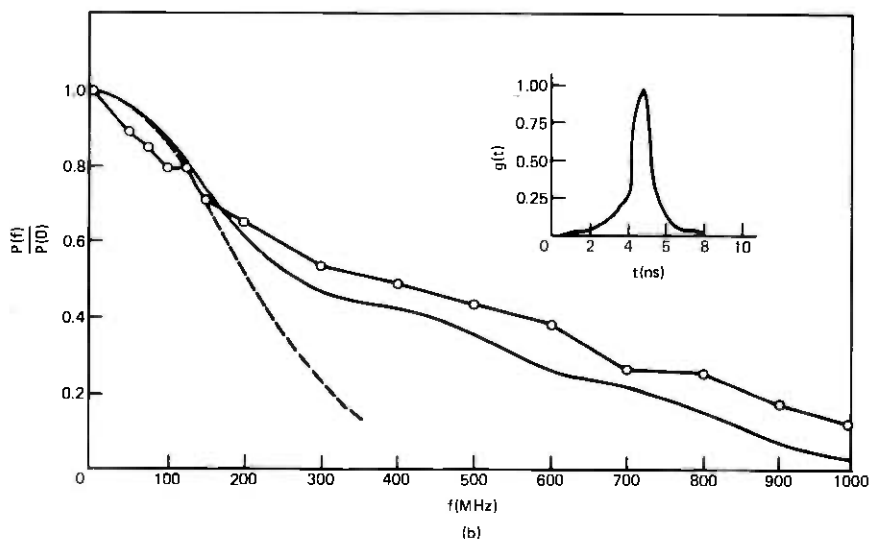
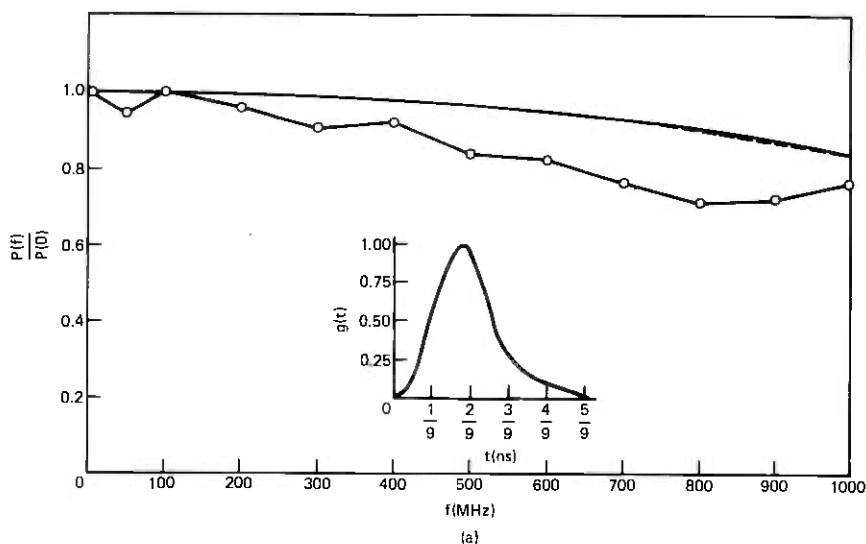


Fig. 4—Frequency domain measurements (0 data points) are compared with fast-Fourier transformed impulse response measurements [ $g(t)$  vs.  $t$ ] at  $\lambda = 908$  nm,  $\Delta\lambda \approx 1.4$  nm. The dashed curves are gaussian fits to the solid curves (computed transforms). (a) Boron-doped graded-core fiber,  $2\sigma = 0.19$  ns/1.07 km. (b) Germanium-doped graded-core fiber,  $2\sigma = 1.8$  ns/0.9 km.

for the low dispersion borosilicate fiber (inset Fig. 4) was deduced from shuttle pulse measurements after nine trips through the fiber. Fourier-transformed time domain results are compared in Fig. 4 with directly measured frequency domain data points measured in incoherent light

at the same wavelength,  $\lambda = 908$  nm. The qualitative agreement is quite good and the quantitative agreement is generally within 20 percent. Dashed curves in Fig. 4a and b show gaussian approximations to the computed solid curves given by

$$|G(\omega)| \approx e^{[-(\omega\sigma)^2/2]}, \quad (23)$$

where  $2\sigma$  is the full rms pulse width of the measured impulse responses,  $g(t)$ , illustrated in the insets of Fig. 4a and b ( $2\sigma \approx 0.19$  ns/1.07 km for the boron-doped fiber *a*;  $2\sigma \approx 1.8$  ns/0.9 km for the germanium-doped fiber *b*). Thus, the gaussian fit to  $|G(\omega)|$  can give an estimate of the pulse width  $2\sigma$  without knowledge of  $\theta(\omega)$ .

In both cases *a* and *b*, the gaussian approximations to  $|G|$  are accurate down to the 0.75-amplitude point in the frequency domain. The approximation does not fit the germanium fiber *b* data, when  $|G(\omega)| < 0.75$ , because its impulse response is asymmetric with a long leading edge.

The usefulness of the minimum phase approximation, for inverting frequency domain amplitude spectra back into the time domain, was tested on data in Figs. 2b and 4b for a germanium-doped fiber. A Hilbert transform was used to compute the minimum phase function,  $\theta(f)$ , from the  $\ln |G(\omega)| = -\eta(\omega)$ ,<sup>14</sup>

$$\theta(f) = -\frac{f}{\pi} \int_{-\infty}^{\infty} \frac{\eta(f_0)}{f_0^2 - f^2} df_0. \quad (24)$$

Hilbert transforms are particularly easy to evaluate when the given function,  $\eta(f)$ , is a piecewise-linear function consisting of a series of  $M$  straight-line segments. In that case its second derivative consists of a sum of impulses and the integral formulation of (24) can be replaced by a summation.<sup>14</sup>

$$\theta(f_m) = -\frac{1}{\pi} \sum_{K=1}^M B(K) [(f_m - f_K) \ln |f_m - f_K| + (f_m + f_K) \ln |f_m + f_K|], \quad (25)$$

where

$$B(K) = A(K+1) - A(K)$$

$$A(K) = \frac{\eta(f_{K+1}) - \eta(f_K)}{f_{K+1} - f_K}.$$

Figure 5a uses the data in Fig. 4b to compare: curve 1, the measured impulse response shown in Fig. 4b, with detector distortion deconvolved ( $2\sigma = 1.81$  ns), and curve 2, the time pulse obtained by taking the Fourier transform of 1 and using its amplitude spectrum and assumed minimum phase to compute the impulse response ( $2\sigma = 1.77$  ns). Curve 3 shows the time pulse calculated from frequency measurements in Fig. 4b and the corresponding piecewise linear minimum phase function ( $2\sigma = 1.89$  ns). The rms pulsewidths and qualitative

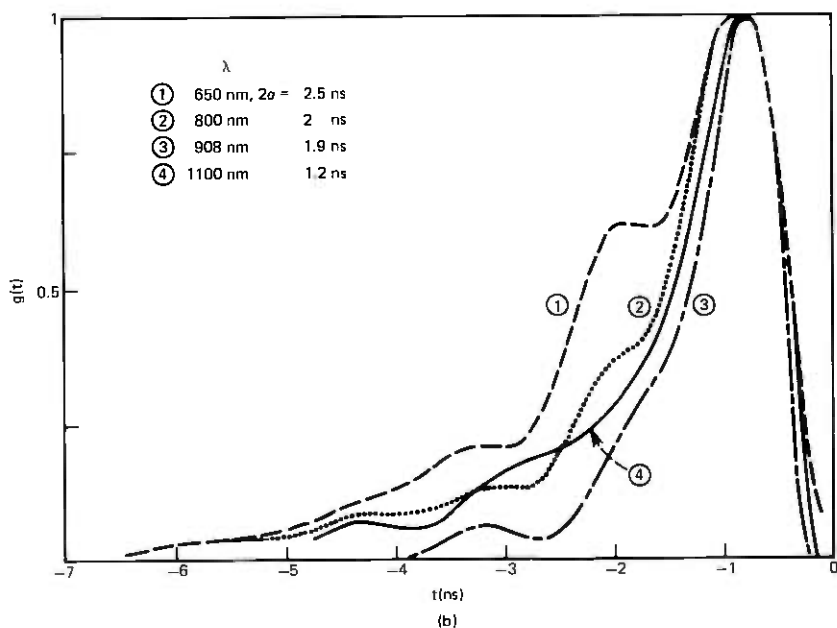
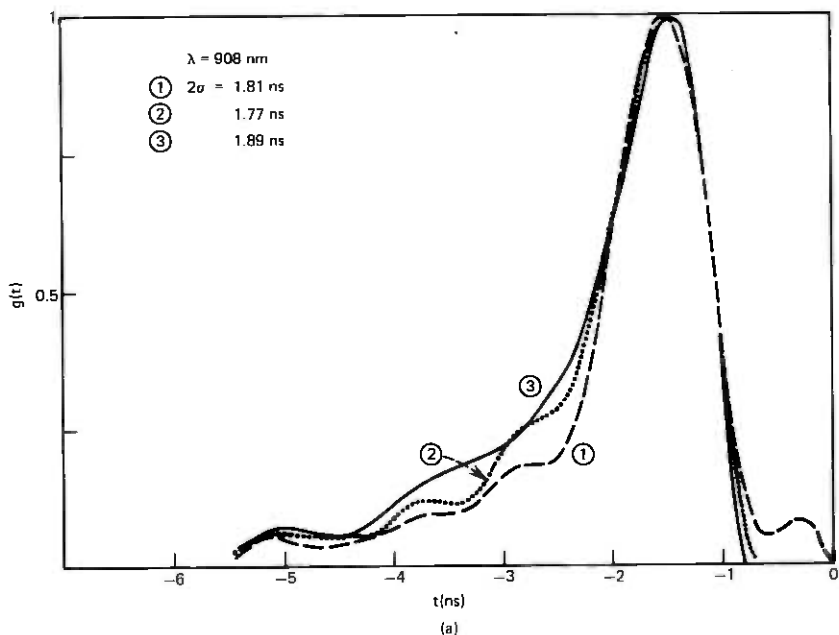


Fig. 5—Time domain impulse responses computed from amplitude spectra in the frequency domain. (a) A measured impulse response at  $\lambda = 908$  nm (1) is compared with (2) its minimum phase response, and (3) the response using frequency domain measurements in Fig. 4b and minimum phase function assumption. (b) Wavelength-dependent time pulses computed from frequency domain measurements in Fig. 2b.

structure of the three pulses in Fig. 5a agree very well, which implies that the minimum phase function can be used to construct a good facsimile of the actual impulse response.

Minimum phase functions were also calculated for data in Fig. 2b and used to construct the wavelength-dependent impulse response shapes in Fig. 5b. The results show that the impulse response becomes wider and more asymmetric when the signal wavelength is reduced from  $\lambda = 1100$  nm ( $2\sigma = 1.2$  ns) to  $\lambda = 650$  nm ( $2\sigma = 2.5$  ns).

## II. CONCLUSIONS

The baseband frequency response of kilometer-long graded index fibers have been directly measured over a 0 to 1 GHz frequency range for wavelengths extending from the visible ( $\lambda = 650$  nm) into the infrared ( $\lambda = 1100$  nm). The accuracy of individual sideband measurements is approximately 10 percent, which is equivalent to a time resolution of  $2\sigma = 0.15$  ns (assuming a gaussian frequency roll-off function  $e^{[-(\omega\sigma)^2/2]}$  at  $f = 1$  GHz). By contrast, full rms pulse width measurements in the time domain would require a precision of  $\sqrt{(0.15)^2 + (2\sigma_i)^2} - 2\sigma_i \approx 0.02$  ns to achieve the same resolution from measurements deconvolved from detector-limited input pulse widths with  $2\sigma_i \approx 0.4$  ns.

The major advantage of the spectral technique described here is its convenience for making wavelength-dependent measurements with a tunable source of incoherent light.

The least-dispersive-measured fiber, with  $NA \approx 0.14$  and graded borosilicate core, had an 80-percent transmission bandwidth,  $F$  (1 dB)  $\approx 1$  GHz/1.07 km ( $\lambda = 908$  nm,  $\Delta\lambda \approx 1.4$  nm), which is approximately equivalent to a full rms pulse width  $2\sigma = 0.2$  ns/km. The fiber bandwidth broadened by about 25 percent over the wavelength range  $650$  nm  $< \lambda < 1100$  nm. However, a significant fraction of that increase between  $650$  nm  $< \lambda < 820$  nm can be attributed to material dispersion effects, which are insignificant for  $\lambda > 820$  nm. For comparison, a germanium-doped fiber with  $NA \approx 0.2$  had a bandwidth  $F$  (1 dB)  $\approx 0.15$  GHz/0.9 km ( $\lambda = 908$  nm,  $\Delta\lambda \approx 1.4$  nm), which is approximately equivalent to a full rms pulse width  $2\sigma = 2$  ns/km. Fiber bandwidth broadened by about 250 percent due to profile dispersion over the wavelength range  $650$  nm  $< \lambda < 1100$  nm. Less than 5 percent of this wavelength dependence can be attributed to material dispersion caused by the 1.5 nm spectral bandwidths of the filtered incoherent signal light. The fact that germanium-doped fibers exhibit much more profile dispersion than boron-doped fibers is in good agreement with interference microscopy measurements on thin fiber samples.<sup>13</sup>

The rms pulse width  $2\sigma$  can be estimated from the transfer function amplitude  $|G(\omega)|$  by assuming a gaussian distribution (23). In some cases, the shape of the pulse can be obtained by assuming a minimum phase transfer function. This latter method was used to compute wavelength-dependent time pulses from frequency response measurements in the germanium-doped fiber described. Profile dispersion made impulse response shapes wider and more asymmetric when the signal wavelength was reduced from  $\lambda = 1100$  nm ( $2\sigma = 1.2$  ns) to  $\lambda = 650$  nm ( $2\sigma = 2.5$  ns).

### III. ACKNOWLEDGMENTS

We are grateful to F. S. Chen for providing the LiTaO<sub>3</sub> modulator and to D. Enck and R. Klein (Varian/LSE Division) for their help with the crossed-field photomultiplier detector. We also thank W. Mammel for her help in computing the FFT and minimum phase functions, W. G. French, J. B. MacChesney, P. B. O'Connor, and G. W. Tasker for providing the fibers, and S. D. Personick for useful discussions of the theory.

### REFERENCES

1. L. G. Cohen, "Shuttle Pulse Measurements of Pulse Spreading in an Optical Fiber," *Appl. Opt.*, *14* (June 1975), pp. 1351-1356.
2. S. D. Personick, "Baseband Linearity and Equalization in Fiber Optic Digital Communication Systems," *B.S.T.J.*, *52* (September 1973), pp. 1175-1194.
3. D. Gloge and E. A. J. Marcatili, "Multimode Theory of Graded-Core Fibers," *B.S.T.J.*, *52* (November 1973), pp. 1563-1577.
4. R. Olshansky and D. B. Keck, "Pulse Broadening in Graded-Index Optical Fibers," *Appl. Opt.*, *15* (February 1976), p. 491.
5. D. Gloge, I. P. Kaminow, and H. M. Presby, "Profile Dispersion in Multimode Fibers—Measurement and Analysis," *Electron. Lett.*, *11* (September 1975), pp. 469-470.
6. J. W. Fleming, "Measurements of Dispersion in GeO<sub>2</sub>-B<sub>2</sub>O<sub>3</sub>-SiO<sub>2</sub> Glasses," Fall Meeting of the Amer. Ceram. Soc., Pocono Manor, October 1975.
7. L. G. Cohen, "Pulse Transmission Measurements for Determining Near Optimal Profile Gradings in Multimode Borosilicate Optical Fibers," *Appl. Opt.*, *15* (July 1976), pp. 1808-1814.
8. D. Gloge, E. L. Chinnock, and D. H. Ring, "Direct Measurement of the (Baseband) Frequency Response of Multimode Fibers," *Appl. Opt.*, *11* (July 1972), pp. 1534-1538.
9. R. Auffret, C. Boisrobert, and A. Cozannet, "Wobulation Technique Applied to Optical Fibre Transfer Function Measurement," First European Conference on Optical Fibre Communication, IEE, London, England (September 16-18, 1975), pp. 60-63.
10. S. D. Personick, W. M. Hubbard, and W. S. Holden, "Measurements of the Baseband Frequency Response of a 1-Km Fiber," *Appl. Opt.*, *13* (February 1974), pp. 266-268.
11. F. S. Chen, "Modulators for Optical Communications," *Proc. IEEE*, *58* (October 1970), pp. 1440-1457.
12. D. Gloge and E. L. Chinnock, "Fiber-Dispersion Measurements Using a Mode-Locked Krypton Laser," *IEEE J. Quantum Electron.*, *QE-8* (November 1972), pp. 852-854.
13. H. M. Presby and I. P. Kaminow, "Refractive Index and Profile Dispersion Measurements in Binary Silica Optical Fibers," *Appl. Opt.*, February 1977.
14. E. A. Guillemin, *Theory of Linear Physical Systems*, New York: John Wiley (1963), pp. 252, 275, and 536.



## Geometrical Uniformity of Plastic Coatings on Optical Fibers

By H. M. PRESBY

(Manuscript received May 14, 1976)

*The concentricity and uniformity of nearly concentric transparent plastic coatings extruded onto optical fibers are determined by a sensitive, nondestructive optical technique. The method is based on the location of unique fringes in the backscattered light arising from a beam that is incident at right angles to the fiber's axis. Results from both uniform and distorted coatings are shown, and instrumentation suitable for on-line coating diagnosis and correction is presented.*

### I. INTRODUCTION

The use of plastic coatings in optical-fiber technology is multifaceted. The refractive index of many polymer materials is less than that of fused silica, enabling them to be used directly as the cladding for fused silica cores.<sup>1-3</sup> The resulting waveguides, suitable for many communication applications,<sup>4,5</sup> are relatively easy to fabricate, possess low loss and large numerical aperture, and are LED-compatible.

Plastic coatings are also applied as an overcoat to glass-clad optical fibers. They reduce microbending loss,<sup>6,7</sup> maintain the pristine strength of the fibers,<sup>8</sup> and provide for abrasion and mechanical protection of the fibers during cable-manufacturing processes. In yet other applications, coatings have been proposed as a method of decreasing crosstalk between optical fibers<sup>9</sup> and as a way of improving the long-term stability of fibers in uncontrolled environments.

To be most effective in all of the above applications, the coating must be applied uniformly and concentrically around the fiber. This is a necessity for routine handling and splicing as well as for optimum strength and transmission characteristics.

The coatings are applied by various methods, and techniques have been proposed and implemented with varying degrees of success to aid in their concentric application. In general, micropositioning and microscopic observations are necessary to align the fiber at the start of each application<sup>5</sup> and only by preparing and microscopically

examining sections of the fiber after the run can the quality of the coating be assessed. In addition to being time consuming and destructive, microscopic examination may not detect certain problems, such as geometrical nonuniformities that can seriously impair the transmission characteristics of the fiber. More importantly, real-time information to enable the fabricator to make corrections, evaluate various applicators or stop the process completely, is not available as the coating is being applied.

We present here a sensitive new method for analyzing transparent coatings on optical fibers. The technique is optical in nature being based on the location of unique fringes in the backscattered light<sup>10</sup> arising from a beam that is incident at right angles to the fiber axis. As such, it is inherently nondestructive and noncontacting. Most importantly, it is capable of providing in-line information on coating concentricity and uniformity as the coating is being applied.

## II. MEASUREMENT THEORY

Consider the two rays of light, I and II in Fig. 1, incident upon a coated optical fiber. Let the index of refraction and the radius of the

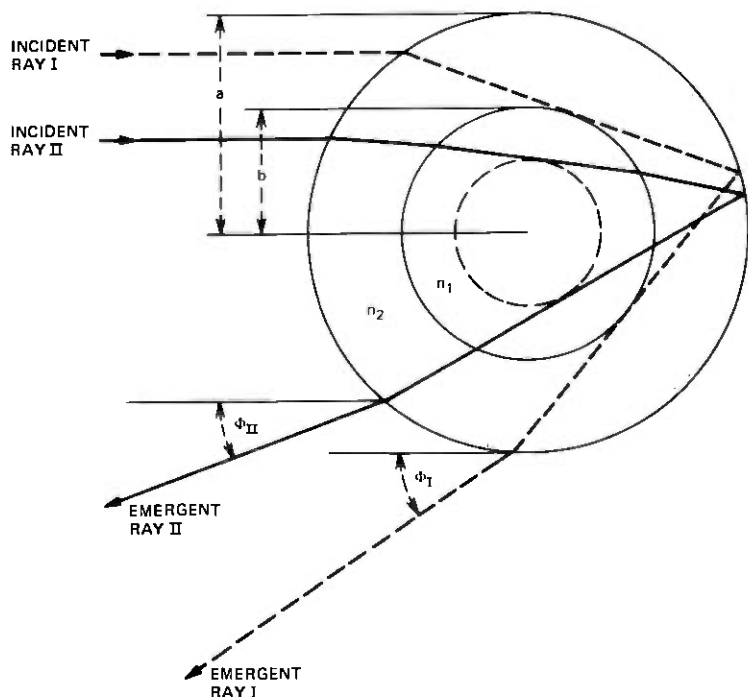


Fig. 1—Paths of rays of minimum deviation in a coated optical fiber. The situation is symmetric for rays incident upon the lower half of the fiber.

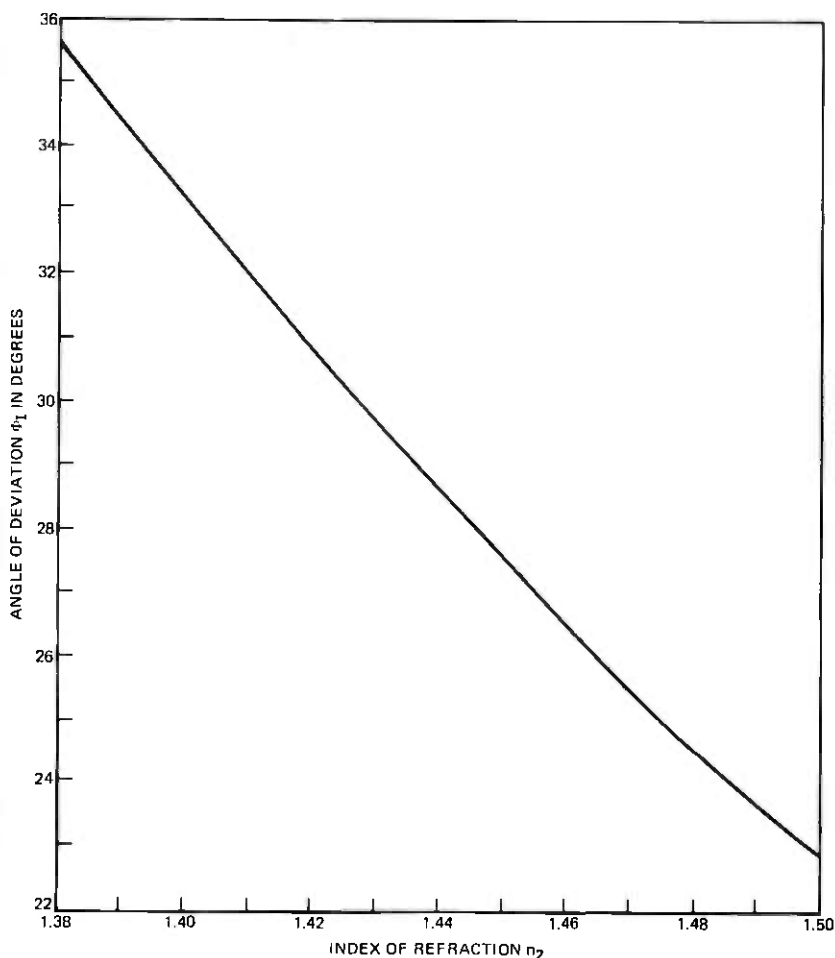


Fig. 2—Location of minimally deviated ray I as a function of the index of refraction of the coating  $n_2$ .

coating be  $n_2$  and  $a$ , respectively. For the purposes of the current analysis, the internal details of the fiber (indicated by the broken circle), which can be either an unclad, step-index, or graded-index variety, are neglected, and we let its index of refraction be  $n_1$  and its radius be  $b$ . We also neglect multiple internal reflections.

Ray I is refracted, traverses the coating, and is then reflected at the coating-air interface and exits making an angle of minimum deviation  $\phi_1$  with its incident direction given by<sup>10</sup>

$$\phi_1 = 4 \sin^{-1} \left[ \frac{2}{n_2 \sqrt{3}} \left( 1 - \frac{n_2^2}{4} \right)^{\frac{1}{2}} \right] - 2 \sin^{-1} \left[ \frac{2}{\sqrt{3}} \left( 1 - \frac{n_2^2}{4} \right)^{\frac{1}{2}} \right]. \quad (1)$$

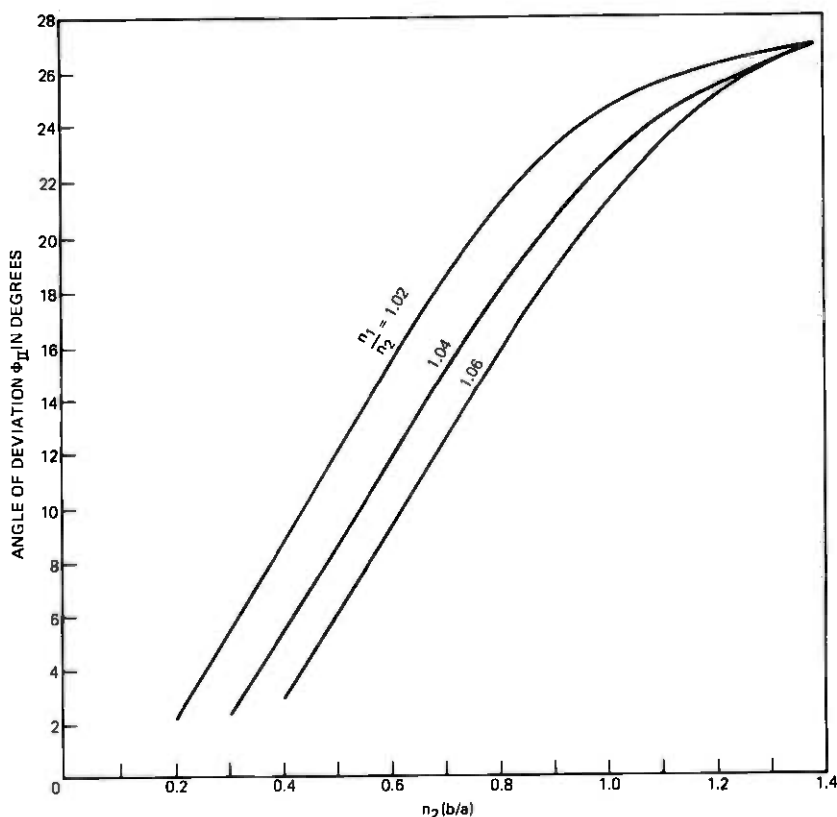


Fig. 3—Location of the minimally deviated ray II, as a function of  $n_2b/a$  for  $n_1/n_2 = 1.02, 1.04,$  and  $1.06$ .

A plot of  $\Phi_I$  versus  $n_2$  is given in Fig. 2. A maximum of intensity dependent only upon the refractive index of the coating,  $n_2$ , exists at this angle. Beyond  $\Phi_I$ , the backscattered pattern cuts off into a low level continuum.

Ray II, after being refracted by the coating, traverses the fiber, emerges into the coating, and is reflected by the coating-air interface. The ray then again enters the fiber and emerges into the coating and from there leaves the fiber, making an angle of minimum deviation  $\Phi_{II}$  with its incident direction.  $\Phi_{II}$  is a function of several angles and of  $n_1$  and  $n_2$ .<sup>11</sup>

Plots of  $\Phi_{II}$  determined by computer as a function of  $n_2b/a$  with  $n_1/n_2$  as a parameter are shown in Fig. 3 for  $n_1/n_2 = 1.02, 1.04,$  and  $1.06$ . For these calculations,  $n_1$  was held fixed at the fused-silica value of 1.457.

Figure 4 presents  $\Phi_{II}$  as a function of coating thickness ( $a - b$ ) for  $n_1 = 1.457$  and  $n_2 = 1.400$ . It is seen that a  $1\text{-}\mu\text{m}$  variation in thickness corresponds to an approximately  $0.1\text{-degree}$  shift in  $\Phi_{II}$ .

It is important to note that ray I does not see the fiber at all. For a given  $n_2$ , however, a critical fiber radius  $b_c$  (or alternatively, coating thickness) will exist beyond which ray I will no longer exist. This condition is given by<sup>11</sup>

$$b_c = a/n_2. \quad (2)$$

The disappearance of ray I is thus a very sensitive indication of a specific coating thickness. For example, if  $b = 50\ \mu\text{m}$ , a typical value, ray I will not be observed if the coating ( $n_2 = 1.4$ ) is less than  $20\text{-}\mu\text{m}$  thick. In general, the status of ray I is only an additional indicator, and coating-thickness measurements are based on the location of ray II. It is also important to note that distortions of the coating or fiber from the ideal circularity assumed here can have a significant effect on the location of  $\Phi_I$  and  $\Phi_{II}$ .<sup>12</sup>

### III. MEASUREMENT TECHNIQUE AND RESULTS

The experimental arrangement to observe the backscattered pattern is shown in Fig. 5.<sup>11</sup> Light from a cw *He-Ne* laser strikes plane mirror *M1* which reflects it to oscillating mirror *M2*. This serves to

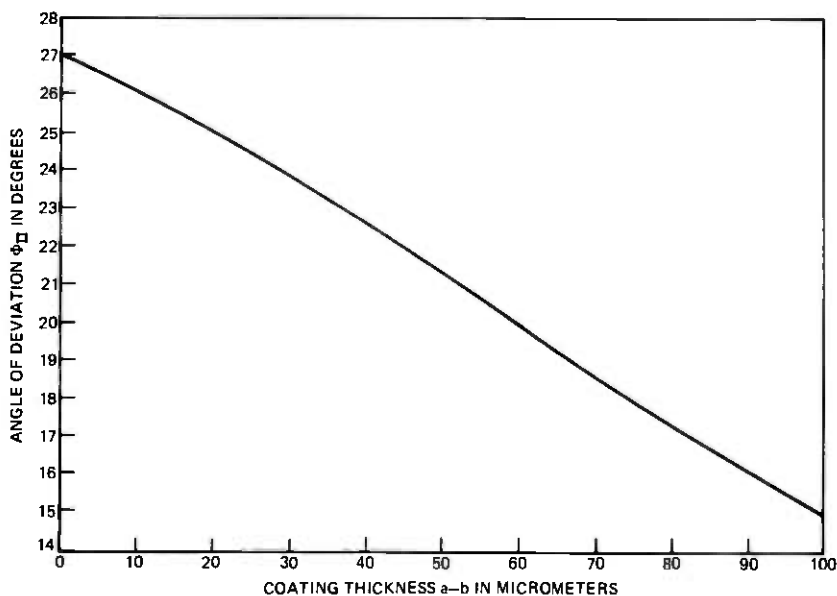


Fig. 4—Value of  $\Phi_{II}$  as a function of coating thickness  $a - b$  for a concentric and geometrically uniform fiber.

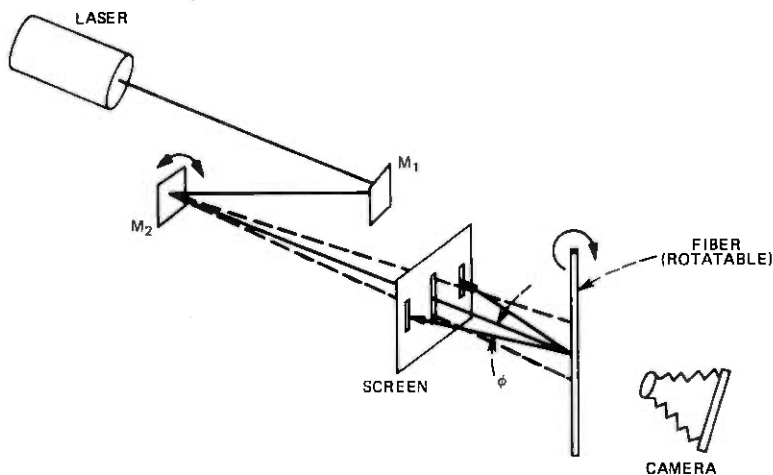


Fig. 5—Experimental arrangement to observe the backscattered patterns.

transform the approximately 1-mm circular beam into a line 1-mm wide, with length determined by the amplitude of oscillation, thus allowing for observations on an extended length of coated fiber, upon which the light impinges after passing through a slit in the observation screen. The fiber is held in a rotatable mount and the backscattered light falling on the screen is photographed with a  $4 \times 5$  framing camera. All of the results to be presented were obtained in this manner with stationary fibers.

A series of patterns, observed on the screen arising from a severely nonconcentric coated fiber, is shown in Fig. 6. The patterns are obtained as the fiber is rotated in 30-degree increments. The approximately  $150\text{-}\mu\text{m}$ -diameter glass fiber, also displayed in Fig. 6, is coated with a silicone resin which varies in thickness from a maximum of approximately  $85\ \mu\text{m}$  to a minimum of  $8\ \mu\text{m}$ . In this and all subsequent results, there is a one-to-one correspondence between a region in the backscattered pattern and a region in the approximately 65-mm illuminated length of fiber. The main fringes arising from rays I and II are labeled in the 0- to 150-degree orientations. The 0-degree origin of the rotational increments in this case was arbitrarily chosen to coincide with a maximum visibility of rays I and II. The light distribution exhibits large variations as the fiber is rotated due to the nonconcentricity of the coating. For example, in the 30-degree orientation, only one of the fringes corresponding to ray I appears; at 120 degrees, only the other one appears; and at 60 degrees both of them are absent. In all orientations, the fringes corresponding to rays II vary in location and in some positions in visibility. If observations of

the backscattered pattern were made for two mutually perpendicular orientations while such a fiber was being pulled, it would be readily ascertained by the visual appearance of the light distribution alone that the coating was nonconcentric and corrective measures could be taken.

An optical fiber with a somewhat improved coating concentricity is shown in Fig. 7 along with the resulting backscattered patterns taken at 30-degree increments. In this case, the silicone-resin coating

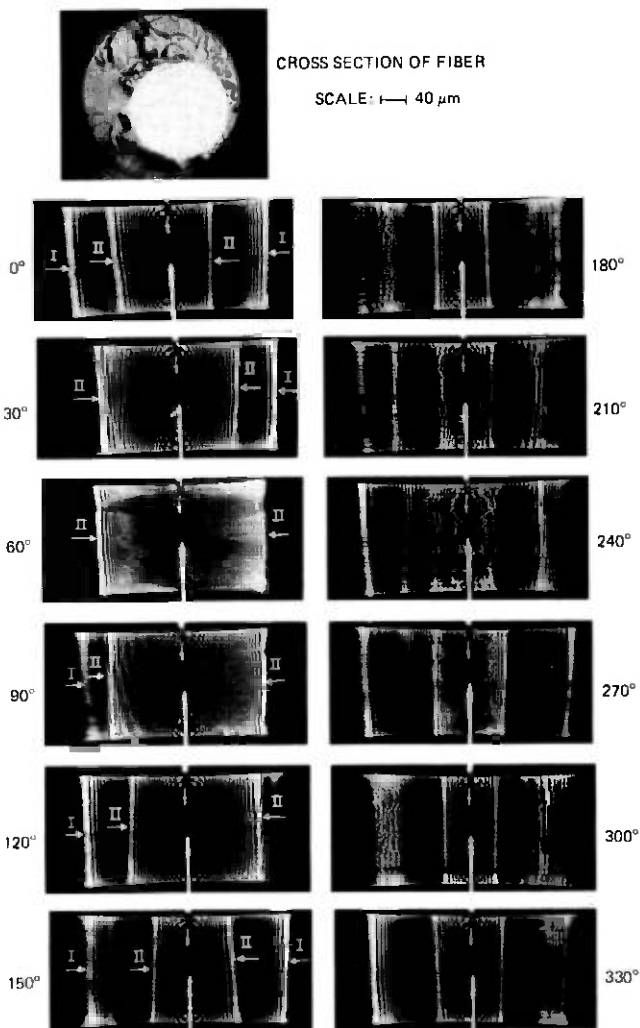


Fig. 6—Silicone-resin-coated fused-silica fiber with large nonconcentricity and associated backscattered patterns.

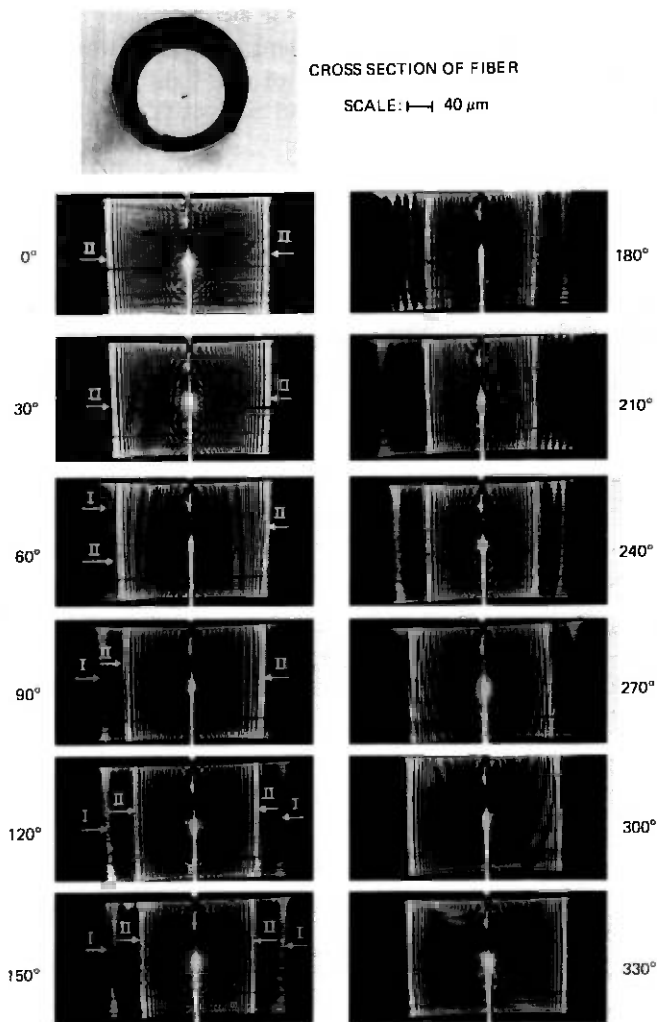
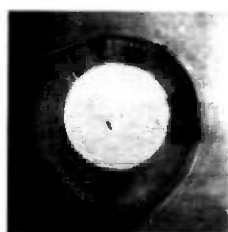


Fig. 7—Silicone-resin-coated fused silica fiber with coating thickness varying from  $24\ \mu\text{m}$  to  $52\ \mu\text{m}$  and associated backscattered patterns.

on the approximately  $145\text{-}\mu\text{m}$ -diameter fiber varies in thickness from  $24\ \mu\text{m}$  to  $52\ \mu\text{m}$ . The fringes arising from rays I and II are labeled in the 0- to 150-degree orientations. The light distributions exhibit considerably fewer variations compared with the previous fiber. Visual observations again are sufficient to detect nonconcentricity.

The silicone-resin coating on the optical fiber shown in Fig. 8 has a fair degree of concentricity, varying in thickness from approximately  $45\ \mu\text{m}$  to  $65\ \mu\text{m}$ . The backscattered light patterns shown in the same



CROSS SECTION OF FIBER

SCALE: 1—60  $\mu\text{m}$

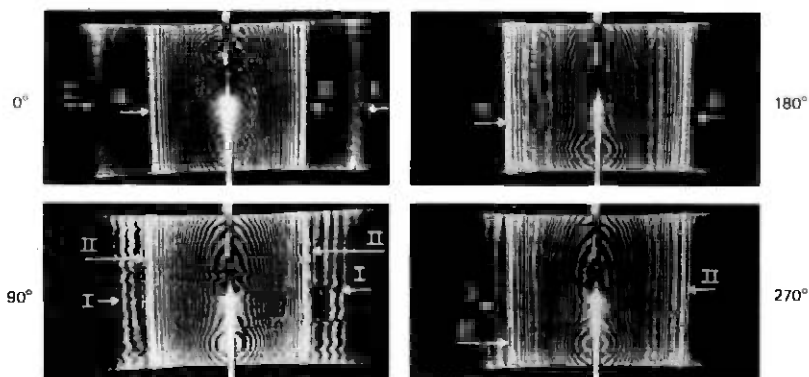


Fig. 8—Silicone-resin-coated fused-silica fiber with coating thickness varying from 45  $\mu\text{m}$  to 65  $\mu\text{m}$  and associated backscattered patterns at 90-degree increments. As in Figs. 6 and 7, a 6.5-cm length of fiber is illuminated.

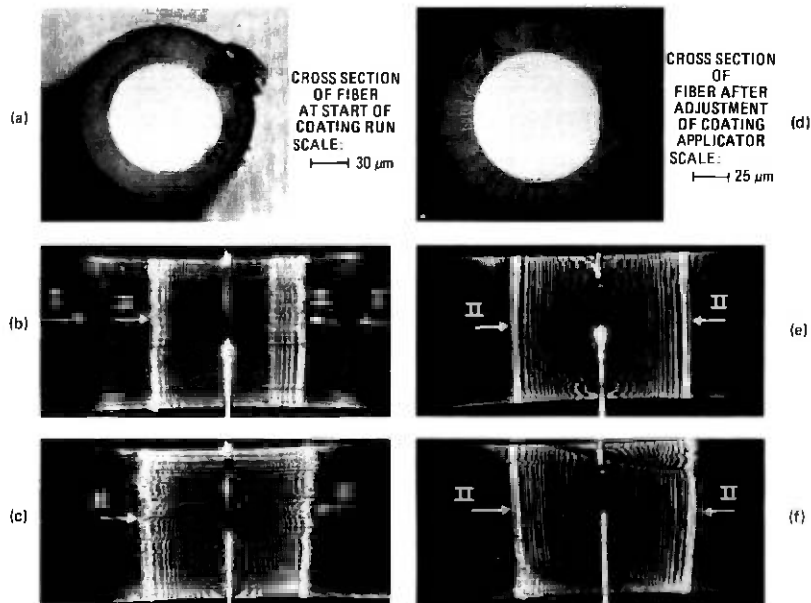


Fig. 9—On-line use of coating analyzer to improve concentricity.

figure were taken at 90-degree increments and indicate their sensitivity and ability to detect coating nonconcentricity from observations made in two perpendicular directions.

An example of the technique in use is afforded by the results in Fig. 9. The approximately 105- $\mu\text{m}$ -diameter glass fiber shown in Fig. 9a is a sample from the start of a silicone-resin-coating run. The coating thickness varies from 23  $\mu\text{m}$  to 36  $\mu\text{m}$ . This nonconcentricity is apparent in the two scattering patterns, Fig. 9b and c, taken at 90-degree orientations. After adjusting the coating applicator while observing the patterns for symmetry, as depicted by Fig. 9e and f, the coated-fiber sample appears as in Fig. 9d. The coating thickness now varies by less than 2  $\mu\text{m}$ , being about 28  $\mu\text{m}$  to 30  $\mu\text{m}$  thick.

The arrangement by which the real-time observations are made is depicted in Fig. 10. The beam from a 5-mW *He-Ne* laser, after being expanded in a manner similar to that of Fig. 5, strikes a beam splitter. A portion is transmitted directly to the fiber while the remainder, after reflections at the plane mirrors, impinges upon the fiber at right angles

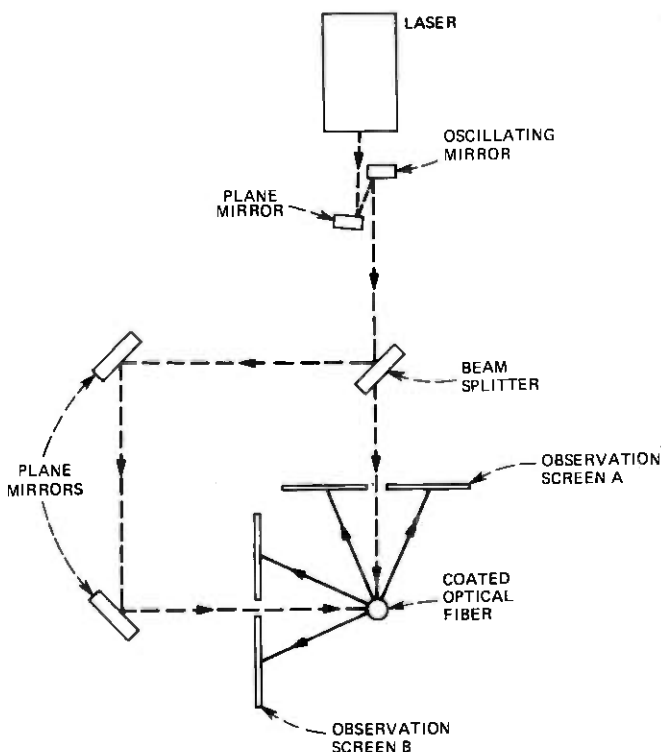
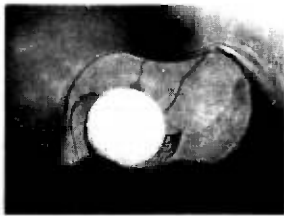


Fig. 10—Setup to monitor coating properties in on-line situation.



CROSS SECTION OF FIBER

SCALE:  $\text{---} \rightarrow 40 \mu\text{m}$

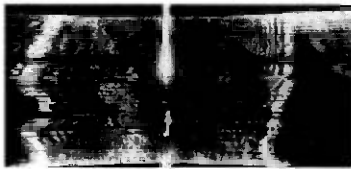
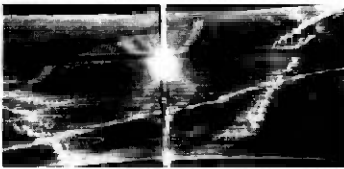
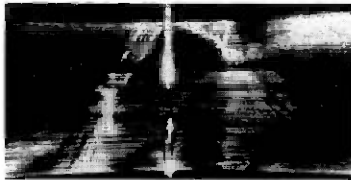


Fig. 11—Severely distorted plastic coating and associated backscattered-light patterns.

to the direct beam. The backscattered patterns are visually detected on two observation screens. Other components of the scattered light overlap the backscattered patterns, but due to their very different appearances, lower amplitudes and shifted locations present no problems.

The entire setup is mounted on a plate fastened to an  $x$ - $y$  positioner to allow real-time alignment with the fiber when necessary. The patterns are invariant to lateral motions of the fiber within the incident beams.<sup>10</sup> The position of the apparatus between the coating applicator and the take-up drum is determined by the coating state (before or after drying or curing) to be monitored. It is readily appreciated that the observation screen can be replaced or supplemented with detectors to automate the coating analysis.

In addition to observations of nonconcentricity, the technique is very sensitive to geometrical deformation and nonuniformities. Figure 11 shows a severely deformed silicone-resin-coated fiber along with some of its associated backscattered patterns. Such patterns indicate a problem and if corrective measures are not effective, the entire process can be stopped before more time and material were wasted.

The silicone-resin coating on the fiber shown in Fig. 12a appears to

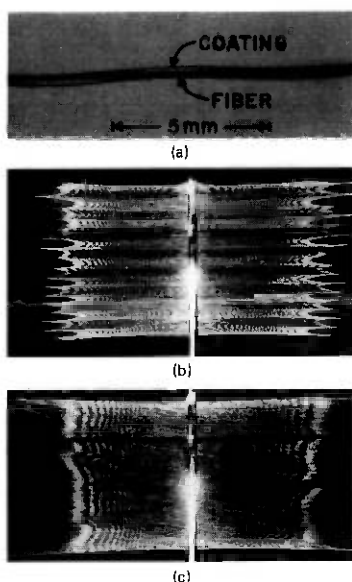


Fig. 12—Nonuniformly applied coatings and associated backscattered patterns. (a) and (b) Silicone resin. (c) Semitransparent polymer.

have been applied in some helical fashion. This is readily detected and observed in the associated scattering pattern, Fig. 12b.

The backscattered pattern of Fig. 12c arising from another coated fiber indicates a nonuniform coating. Despite the semicrystalline structure of the coating material applied to the fiber in this case, which renders it somewhat less transparent than silicone, the pattern is clear and can be used to analyze the coating.

#### IV. CONCLUSION

A sensitive, noncontacting, and nondestructive optical technique has been developed to evaluate the geometrical quality of plastic coatings on optical fibers both in laboratory and on-line situations. The method should prove valuable not only in analyzing coatings but also in developing the coating facilities themselves.

The technique has been applied to a variety, but not all, of the coatings currently under development. A necessary requirement for its implementation is that the coating material should be fairly transparent, a condition found satisfied by most of the plastic materials examined.

The theory of determining coating thickness is applicable only to the case of concentric coatings and should therefore be used with caution in other situations.

While visual observations have been emphasized, it would certainly be advantageous to automatically detect and electronically process the backscattered-light signal. This can be accomplished by known techniques utilizing photodiode arrays or vidicon scanning.

The method presented should also be applicable to extremely thick coatings as might be envisioned in fiber pigtail, jumper, or cabling operations and should aid in the production of uniform coatings in those areas as well.

## V. ACKNOWLEDGMENTS

The author would like to thank R. M. Derosier for the construction of the on-line coating-analysis apparatus, D. Marcuse for the computer calculations, and P. Kaiser for providing the fibers used in this study.

## REFERENCES

1. K. Yoshimura et al., "Low-Loss Plastic-Cladding Fibre," *Elect. Lett.*, *10*, No. 25/26 (December 12, 1974), pp. 534-535.
2. Y. Suzuki and H. Kashiwagi, "Polymer-Clad Fused-Silica Optical Fiber," *Appl. Opt.*, *13*, No. 1 (January 1974), pp. 1-2.
3. S. Tanaka et al., "Silicone-Clad Fused-Silica-Core Fibre," *Elect. Lett.*, *11*, No. 7 (April 3, 1975), pp. 153-154.
4. P. Kaiser, A. C. Hart, Jr., and L. L. Blyler, Jr., "Low-Loss FEP-Clad Silica Fibers," *Appl. Opt.*, *14*, No. 1 (January 1975), pp. 156-162.
5. L. L. Blyler, Jr. et al., "Low-Loss Silicone-Clad Fused Silica Fibers for Optical Communications," *Am. Ceram. Soc. Bull.*, *55*, No. 4, p. 455; Cincinnati Meeting, May 1-6, 1976, Paper 5-J1-76.
6. D. Gloge, "Optical Fiber Packaging and Its Influence On Fiber Straightness and Loss," *B.S.T.J.*, *54*, No. 2 (February 1975), pp. 245-262.
7. W. B. Gardner, "Microbending Loss in Optical Fibers," *B.S.T.J.*, *54*, No. 2 (February 1975), pp. 457-465.
8. C. R. Kurkjian et al. "Tensile Strength Measurements on Long Gage Lengths of Polymer-Coated Silica Fibers," *Am. Ceram. Soc. Bull.*, *55*, No. 4, p. 455; Cincinnati Meeting, May 1-6, 1976, Paper 8-J1-76.
9. A. H. Cherin and E. J. Murphy, "Quasi-Ray Analysis of Crosstalk Between Multimode Optical Fiber," *B.S.T.J.*, *54*, No. 1 (January 1975), pp. 17-45.
10. H. M. Presby, "Refractive Index and Diameter Measurements of Unclad Optical Fibers," *J. Opt. Soc. Am.*, *64*, No. 3 (March 1974), pp. 280-284.
11. H. M. Presby and D. Marcuse, "Refractive Index and Diameter Determinations of Step Index Optical Fibers and Preforms," *Appl. Opt.*, *13*, No. 2 (December 1974), pp. 2882-2885.
12. H. M. Presby, "Ellipticity Measurement of Optical Fibers," *Appl. Opt.*, *15*, No. 2 (February 1976), pp. 492-494.



## Ordering Techniques for Coding of Two-Tone Facsimile Pictures

By A. N. NETRAVALI, F. W. MOUNTS, and E. G. BOWEN

(Manuscript received June 23, 1976)

*This paper describes some techniques for efficient coding of two-tone (black and white) facsimile pictures. These techniques use the two-dimensional correlation present in spatially close picture elements to change the relative order of transmission of elements in a scan line. This ordering increases the average length of the runs of consecutive black or white elements in the ordered line, making the data more amenable to one-dimensional run-length coding. We describe several variations of the ordering scheme, which differ in complexity and coding efficiency and evaluate their coding efficiency. For a variety of 8-1/2 inch by 11-inch typed documents, road maps, and circuit diagrams scanned with 200 lines/inch, these techniques reduce the bit rate by 30 to 50 percent over and above the one-dimensional run-length coding along a scan line; for single-spaced typed material with 100 lines/inch, this reduction is about 25 percent. We compare one of our techniques with a two-dimensional compression technique recently proposed by Preuss. We show that our technique results in an entropy about 10 to 18 percent lower than that obtainable through Preuss' technique.*

### I. INTRODUCTION

Transmission and/or storage of two-tone (black and white) pictures, such as weathermaps, printed texts, etc., have been receiving considerable attention for some time. The practical importance of this problem is evidenced by the number of facsimile communication systems that are now available.<sup>1</sup> As the cost of electronics decreases faster than transmission costs, it is becoming advantageous to use sophisticated facsimile terminals to reduce transmission costs and time, and, indeed, many of the recent facsimile communication systems have resorted to various source encoding techniques to utilize the statistical redundancy between the spatially close picture elements to reduce the bit rate required for transmission.<sup>2-5</sup>

The picture elements along a scan line of a facsimile picture consist of runs of white picture elements (pels) separated by runs of black

picture elements. Values of the spatially close picture elements are significantly correlated. Source coding techniques, which do not reduce the "information content" of the pictures (i.e., it is possible to construct the original picture exactly without any degradation from the coded picture) use the statistical redundancy either along a single scan line or along many scan lines. One-dimensional run-length coding techniques<sup>6</sup> code the runs of black or white elements along a scan line. Development and performance of many different codes to code the runs have been a subject of many papers.<sup>7-9</sup> Some of these codes are capable of performing close to the entropy of the run-length statistics. Extensions of this basic run-length coding scheme have been made to include line-to-line correlations.<sup>10-12</sup> Two-dimensional correlations have also been used in development of block coding<sup>13</sup> as well as blob coding<sup>14</sup> methods.

In this paper, we describe techniques which use the two-dimensional correlation of the picture signals. Specifically, our techniques consist of changing the relative order of transmission of the picture elements along a scan line in such a way as to increase the average run length of the black and/or white elements. A reference signal is constructed from the previously transmitted data, and the data in the present line is ordered with respect to this reference signal. A memory is used to store the incoming bits of new data in a manner such that the address for storing a particular input bit is derived from the reference signal. At the end of the ordering period, the information stored in the memory is read out in a sequential manner and run-length coded. The receiver decodes the run-length coded information and stores it for a given ordering interval. The original data stream is then reconstructed by reading out the stored data in the same order in which it was stored at the transmitter. Our techniques can be classified into three broad categories. In the first category, described in Section 2.1, we order a line of picture data using the previously transmitted line immediately above it. Thus, the elements of the previous line are taken as the reference signal for ordering. In the second category, described in Section 2.2, we predict an element of a line from the value of a corresponding element from the previously transmitted line, and order the prediction error of the present line using elements of the previous line as the reference signal. The third category, which is described in Section 2.3, uses several already transmitted elements both from the present line and the previous line to define a state. We develop a predictor as a function of the state, as one which minimizes the prediction error conditioned on that state. We then sort the states in terms of probability of the prediction error associated with each

state, and order the prediction error (using the state-dependent predictor) according to the *goodness* of the state. During ordering, prediction errors corresponding to "good" (states with low probability of prediction error) and "bad" states are arranged in a sequence in two different parts of a memory. Contents of the memory are then read out and run-length coded for transmission. Since prediction errors corresponding to "good" states are mostly 0, this technique increases the length of the 0 runs and consequently achieves bit-rate reduction.

### 1.1 Summary of results

Our simulations indicate that, for pictures with 200 lines/inch, the previous-line-ordering technique reduces the entropy by about 20 percent over the entropy using one-dimensional run-length coding. Using previous-line-element-prediction and previous-line-ordering, this reduction is about 30 percent. State-dependent prediction and ordering reduce the entropy by about 33 to 50 percent. This reduction is about 25 percent for a picture with 100 lines/inch. Our results indicate that our state-dependent predictor does not vary significantly with pictures and, therefore, may not have to be transmitted for most pictures. Also, most of the advantage in using ordering based on "good-bad" state-groups is obtained by using only two state-groups. Among the algorithms that we compare ours with, is an algorithm recently proposed by Preuss.<sup>12</sup> We show that our algorithm is about 10 to 18 percent more efficient in terms of entropy.

## II. CODING ALGORITHMS

In this section, we describe each of our coding algorithms in detail and present results of our simulations on the computer. The computer simulations were done on pictures with 256 lines and 256 elements per line. The resolution was either 200 lines/inch or 100 lines/inch. The pictures we used included a drawing of a schematic, a map, and the inside part of text material (both single- and double-spaced typing). Sections of pictures used are shown in Fig. 1. Figures 1a and 1b are sections of single-spaced text with 200 lines/inch and 100 lines/inch, respectively. Figure 1c is double-spaced text with 200 lines/inch and Figure 1d is part of a circuit diagram. In addition to these, we used a map which is a section of page 19 from Ref. 15. As a measure of performance, we used the entropy of run-length statistics. We computed the entropy of black and white runs and the average black and white run lengths. Using these and eq. (1), we computed the entropy in bits/pel (assuming that the number of black and white runs are

8 kHz line rate  
, it uses 7th-  
order to increase  
respondingly  
a given trans-  
mission dot sequ

(a)

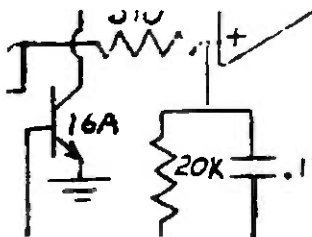
lines of 1000 elements).  
over a 1 MHz analog channel  
bit digital channel without  
in quasi-real time, so inte-  
ring is possible.

compatible with much existing  
uses 8 kHz line rate and 60  
however, it uses 7th-order li-  
terface to increase the pic-  
ture correspondingly increase  
for a given transmission

(b)

in a Unix di-  
rect done as follo-  
wing the Unix dire-

(c)



(d)

Fig. 1—Sections of figures viewed through a television camera and converted to a two-tone picture by a simple thresholding technique. Figures (a), (c), and (d) had 200 lines/inch and an array of  $256 \times 256$  was used for simulation. Figure (b) was taken at 100 lines/inch.

equal to  $N/2$ ) by:

$$H = \frac{H_w \cdot \frac{N}{2} + H_b \cdot \frac{N}{2}}{r_w \cdot \frac{N}{2} + r_b \cdot \frac{N}{2}} = \frac{H_w + H_b}{r_w + r_b}, \quad (1)$$

where

$H_w$  is the entropy of the white run statistic (bits/run),

$H_b$  is the entropy of the black run statistic (bits/run),

$r_w$  is the average white run length (pels/run),

$r_b$  is the average black run length (pels/run),

$H$  is the entropy in bits/pel.

### 2.1 Ordering present line with reference to previous line

This technique orders the present line with respect to the previous line. Consider a memory containing 256 cells (equal to the number of elements per line). We store in this memory elements from the present line. Assume for the sake of explanation that the memory is arranged along a line and memory location 1 corresponds to the left-hand side and location 256 corresponds to the right-hand side of the memory. If the first element of the previous line is white ( $=1$ ), then we put

the content of the first element of the present line on the left-hand side of the memory. If, on the other hand, the previous line element is black (=0), we put the first element of the present line on the right-hand side of the memory. We then put the second element on the right-hand or left-hand side of the memory depending on whether the second element of the previous line is black or white. This process is continued until the entire present line is ordered and the memory is filled. The information stored in the memory is coded as runs of black and white elements. It is easy to see that the present line can be uniquely reconstructed from the knowledge of the run lengths of the ordered line since the ordering information is known to the receiver.

The entropies obtained using the ordered run-length statistics are given in Table I. This table also shows, for comparison purposes, the entropy of the picture using the statistics of simple one-dimensional (along a scan line) unordered run lengths. The ordered entropy of the run lengths varies between 0.12 bit/pel to 0.24 bit/pel for 200 lines/inch resolution pictures. The increase in coding efficiency (=decrease in entropy) due to ordering over plain run-length coding is of the order of 20 to 25 percent. This increase in efficiency is decreased to 16 percent for the picture with 100 lines/inch. In Fig. 2, we show the original picture (same as Fig. 1a) and its ordered version. It is interesting to note that the picture elements on the left side of the ordered picture are mostly white and those on the right side of the picture are

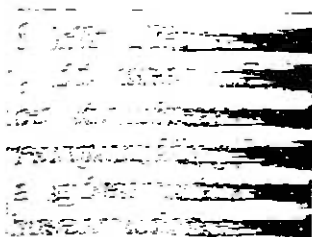
Table I—Entropy comparisons for different coding algorithms

Coding Technique	Entropy (bits/pel) Picture				
	1	2	3	4	1 at 100 lines/in.
(1) One-dimensional run-length coding	0.30	0.16	0.21	0.23	0.38
(2) Present line ordered with reference to previous line	0.24	0.12	0.16	0.17	0.32
(3) Finite length ordering (length = 64) of Technique (2) (length = 128)	0.29 0.28	0.17 0.15	— —	— —	— —
(4) Run-length coding of prediction error using previous line predictor	0.25	0.13	0.15	0.16	0.35
(5) Technique (4) with ordering using previous line	0.21	0.11	0.14	0.15	0.31
(6) Run-length coding of prediction error using state-predictor	0.24	0.13	0.15	0.16	0.34
(7) Technique (6) with state-ordering using 2 state-groups	0.20	0.10	0.11	0.12	0.30
4 state-groups*	0.20	0.10	0.11	0.12	0.30
16 state-groups*	0.19	0.099	0.11	0.119	0.29
Technique of Preuss using 2 state-groups*	0.22	0.11	0.13	0.14	0.34

\* These entropy numbers do not include extra bits required to specify number of elements in each state-group.

8 kHz line rate  
, it uses 7th-  
ce to increase  
respondingly  
a given trans  
osen dot sequ

(a)



(b)

Fig. 2—(a) Picture of original. (b) Present line ordered with respect to previous line.

mostly black. If the vertical correlation between the scan lines was perfect, there would be no scattered black and white elements; all the white elements would be to the left and all the black elements would be to the right. The increase of coding efficiency is intuitively obvious by comparing both the original and the ordered pictures of Fig. 2.

### 2.1.1 Finite length ordering

To evaluate the effects on coding efficiency of ordering only a part of the line, we simulated finite length ordering. This has the advantage to some extent of localizing along the horizontal direction the effect of transmission errors. However, vertical propagation of transmission errors is still possible. To illustrate this scheme, consider two memories of 128 cells each (half the number of samples/line). We then order the elements of the present line as before for each half of the line. However, in the first memory, we put elements corresponding to black elements of previous line to the left side and elements corresponding to the white elements of the previous line to the right side; whereas, for the second memory we reverse the sides for the black and white elements, i.e., elements of the present line corresponding to the black elements of the previous line are put on the left side. This minimizes the effects of "discontinuity" at the boundary of the two memories. The two memories are now arranged back to back, and their contents are read out sequentially and are run-length coded. The results of simulating this scheme are shown in Table I for different sizes of the memories.

The increase in the entropy by dividing the line into two segments is significant. Thus, there is a considerable loss in coding efficiency due to finite length ordering. This allows us to conclude that by ordering two lines instead of parts of a line and arranging them back to back, as above, there may be further improvement in coding efficiency.

### 2.2 Ordering present line prediction errors with reference to previous line

This coding technique is similar to the one described in Section 2.1, except that now we order the prediction errors of the present line. We take the predictor to be the corresponding picture element in the previous line. We now order this prediction error as before; i.e., if the previous line has a white element, we put the prediction error of the present line to the left side of the memory and vice versa. As in the previous technique, from the ordered line, it is easy to decode uniquely the contents of the present line.

The entropy of the pictures using the run lengths of the ordered prediction error is between 0.11 bit/pel and 0.21 bit/pel for pictures with 200 lines/inch, as seen from Table I, and this amounts to a 30 to 35 percent decrease in entropy over simple one-dimensional run-length coding. To calculate the advantage of ordering, we also measured the entropy of the picture using the run-length statistics of the prediction error with the previous line element as predictor. The entropy of this, which is shown in Table I, varied between 0.13 bit/pel to 0.25 bit/pel, for pictures with 200 lines/inch. Thus, the reduction in entropy due to ordering was 7 to 16 percent over and above the entropy of the prediction errors. For the picture with 100 lines/inch, ordering the prediction errors brought the entropy down to 0.31 bit/pel, which is a reduction of about 17 percent over the entropy of one-dimensional run-length coding.

### 2.3 State-dependent prediction and ordering

The technique described in this section differs from the two earlier techniques in its use of more picture elements spatially close to the present element. It uses these elements to define a state of the present picture element. We develop a predictor for each state and use the state also to order the present line. Using this technique, it is possible to *separate* the process of prediction and ordering.

To illustrate the technique, consider the picture element configuration shown in Fig. 3. The state of the present picture element  $X$  is defined by elements  $A$ ,  $B$ ,  $C$ , and  $D$ . Thus, state  $Z$  is the four-tuple

$$Z = (A, B, C, D). \quad (2)$$

Since each of the elements  $A$ ,  $B$ ,  $C$ , and  $D$  can have two possible values,

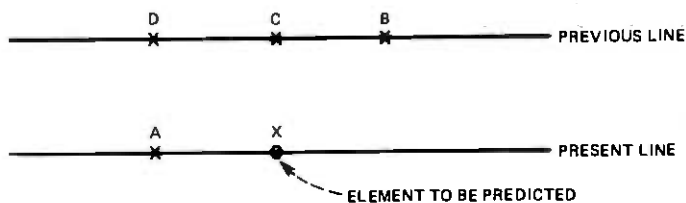


Fig. 3—Configuration for state definition.

there are 16 states, which we denote by the set  $\{Z_i\}$ ,  $i = 1, \dots, 16$ . The development of a state-dependent predictor is our next task. Such a development is as old as predictive coding itself.<sup>12,16</sup> The predictor is developed by the following criterion. We first compute  $P(X = \text{'Black'} | Z = Z_i)$ , the probability of the present picture element  $X$  being Black given the state  $Z = Z_i$ . The predictor  $C(Z_i)$  for a given state  $Z_i$ , is then,

$$\begin{aligned}
 C(Z_i) &= \text{'Black'} && \text{if } P(X = \text{'Black'} | Z = Z_i) > 0.5 \\
 &= \text{'White'} && \text{otherwise.}
 \end{aligned}
 \tag{3}$$

It is easy to see that this predictor minimizes the probability of making an error given that a particular state has occurred. We have calculated the predictor for each state using several pictures. These are shown in Table II. For most states, the predictors do not depend upon the picture used, except for a few states that are marked with asterisks in Table II; thus, it is not necessary to transmit the predictors for each different picture. We shall evaluate the effects of using the predictors of one picture for other pictures.

Having developed the predictor, we sort the states into two groups. The probability of correct prediction using the state-dependent predictor is shown in Table II. We note that the probability of correct prediction is always higher than 0.5 due to our predictor being a minimum prediction error predictor. States which have high probability of correct prediction will be called "good" states. Our ordering strategy depends upon the goodness of the state. Let the 16 states be divided into two groups: one containing "good" states and one containing "bad" states. Our state-dependent ordering algorithm then works as follows: we first evaluate the prediction error for a particular picture element in the present line by using the state-dependent predictor. Then, if the state is a "good" state, we put the prediction error on the left side of the memory, and if the state is "bad", we put the prediction error on the right side of the memory. In all our simulations, we used a threshold of 0.8 for the probability of prediction error to determine the goodness of a state. Having ordered the predic-

tion error, we then code the run lengths of the prediction error. It is easy to see that the line of data can be uniquely constructed from the coded run lengths of the prediction error. The entropy of run lengths of such ordered prediction errors for different pictures is given in Table I. For pictures with 200 lines/inch resolution, the entropy varies between 0.10 bit/pel to 0.20 bit/pel. This represents a decrease of between 33 percent and 49 percent over the entropy of simple one-dimensional run-length coding. We evaluated, for comparison purposes, the entropy of the picture using the run-length statistics of the prediction error. This varies between 0.13 bit/pel to 0.24 bit/pel for the pictures with 200 lines/inch. It is clear then that state-dependent ordering allows us to decrease the entropy by about 16 to 25 percent over and above the entropy obtained by using the prediction error of the state-dependent predictor.

We described a scheme in which only two groups of states were used for ordering purposes. To evaluate the effect of using more than two groups, we divided the states into 16 groups, and ordered the prediction error as before. In the case of more than two groups of states, it is not possible to decode the original line of picture data from coded run lengths unless extra information about the number of elements in each state-group is specified for each line. The entropy of the run-length statistic using more than two state-dependent groups is shown in Table I. These figures of entropy do not include the extra information that is required to be transmitted about the number of elements in the group. The increase of coding efficiency by using more than two groups is somewhat small and it would be offset completely by the extra information mentioned. Thus, most of the decrease of entropy due to state-dependent ordering is obtained by using only two groups.

In all of the state-dependent coding algorithms, we have not made an effort to optimize several of the coder parameters. Thus, for example, when the state-groups are less than 16, we could optimize the groupings of the states. The groupings that we used were intuitive and somewhat ad hoc. We did vary the groupings in the case of two groups and found that the entropies did not change significantly. It appears that optimization of groupings may not result in any significant entropy reduction.

### **2.3.1 Sensitivity to picture variation**

Picture content affects three parameters of our state-dependent coding algorithms: the state-dependent predictor, the entropy numbers which depend on the statistics of the run lengths, and the definition of "good" and "bad" (or the groupings) states. We studied the sensitivity of our coding algorithms by considering the variation of predic-

Table II—State-dependent predictors

State No.	State Definition	Picture 1 Single-Space Space Type			Picture 2 Double-Space Space Type			Picture 3 Circuit Diagram			Picture 4 Road Map			Picture 1 Single-Space Type (100 Lines/In)			Weather Map (Prenus)	
		Pred.	Prob. of Cor- rect Pred.	Prob. of State	Pred.	Prob. of Cor- rect Pred.	Prob. of State	Pred.	Prob. of Cor- rect Pred.	Prob. of State	Pred.	Prob. of Cor- rect Pred.	Prob. of State	Pred.	Prob. of Cor- rect Pred.	Pred.	Prob. of Cor- rect Pred.	
1		B	0.96	0.0553	B	0.97	0.0354	B	0.97	0.0366	B	0.97	0.0496	B	0.84	0.0229	B	0.911
2		B	1.00	0.0076	B	1.00	0.0040	B	1.00	0.0043	B	0.96	0.0035	B	0.90	0.0079	B	0.991
3		B	1.00	0.0001	B	0.83	0.0001	B	1.00	0.00003	W*	0.70	0.0014	B	0.51	0.0008	B	0.663
4		B	0.99	0.0033	B	1.00	0.0017	B	0.99	0.0013	B	0.85	0.0013	B	0.99	0.0049	B	0.952
5		B	0.83	0.0291	B	0.86	0.0156	B	0.80	0.0182	B	0.81	0.0152	B	0.68	0.0207	B	0.768
6		B	1.00	0.0008	B	1.00	0.0002	B	0.98	0.0009	B	0.82	0.0014	B	0.87	0.0054	B	0.920
7		W	0.74	0.0260	W	0.76	0.0137	W	0.81	0.0155	W	0.81	0.0175	W	0.74	0.0366	W	0.553
8		B	0.55	0.0169	B	0.54	0.0084	B	0.61	0.0086	B	0.58	0.0089	W*	0.55	0.0259	B	0.501

Table II—Continued

State No.	State Definition	Picture 1 Single-Space Type		Picture 2 Double-Space Type		Picture 3 Circuit Diagram		Picture 4 Road Map		Picture 1 Single-Space Type (100 Lines/In)		Weather Map (Frons)	
		Pred.	Prob. of Correct Pred.	Pred.	Prob. of Correct Pred.	Pred.	Prob. of Correct Pred.	Pred.	Prob. of Correct Pred.	Pred.	Prob. of Correct Pred.	Pred.	Prob. of Correct Pred.
9		W	0.63	W	0.60	W	0.69	W	0.70	W	0.71	W	0.816
10		B	0.71	B	0.72	B	0.80	B	0.78	B	0.52	B	0.532
11		W	1.00	W	1.00	W	1.00	W	0.88	W	0.97	W	0.912
12		W	0.85	W	0.81	W	0.82	W	0.84	W	0.83	W	0.810
13		W	0.84	W	0.97	W	0.87	W	0.53	W	0.60	B	0.609
14		B	0.86	B	0.75	B	0.67	B	0.88	B	0.85	B	0.885
15		W	1.00	W	1.00	W	1.00	W	0.99	W	0.94	W	0.988
16		W	0.99	W	1.00	W	1.00	W	1.00	W	0.99	W	0.996

\* Varied with pictures.

 = Black = B.

 = White = W.

tors. The second factor mentioned could be studied by developing a specific code based on some run-length statistics (of one of the pictures, or some "average" picture) and then using it on all the pictures. We did not study this aspect of sensitivity of our algorithm. As mentioned in the previous section, we studied the variation of the entropy with groupings and found that the variation was not too sensitive. Thus, it appears that the groupings-information need not be computed or transmitted for each picture.

From Table II, it is clear that for a resolution of 200 lines/inch, the predictors are identical for all states for pictures of single-spaced typing, double-spaced typing, and schematic. This may be a result of our using a predictor based on the local information surrounding the picture element. In the case of a map, however, there are two states that have a different predictor compared to the first three pictures. Both these states were regarded as "bad" states for the coding of the map. We used the predictor of the first three pictures for the coding of the map; and using two state groups, we found a 3-percent increase in the entropy. Also, in the case of the picture with 100 lines/inch, there is only one state (state number 8) which had a different predictor than the first three pictures. This was again a "bad" state. For this picture, we found the increase in entropy of about 2 percent. This allows us to conclude that it may not be necessary to compute and transmit the state-dependent predictor information for each picture.

#### **2.4 Comparison with the algorithm of Preuss**

Most coding algorithms perform differently for different pictures. To compare our results with other two-dimensional coding techniques, we implemented a coding algorithm proposed by Preuss.<sup>7</sup> This also allowed us to bring out certain similarities and dissimilarities between our algorithm and that of Preuss. Preuss has developed a state-dependent predictor analogous to our predictor. This predictor is shown in Table II. It is seen that his predictor differs from our predictor for the first three pictures only for state number 13. Also, it differs from our predictor for the first picture (100 lines/inch) for state numbers 8 and 13. In our simulation of Preuss' scheme, we used the predictor tuned to the particular picture rather than Preuss' predictor. Preuss computes the prediction errors analogous to our scheme, and then codes the run lengths between the prediction errors for each of the state-groups separately, using a different run-length code for each state-group. We, on the other hand, use the state-groups to order the present line and encode the run lengths of the entire ordered line of the prediction errors. Preuss has to specify the number of elements

in each state-group;\* for  $K$  state groups with  $N$  elements in each line, this may amount to  $(K - 1) \log_2 N$  extra bits/pel. In our algorithm, we do not need transmission of such information for  $K = 2$ . In Preuss' scheme, the run lengths have to be terminated at the end of each state-group for each line, but in our algorithm, a run may begin in one state-group and extend all the way up to the end of the line, crossing several state-groups. Despite these disadvantages, we thought that Preuss' scheme may result in lower entropy, since his run-length code was matched to the run-length statistics of the prediction errors corresponding to each state-group. We simulated Preuss' scheme using two state-groups that were the same as those used for our algorithm. Results of this simulation are given in Table I. Entropy numbers given for Preuss' scheme do not include the extra information required for the number of elements in each state-group. It is seen from this table that, compared to our scheme using two state-groups, Preuss' scheme results in a 10- to 18-percent increase in entropy. Thus, our scheme appears, at least for the pictures we used, to be more efficient.

### III. DISCUSSION AND SUMMARY

We have presented three different algorithms for the coding of two-tone pictures. All three algorithms are "information" preserving, and, therefore, it is possible to decode exactly the original picture with no approximations. We have compared our results (only in terms of entropy) with some standard algorithms such as: (i) one-dimensional run-length coding, (ii) run-length coding of the prediction errors using several different two-dimensional predictors, and (iii) a two-dimensional algorithm of Preuss. We found our algorithm to be 10 to 18 percent more efficient than the algorithm of Preuss. Admittedly, this is not a complete comparison. Other parameters, such as the number of samples per line (we used only 256) and varying picture material, may offset the comparisons. Also, we did not study many other aspects important for a coding system, including the performance in the presence of transmission channel errors.

Our technique can be extended by proper definition of the state to the case of two-tone dithered pictures. This will be reported in a future paper.<sup>17</sup>

### IV. ACKNOWLEDGMENTS

This work was performed on the picture processing facility developed mainly by J. D. Beyer and R. C. Brainard. Also, our work

---

\* In a private communication, Preuss has shown that his scheme can be modified so that the number of elements in each of the state-groups need not be transmitted.

was made easier by many of the general purpose programs developed by B. G. Haskell.

## REFERENCES

1. D. M. Costigan, "FAX: The Principles and Practice of Facsimile Communication," New York: Chilton, 1971.
2. D. Hochman and D. R. Weber, "DACOM Facsimile Data Compression Techniques," 1970 Int. Conf. on Communications, pp. 20.14-20.21.
3. B. M. Rosenheck, "FASTFAX, A second Generation Facsimile System Employing Redundancy Reduction Techniques," IEEE Trans. Commun. Tech., *COM-8* (December 1970), pp. 772-779.
4. C. G. Beaudette, "An Efficient Facsimile System for Weather Graphics," in *Picture Bandwidth Compression*, New York: Gordon Breach, 1971, pp. 217-229.
5. R. B. Arps, "Bibliography on Digital Graphic Image Compression and Quality," IEEE Trans. Inform. Theory, Vol. 20 (January 1974), pp. 120-122.
6. J. Capon, "A Probabilistic Model for Run-Length Coding of Pictures," IRE Trans. Inform. Theory, *IT-5* (1959), pp. 157-163.
7. D. A. Huffman, "A Method for the Construction of Minimum Redundancy Codes," Proc. IRE, *40* (September 1952), pp. 1098-1101.
8. W. W. Happ, "Coding Schemes for Run-Length Information Based on Poisson Distribution," National Telemetry Conference Record, April 1969, pp. 257-261.
9. H. Meyer, H. G. Rosdolsky, and T. S. Huang, "Optimum Run Length Codes," IEEE Trans. Commun., *COM-22* (June 1974), pp. 826-835.
10. T. S. Huang, "Run-Length Coding and Its Extensions," in *Picture Bandwidth Compression*, New York: Gordon Breach, 1972, pp. 231-266.
11. P. A. Stern and W. Heinlein, "Facsimile Coding Using Two-Dimensional Run Length Predictions," International Seminar on Digital Communications, Zurich, 1974, pp. 170-176.
12. D. Preuss, "Comparison of Two-Dimensional Facsimile Coding Schemes," International Conference on Communications, June 1975, pp. 7.2-7.16.
13. M. Kunt, "Comparison de Techniques d'Encodage Pour la Reduction de Redondance d'Images Fac-simile a deux Niveaux," Thesis, Ecole Polytechnique Federale de Lausanne, 1974.
14. A. J. Frank, "High Fidelity Encoding of Two-Level, High Resolution Images," International Conference on Communications, June 1973, pp. 26-5-26-1.
15. State Farm Road Atlas: United States, Canada, Mexico, New York: Rand McNally, 1965.
16. J. S. Wholey, "The Coding of Pictorial Data," IRE Trans. Inform. Theory, *IT-7* (April 1961), pp. 99-104.
17. A. N. Netravali, F. W. Mounts, and J. D. Beyer, "Techniques for Compression of Dithered Two Level Pictures," unpublished work.

## Last-Trunk-Usage Measurements in Step-by-Step Switching Systems

By B. R. LaCAVA, W. D. MILLER, and B. YAGED

(Manuscript received July 22, 1976)

*A measurement approach is described which provides the capability of detecting traffic congestion in the graded multiples of a step-by-step switching system. The basic idea is to measure the load carried on the last trunk of each graded multiple and, using the techniques described, to determine the congestion level in each grading. The method, which requires only one lead per grading, works because Bell System grading patterns, which differ in structure depending on size, all have a common last-choice trunk and because the load carried on the last-choice trunk increases as the congestion in a grading increases. The basic idea and the interpretation of last-trunk-usage data in the presence of day-to-day variations in the offered load for configurations with and without rotary out-trunk switches are described in detail. Last-trunk-usage measurements are compared with other possible traffic measurements on gradings in terms of effectiveness in detecting various service impairments. The statistical accuracy of load and blocking estimates from last-trunk-usage measurements is also discussed. The result is a simple, effective measurement technique with the combined advantage of rapid detection of gradings with service problems and relative ease of implementation.*

### I. INTRODUCTION

Because of physical limitations, the trunks that connect the successive switching stages in a step-by-step switching system are arranged in sets of partial-access patterns called graded multiples (also called gradings, graded subgroups, or subgroups). The Bell System uses standard patterns for the gradings; a representative configuration is shown in Fig. 1. A call arriving hunts across the 10 trunks marked as heavy lines to find an idle trunk; if these 10 are busy, the call is blocked with a reorder tone returned to the customer. Details of the traffic flow through the system are given in Ref. 1. A long-standing problem in step-by-step offices has been the difficulty in detecting traffic congestion in the graded multiples, since detailed measurements are not obtained.

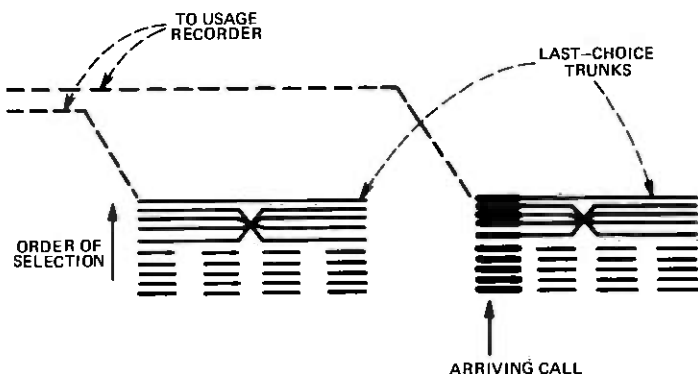


Fig. 1—Typical step-by-step subgroups showing limited trunk access for an arriving call.

In this paper, a new measurement approach is described which provides an economical and effective means for identifying specific graded multiples with substandard blocking levels. The basic idea is to capitalize upon the fact that, although the Bell System patterns differ in detailed structure depending upon the number of trunks, they all have a common last-choice trunk. Thus, the traffic performance, i.e., fraction of calls blocked, of a graded multiple can be monitored by measuring the load carried on the last-choice trunk (see Fig. 1). As the congestion in a grading increases, the load carried on the last trunk also increases. By properly interpreting the last-trunk usage (LTU), it is possible to infer the congestion level of each grading. Since only one connection per grading is required, the method makes efficient use of measurement equipment. The data can be collected by a variety of available usage-measuring equipment. Notice that the wiring can be validated by making the last trunk busy during nonpeak hours and checking for the correct usage measurement. Also, it is possible to detect (and thus avoid possible data misinterpretation) whenever subgroup performance cannot be determined due to the last trunk having been taken out-of-service, since its usage will appear as 36 CCS (hundred call seconds) in each hour.

Notice that this measurement approach is an application of a more general concept wherein the traffic performance of a set of servers is evaluated by measuring the behavior of one carefully selected element of the set. It is possible that this general concept may have broader applicability and should be considered in designing new measurement techniques.

Section II provides an overview of the measurement procedure and describes the model used to develop the last-trunk-usage procedures.

Section III describes the additional considerations required when the subgroups access rotary out-trunk switches (rots). Section IV discusses the use of LTV and other possible traffic measurements in detecting congestion problems—general overloads, imbalances between subgroups, and imbalances within subgroups. The LTV measurement procedure does not detect equipment irregularities. Section V relates the statistical accuracy of blocking and offered-load estimates to inherent variations in LTV data. Finally, Section VI discusses the application of the method.

## II. OVERVIEW OF LAST-TRUNK-USAGE PROCEDURES

The LTV monitoring procedures were developed using a computer simulation model of step-by-step ( $S \times S$ ) graded multiples.<sup>1</sup> The model has the following properties: Poisson arrivals, inherent load-

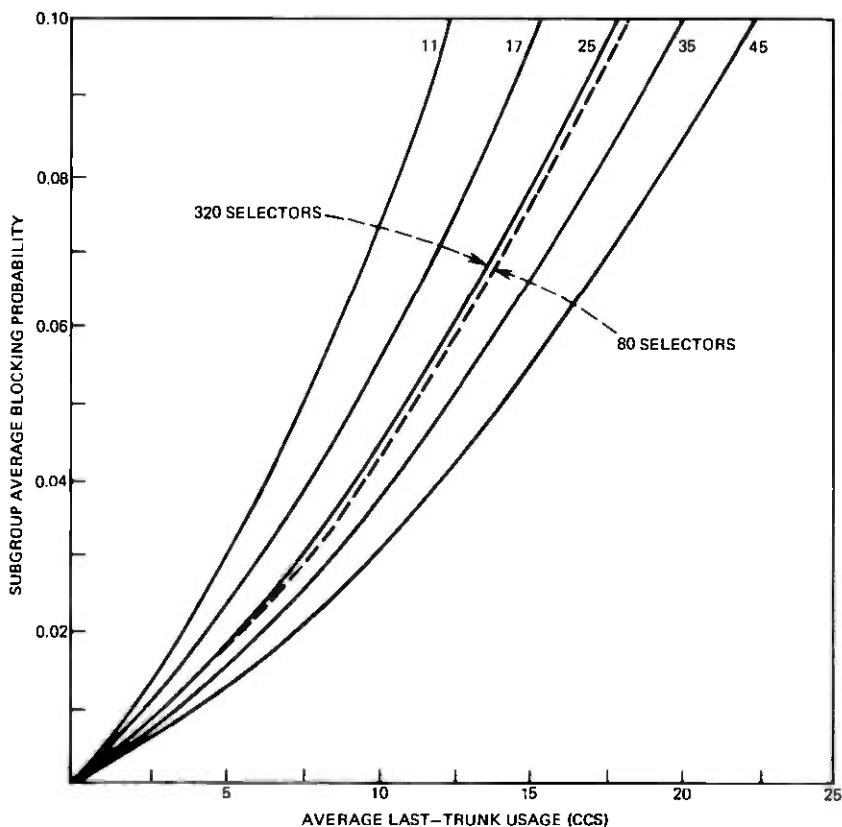


Fig. 2—Subgroup average blocking probability versus average last-trunk usage for 11-, 17-, 25-, 35-, and 45-trunk gradings with low day-to-day variation in offered load.

balancing, blocked calls cleared, and a negative exponential distribution for holding times. Retrials are not included in the model. A representative set of grading patterns was selected for detailed study. For each grading, the simulation was initially used to determine the equilibrium blocking and last-trunk usage over an appropriate range of offered loads.

Figure 2 shows the relationship between average blocking and average LTU for several gradings. In this paper, "average blocking" means "average call congestion." The use of average blocking and average LTU, rather than their equilibrium values, is appropriate since it is assumed that the offered loads will vary on different days according to the *low* day-to-day variation model;<sup>2</sup> measurements during a time-consistent hour must be averaged over several days to provide stable results (and reduce the possible impact of a single long-holding-

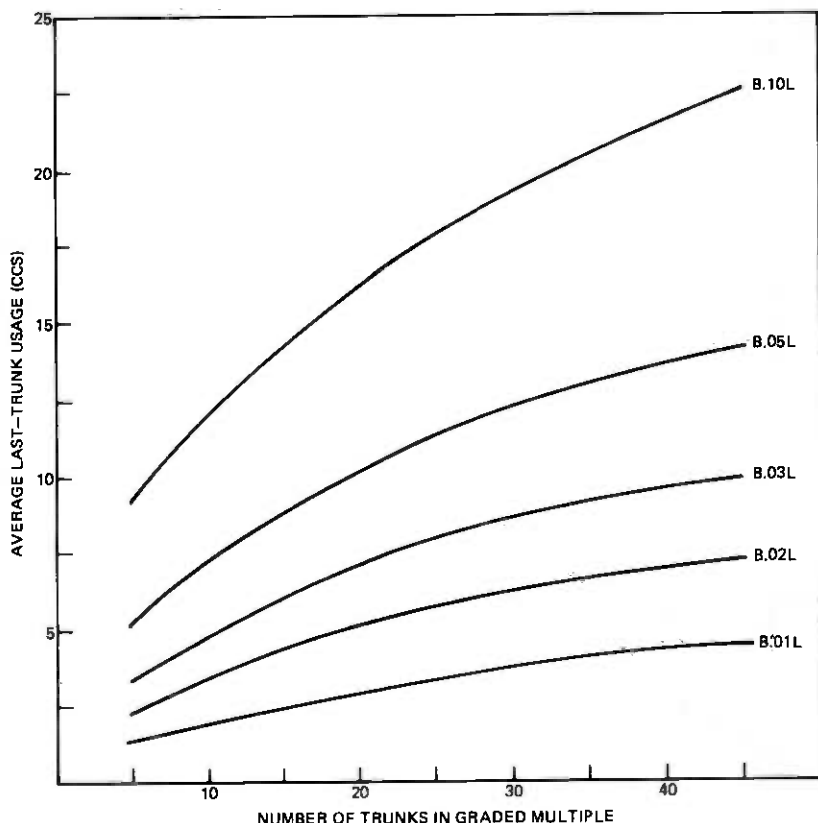


Fig. 3—Average last-trunk usage versus the number of trunks in the graded multiple for blocking at B.01L, B.02L, B.03L, B.05L, and B.10L.

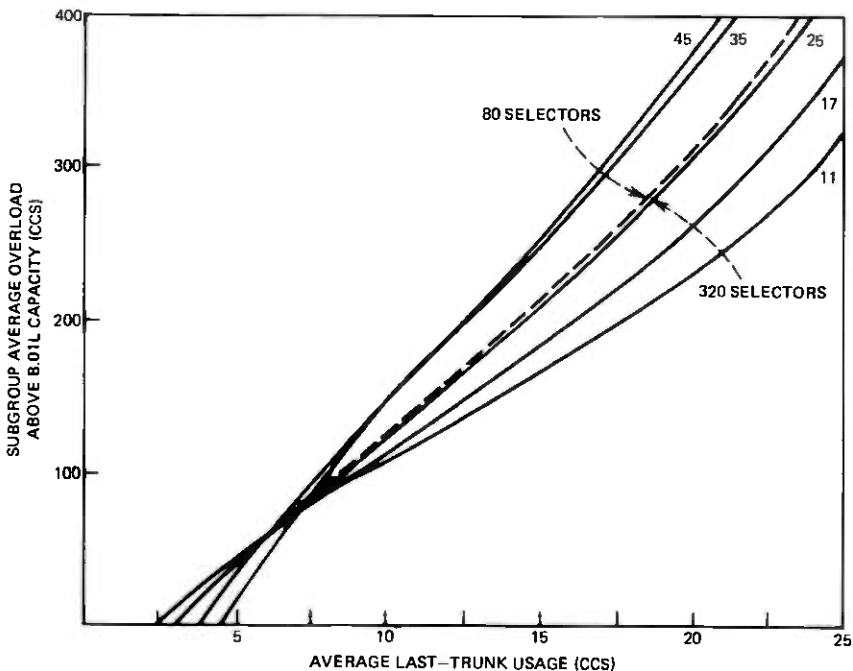


Fig. 4—Subgroup average overload versus average last-trunk usage for different graded multiple configurations (non-ROTS accessing) with low day-to-day variation in offered load.

time call). Figure 2 shows that last-trunk-usage data provide a good indication of subgroup performance, or blocking level. The L<sub>TU</sub>-blocking relation is somewhat dependent on the number of trunks in the grading, but for a given number of trunks, is generally not very sensitive to the number of accessing selectors. Because of this insensitivity, selector dependence was not studied in detail. Note that Fig. 3 uses the same data as Fig. 2, but relates average L<sub>TU</sub> and number of trunks in the grading for fixed average blocking levels.

The difference in offered load from that required for B.01L, a frequently used objective in  $S \times S$  systems, is plotted against average L<sub>TU</sub> in Fig. 4 for the same grading sizes as in Figs. 2 and 3. (The notation B.XXXV means that "Erlang-B" assumptions were used, that the blocking probability for no day-to-day variation or the average blocking probability for results with day-to-day variation is O.XXX, and that V indicates the amount of day-to-day variation with V blank for no day-to-day variation and L, M, or H for low, medium, or high day-to-day variation, respectively.) The curves in Figs. 2 and 3 show that the subgroup overload increases in an approximately linear fashion with L<sub>TU</sub>, up to a blocking of roughly B.10L.

Again, results are not very sensitive to the number of selectors. However, errors in offered load or subgroup overload estimates may arise if certain service-affecting problems exist, but are unknown; these will be discussed in Section IV.

As mentioned, the results indicate that curves of blocking vs L<sub>TU</sub>, constant blocking curves for L<sub>TU</sub> vs the number of trunks, and subgroup overload vs L<sub>TU</sub> are not strongly dependent upon the number of selectors that access the grading. Consequently, the general problem of studying all 155 standard combinations of selectors and subgroup trunk patterns found in the Bell System was simplified by ignoring selector dependence and considering only the different grading configurations. Note that the relationship of L<sub>TU</sub> to offered load, in contrast to the overload in CCS, is somewhat dependent upon the number of selectors accessing the graded multiples; this occurs because the capacities of the gradings are dependent on the number of accessing selectors.<sup>1</sup>

### III. EFFECTS OF ROTTS ON L<sub>TU</sub> PROCEDURES

Rotary out-trunk switches (rotts) are used in step-by-step systems to concentrate traffic from several graded multiples, hereafter called the access subgroups, onto a single outgoing trunk group, whose occupancy is higher than those of the access subgroups. The model of traffic flow in a graded multiple used in Section II is not appropriate in the presence of rotts for the reasons described. rotts access subgroups are generally engineered at one-tenth the blocking desired for the entire rotts system to ensure adequate access to the outgoing trunks. A representative local rotts configuration is shown in Fig. 5 for  $m$  access subgroups (10-trunk, full-access subgroups in this case) going to  $n$  rotts subgroups, each consisting of about 20 to 30 switches. The trunks from the access subgroups are spread across the rotts subgroups according to specified patterns to distribute traffic across the rotts trunks and to provide access from a given selector to the several rotts subgroups. If the number of outgoing trunks per rotts subgroup is less than 21 (or 22 in toll groups), the outgoing trunks from each rotts subgroup may be multiplied to adjacent subgroups.

In local rotts groups, approximately 40 percent of the trunks in the rotts access subgroups are wired directly to the outgoing trunks, bypassing the rotts switches. Thus, certain outgoing trunks can be accessed either directly from trunks in the rotts access subgroups as well as indirectly through a rotts switch. If the latter occurs, the directly linked trunk in the rotts access subgroup is made busy to prevent a second call from seizing the outgoing trunk. Subsequent calls arriving at the access subgroup that find a directly linked trunk busy will use trunks higher in the hunting order (closer to the last trunk).

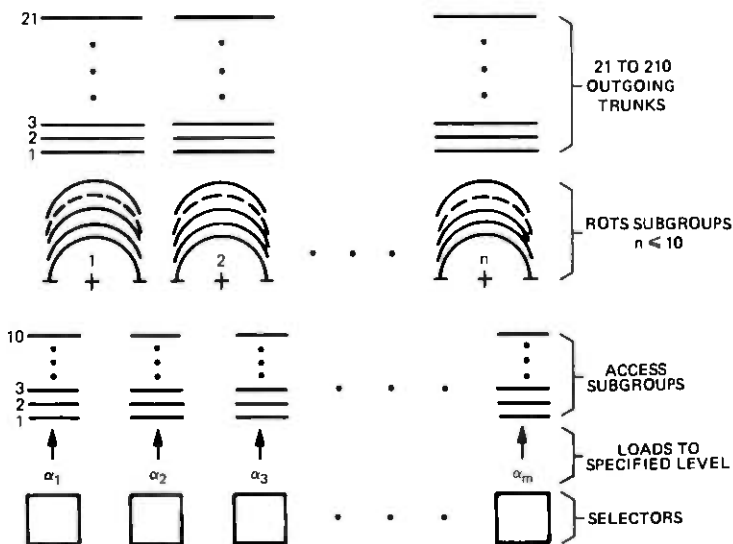


Fig. 5—Representative rors group configuration.

In addition, if all outgoing trunks in a ROTS subgroup are busy, all idle ROTS switches in that subgroup are made busy. This has the combined effect of forcing traffic higher in the access gradings and, if such a switch is connected to the last trunk of an access subgroup, of generating busy-back (non-call carrying) usage on that trunk. Any call searching for an idle trunk, which progresses to the last-choice trunk and finds the last-choice trunk busy from either type of usage, is blocked.

Consequently, the access gradings must carry the actual offered load plus the induced busy-back load. Since any calls that are blocked in the ROTS system receive reorder tone from the selectors of the access subgroups, the blocking observed on the access subgroups equals the system blocking, even though the access subgroups are usually engineered at one-tenth the desired system blocking. In addition, the intricate access arrangement results in significant interaction between the traffic parcels offered to the different access subgroups. The result is that the performance of a subgroup is influenced by its own offered load, the congestion level on the outgoing trunks, and the performance levels of the other access subgroups.

Therefore, it was not clear whether the relationships between LTV and blocking shown in Section II applied in the presence of ROTS. To determine this, a computer simulation of ROTS configurations modeled by Neal was studied.<sup>3</sup> The traffic assumptions of the graded multiple simulation model described in Section II are applicable here.

For the different grading patterns and different ROTS configurations,

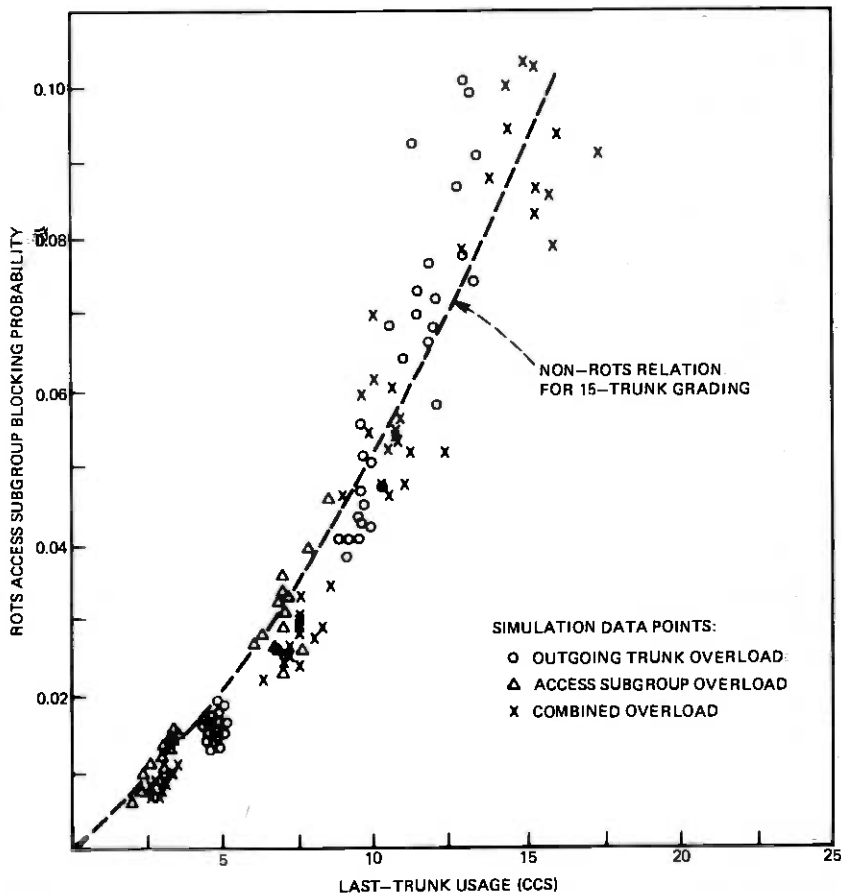


Fig. 6—rots access subgroup blocking versus last-trunk usage for rots group of 15 subgroups of 40/15 with up to 135 outgoing trunks and no day-to-day variation in offered load—general overloads.

it was found from simulation that approximately the same relationships between LTU and blocking apply as when the graded multiples do not access rots, giving acceptable estimates up to ten-percent blocking. Figure 6 shows a curve which relates LTU and blocking for non-rots subgroups, as well as data points from simulation studies of a configuration with 15 access subgroups of 15 trunks each and up to 135 outgoing trunks; the offered loads to the subgroups were equal (or balanced). By varying the offered load and the number of outgoing trunks, arrangements were investigated in which the access subgroups were under-engineered, as well as situations where the outgoing trunk group was under-provided. The data points clustered about the non-rots curve, for blocking levels up to about B.10. Significant

differences between the data points and the curve occur above ten-percent blocking because of interactions caused by busy-back usage.

These ROTS, non-ROTS comparisons are based upon *no* day-to-day variations since substantially more computer time would be required to study *low* day-to-day variations explicitly. However, the relative comparisons still hold for *low* day-to-day variations, and, thus, Fig. 2 can be used to estimate the average blocking of subgroups which access ROTS.

The same non-ROTS curve is shown in Fig. 7, but the data points represent ROTS simulation results where the offered loads to the subgroups are unequal (imbalanced). In this case, the data points were more clustered about the non-ROTS curve than in Fig. 6. These effects were confirmed for additional ROTS configurations of 11-, 21-, 25-,

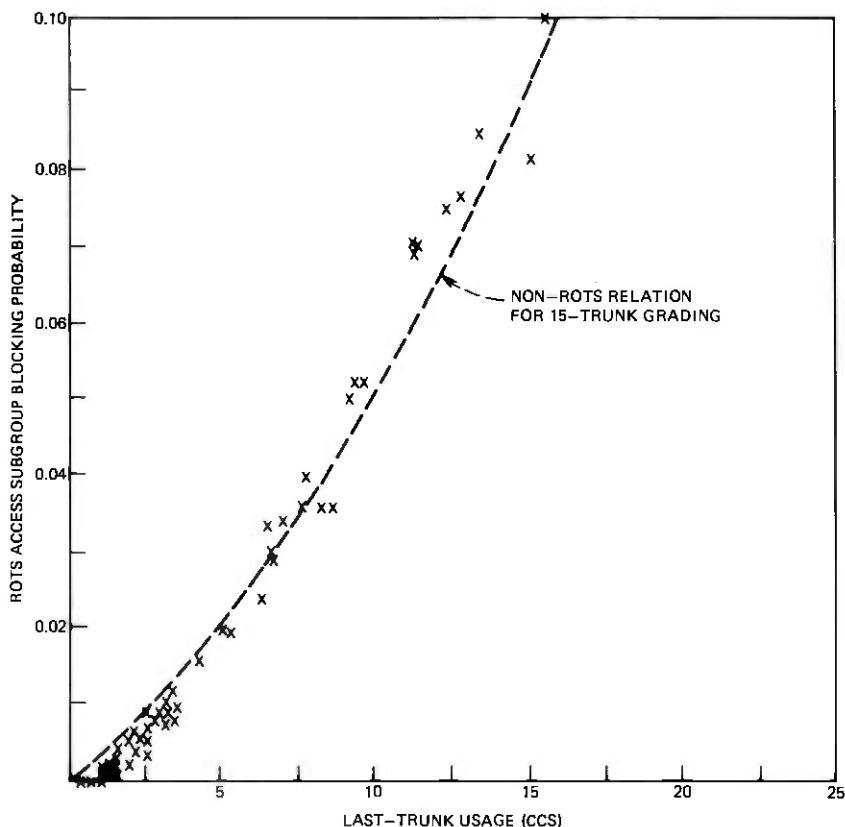


Fig. 7—rots access subgroup blocking versus last-trunk usage for ROTS group of 15 subgroups of 40/15 with 105 outgoing trunks and no day-to-day variation in offered load—imbalanced loads in access subgroups.

35-, and 45-trunk subgroups with between 34 and 210 outgoing trunks, demonstrating that the LRU-blocking relation of Section II could apply as well to ROTS configurations under a wide variety of conditions. An important feature is that the LRU measurement monitors the blocking of the access subgroups, which is, in fact, *equal to* the blocking for the entire configuration, the quantity of interest from a service standpoint. The impact of the scatter in ROTS data points on blocking estimates is discussed in Section V.

It is possible to measure the actual last-trunk call usage, excluding busy-back usage. This procedure, examined via simulation, did not give as good agreement to the non-ROTS LRU-blocking relations for general overloads, in that this type of overload affects the call usage on the last trunk for a given blocking level. The majority of points in the scatter diagram of Fig. 8 for access subgroups of 15 trunks fall

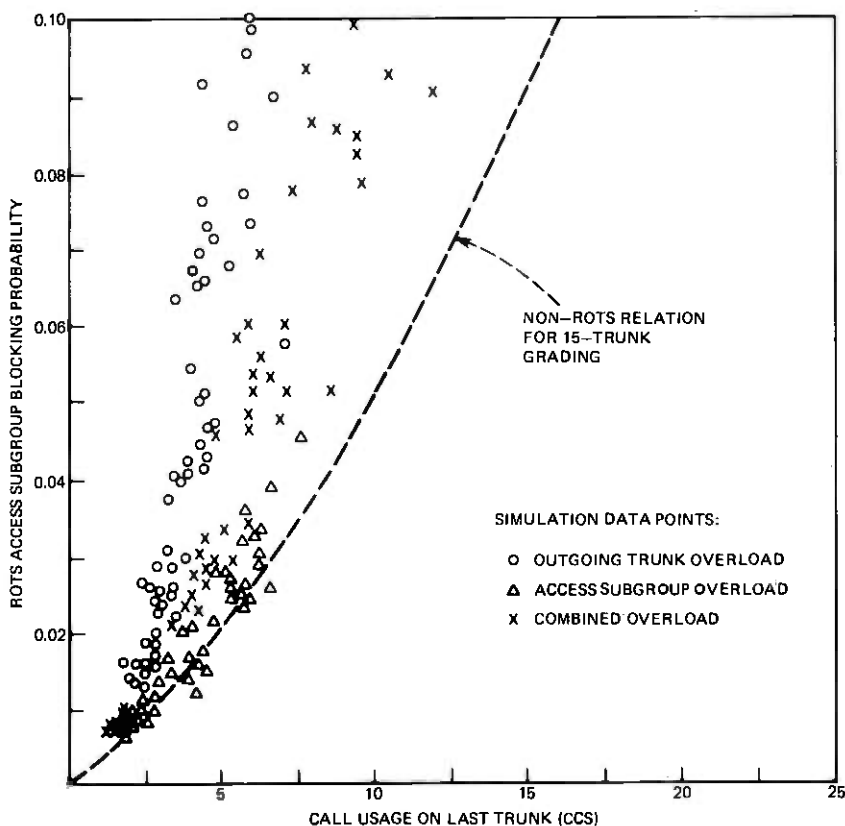


Fig. 8—rots access subgroup blocking versus call usage on last trunk (excludes busy-back usage) for ROTS group of 15 subgroups of 40/15 with up to 135 outgoing trunks and no day-to-day variation in offered load-general overloads.

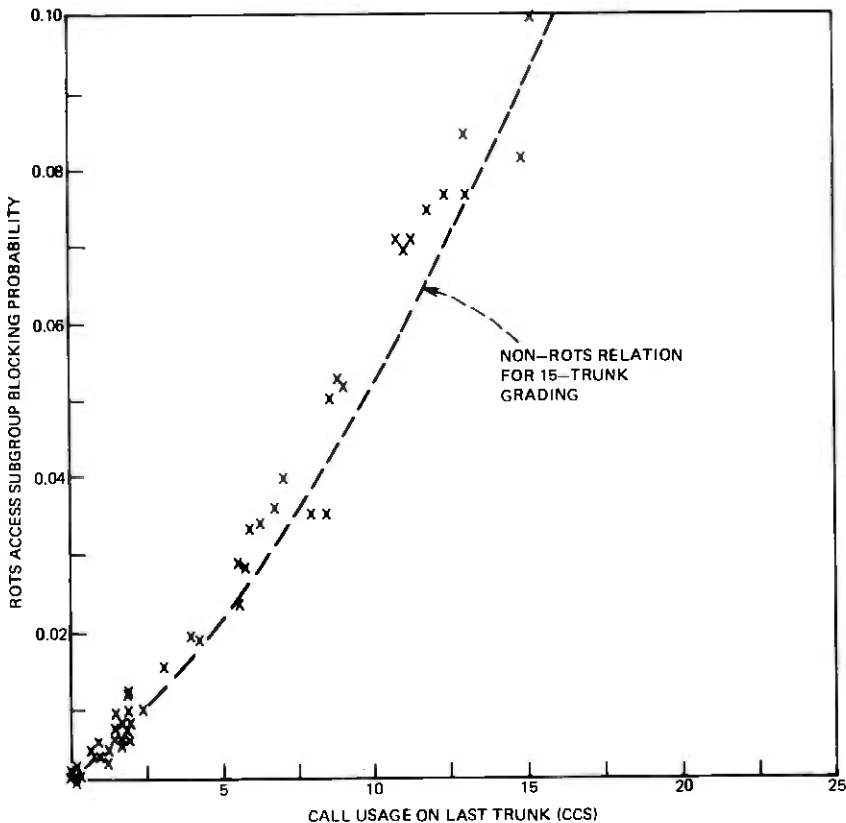


Fig. 9—rots access subgroup blocking versus call usage on last trunk (excludes busy-back usage) for rots group of 15 subgroups of 40/15 with 105 outgoing trunks and no day-to-day variation in offered load—imbalanced loads in access subgroups.

to the left of the non-rots relation for a 15-trunk subgroup. There was less disagreement for the case of load imbalances in accessing subgroups. Figure 9 shows that the scatter diagram for 15-trunk subgroups follows the corresponding non-rots relation, but that the simulation points generally fall to the left of the curve, implying a small bias. Again, similar results were observed for both general overloads and imbalances in simulating other rots configurations.

Last-trunk-busy (LTB) registers on graded subgroups are wired to exclude made-busy counts. Thus, the results in Figs. 8 and 9 also apply to LTB counts in the presence of rots, where the abscissa would be measured in LTB registrations rather than call usage on the last trunk. Notice that reconnecting the LTB register to include busy-back effects complicates data interpretation, since it appears difficult to estimate the correct mean holding time when busy-back usage occurs.

While the average LTR-blocking relations of Figs. 2 and 3 provide acceptable average blocking estimates for ROTS configurations, the subgroup average overload-LTR relation of Fig. 4 does not always apply. Not only is it difficult to accurately estimate the magnitude of the overload, but whether the overload occurs in the access subgroups, the outgoing trunk group, or both is not evident. Once the LTR procedure detects blockages, additional measurements must be taken to determine the cause of the blockage. If the outgoing trunk group is adequately engineered, as determined from total carried load or all-trunks-busy measurements, the access subgroup is limiting; in this case, Fig. 4 can be used to estimate the subgroup overload. If the outgoing trunk-group capacity is limiting and additional trunks are added, additional LTR measurements should be taken to see if the access subgroup capacity is still sufficient after augmenting the outgoing trunk group.

In summary, the basic LTR-blocking relations apply to ROTS configurations, although some moderate additional estimation uncertainty arises from the scatter shown in Figs. 6 and 7. Thus, the LTR procedure appears to be an acceptable performance-measurement tool, even though it alone cannot determine the source of the congestion problem. An additional measurement on the outgoing trunks is needed to decide what corrective action is required for a congested ROTS configuration.

#### IV. STEP-BY-STEP SERVICE-AFFECTING PROBLEMS

##### 4.1 Overview

LTR procedures can be used to detect several service-affecting problems, namely: general overloads, load imbalances, and out-of-service trunks. In each case, the problem is described and how LTR measurements are effective in detecting the problem is shown; the ability of carried load or last-trunk-busy measurements to detect the problem is also discussed. First, a general understanding of the principles used in engineering  $S \times S$  subgroups is needed.

Consider a typical stage in a  $S \times S$  train (Fig. 10), where the incoming traffic load is directed to  $n$  groups of selectors. Each selector group has access to a set of trunks on each level. In practice, the selector grouping for different levels may not be identical. Two basic assumptions in  $S \times S$  engineering are: (i) incoming traffic is distributed equally between selector groups (i.e.,  $L_1 = L_2 = \dots = L_n$ ) and (ii) each selector group offers the same proportion of the incoming traffic to a given level  $j$  (i.e.,  $a_{1j} = a_{2j} = \dots = a_{nj}$ ). As a result, all subgroups on a given level generally have the same number of trunks. Based on these assumptions, we need only measure the total carried

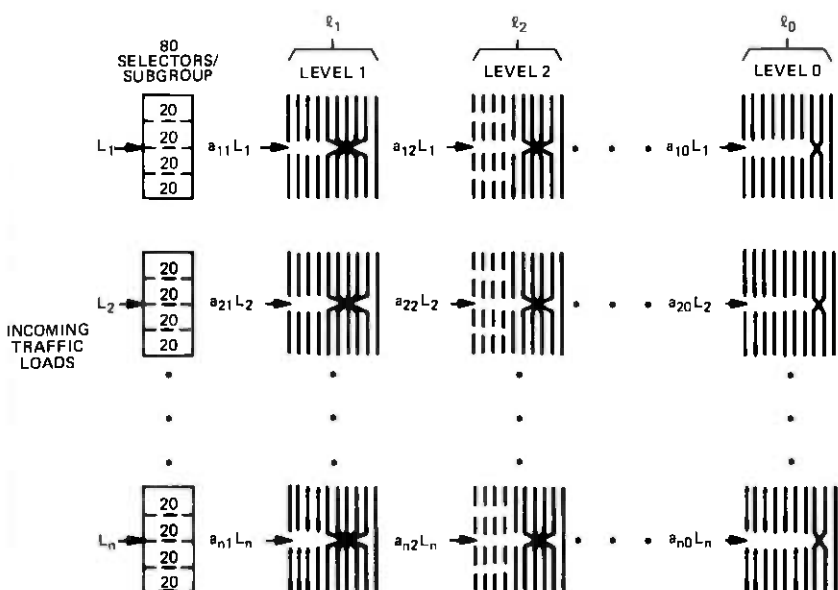


Fig. 10—Step-by-step provisioning and monitoring problems: aggregate measurements of total carried loads  $l_i$ .

load on all trunks on a level (e.g.,  $l_1$ ) to estimate the carried load for each subgroup (e.g.,  $l_1/n$ ) and to determine the number of trunks required to meet a stated service objective.

#### 4.2 General overloads

A general overload occurs when all subgroups on a level have excessive blocking, as indicated by comparing the LTU values with a threshold determined from Fig. 2. The amount of overload on each subgroup can be determined from Fig. 4 if the subgroups do not access ROTS. If the subgroups access ROTS, then additional measurements, such as outgoing trunk carried load or all-trunks-busy counts on the ROTS subgroups, are required to determine if the blockage arises in the access subgroups or the outgoing trunks.

Carried-load measurements on subgroups within a  $S \times S$  train are not commonly made because of the excessive number of measurement leads required, but are usually made on interoffice trunks. Such load measurements should detect a general overload in the non-ROTS case and in the ROTS case only if the problem is insufficient outgoing trunks. Last-trunk-busy registers, although not generally available, should indicate overloads, assuming that the correct mean holding-time is used and that the last trunk is in service. With ROTS, LTB counts are limited by the effect described in Section III.

### 4.3 Load Imbalances

Load imbalances arise when the incoming loads per selector vary over a wide range (e.g., trunks from No. 4A crossbar or  $S \times S$  offices) and the trunks are not uniformly distributed across selector groups, or trunks from different offices, which exhibit different calling patterns to different levels, are not well distributed. In either of these cases, the traffic offered to a level is not the same for each selector group (e.g.,  $a_{1j}L_1 \neq a_{2j}L_2 \neq \dots \neq a_{nj}L_n$ ), causing some subgroups to be overloaded while others are underloaded. Imbalances lead to higher blocking to selected incoming trunks as well as an increase in the average congestion across all trunks.

Last-trunk-usage procedures effectively detect blockages arising from load imbalances between subgroups, since the congestion level of each subgroup is individually monitored and recorded. This results in the specific identification of congested subgroups for corrective action.

In some cases, particularly when the larger gradings are used, balance within a grading may become a problem. Measuring the L<sub>TU</sub> is also effective here. This follows both from the flatness of the B.01L curve and from the significant spread between the curves in Fig. 3. To illustrate, consider a 45-trunk grading. From Fig. 3, we interpret an average L<sub>TU</sub> of 4.5 CCS as about one-percent average blocking under the assumption that the offered load is balanced across the individual groups of first-choice trunks (legs) of the graded multiple. Suppose the maximum imbalance occurs, i.e., all traffic is offered to only one leg and the remaining receive no calls. In this case, only ten of the 45 trunks carry any traffic; the observed average blocking would be about 2.5 percent (average L<sub>TU</sub> of 4.5 CCS on ten trunks). Thus, if the L<sub>TU</sub> is controlled so that the indicated average blocking for a 45-trunk subgroup with balanced loads is about one percent, no parcel of traffic will see more than 2.5-percent average blocking. The difference between this value and the average blocking estimate, smaller when less extreme types of imbalances occur and when the subgroup has fewer than 45 trunks, is important only when a specific group of incoming trunks is focused on an overloaded leg. If incoming trunk groups are spread across the legs, each group of customers would experience about the average blocking (across legs) for the subgroup; this average blocking is accurately estimated by the L<sub>TU</sub> procedure. Thus, the L<sub>TU</sub> procedure provides reasonable control over imbalances among the legs, although it cannot assure maximum equipment utilization. However, the estimates of subgroup average overload shown in Fig. 4 always exceed the true value in the presence of imbalances within a subgroup.

Carried-load measurements are commonly obtained on interoffice trunk groups, but are generally aggregated across all subgroups on a level for the non-ROTS case or are obtained on the outgoing side of the ROTs switches when ROTs are used. In both cases, these composite carried-load measurements cannot detect imbalances, since the carried load actually decreases as the imbalance increases. As before, LTB registers are capable of detecting imbalances although they are not usually available in the field.

#### **4.4 Out-of-service trunks**

Out-of-service trunks that lead to an increase in subgroup congestion can be detected by the LTV procedure. An out-of-service trunk that does not lead to undesirable blocking levels (if the subgroup's offered load is sufficiently below engineered capacity so that loss of a trunk has no service impact) would not be detected by the LTV procedure. The shallow slope of the B.01L curve of Fig. 3 results in the average blocking estimate being insensitive to a modest number of made-busy trunks. Thus, the LTV procedure can detect such blockage, but not indicate the cause of the blockage (i.e., overload, imbalance within the subgroup, or made-busy trunks). With out-of-service trunks, the overload estimate of Fig. 4 always exceeds the true overload. Measurements of total-carried-load may not indicate a service problem caused by out-of-service trunks, particularly if the load measurements are aggregated across subgroups.

#### **4.5 Equipment malfunctions**

Malfunctions leading to abnormally short holding times (the "killer trunk" phenomenon) cannot be located with the LTV procedure.

### **V. UNCERTAINTIES IN BLOCKING AND LOAD ESTIMATES**

The uncertainty in average blocking estimates is important in deciding when corrective action is required. The uncertainty in these estimates arises from three effects: variations in single-hour LTV measurements, day-to-day variations of offered load, and approximations used in the LTV procedure. Estimates of blocking and offered load from single-hour LTV data cannot be used, because they have a large coefficient of variation (*cv*); this is defined as the standard deviation to mean ratio of a random variable and indicates the "spread" of values of the variable about its average. Consequently, LTV data must be averaged over several hours to provide reliable estimates. This section shows that last-trunk-usage procedures using time-consistent busy-hour measurements can detect moderate to severe problems with acceptable confidence in five days whereas at least 20 days are needed for provisioning studies.

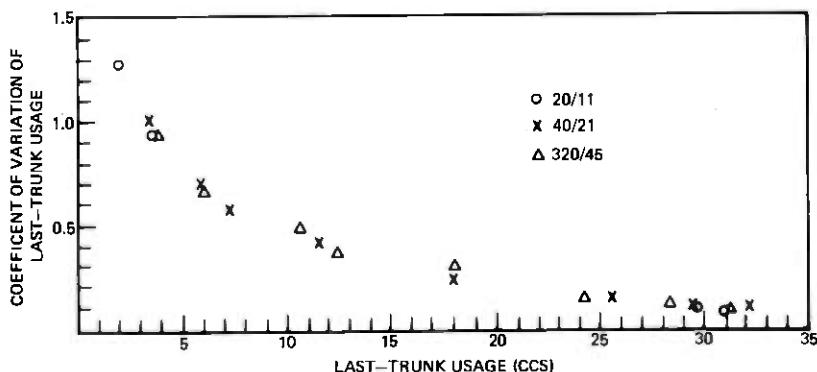


Fig. 11—Simulation points of coefficient of variation of single-hour last-trunk usage for several graded multiple configurations with no day-to-day variation in offered load.

For low subgroup blocking (B.01<sub>-</sub>), the cv for a single-hour LTRU measurement is approximately one. The cv decreases to roughly 0.1 for subgroup blocking above B.10<sub>-</sub>. Simulation results for subgroups with 11, 21, and 45 trunks indicate that the cv of an LTRU measurement is not strongly dependent upon grading size or pattern for Poisson traffic with no day-to-day variations (Fig. 11). The effects of day-to-day variation in the offered load and discrete sampling of the last-trunk usage on estimates of blocking and load were studied using procedures formulated by Neal and Kuczura,<sup>4</sup> Hill and Neal,<sup>5</sup> and Hill.<sup>6</sup> The standard deviation of the average blocking estimate for all subgroups (with blocking near B.01L) is approximately 0.01 for LTRU values averaged over five hours (typically the same hour on five consecutive days). Thus, if five measurements give a blocking estimate greater than B.02L, we can be 84-percent confident that the true blocking is greater than B.01L. This result assumes a statistical model where the error is normally distributed with mean zero. Hence, LTRU measurements during the busy hour enable relatively quick (i.e., five days) detection of subgroups with moderate to severe service-affecting problems. If five measurements give a blocking estimate less than B.02L, but greater than B.01L, the adjustment of performance levels to a B.01L objective should only be based on longer study intervals (e.g., 20 days) and a demonstrated practical need for such adjustments.

Five days of data are not sufficient to accurately determine the number of trunks required to meet a given blocking objective. With five days of data, the standard deviation in the average offered load estimate is about 40 CCS for a 21-trunk subgroup; thus, we can be

68-percent confident that the true offered load will be within 40 CCS of the estimated offered load, which corresponds to a possible deviation of two to three trunks from the number required to precisely meet the objective. The 68-percent confidence interval can be reduced to within one trunk by taking at least 20 days of data. It would seem that this is the minimum number of days needed for any provisioning study.

ROTS subgroups are subject to approximately the same level of statistical variations as non-ROTS subgroups. However, the scatter of Fig. 6 indicates that there will be some uncertainty introduced by using non-ROTS LTU-blocking relations for ROTS subgroups. Fortunately, the effect of possible approximation bias or additional variance is negligible when compared to the estimation error arising from other sources (measurement variation and day-to-day variations) during a five-day study.

## **VI. APPLICATIONS**

### **6.1 Types of trunks**

The preceding discussions have assumed that the graded subgroups were either connecting intraoffice selector stages or were one-way interoffice trunks. For two-way interoffice trunks, the LTU method applies to all trunk groups with ROTS, since the ROTS isolate the effects of the trunk selection method (whether from common-control or  $S \times S$  equipment) at the far end from the LTU measurement. The LTU method is not applicable where selector subgroups directly access (instead of going through ROTS) two-way interoffice trunks, unless, at the far end, the trunks are chosen in the same hunting order as at the near end. For trunk groups where the procedure is not applicable, total carried-load measurements should be used, since these are typically small groups that are not susceptible to load imbalance problems because they are full or nearly full-access groups.

### **6.2 Measurement equipment**

There is a wide variety of measurement equipment available for collecting LTU data. However, some Bell System measurement equipment found in small  $S \times S$  switching entities such as community dial offices (CDOs) may not be ideal for LTU measurements. These electro-mechanical recorders have a relatively small number of output registers and are configured to report usage only on a grouped basis rather than an individual trunk basis. Last-trunk-usage measurements, requiring only one input lead per graded multiple, would utilize this equipment inefficiently assuming that a sufficient number of output registers were available. For some cases an option to record usage on individual

trunks could be added. In general, a more viable alternative would be to use other measurement equipment that is suitable for the collection of LTR data.

### 6.3 Data collection and analysis

For each level under study at a particular selector stage, last-trunk-usage data should be collected during the time-consistent level-congestion busy hour; i.e., the time-consistent hour in which the total LTR for the level (obtained by summing over all subgroups on the level) is greatest. This hour can be determined by collecting data in several candidate hours during a study period and then choosing the time-consistent hour in which the total LTR for the level is greatest. In some cases, it may be desirable to analyze LTR data outside of the time-consistent level-congestion busy hour to detect focused overloads which may occur in other time periods. Of course, the data should be collected in the busy season to maximize the effectiveness of the measurement.

For the study period, the average busy-hour LTR for each subgroup can be calculated and used with Table I to estimate that subgroup's average blocking. This table, related to Fig. 2, provides a summary of the average last-trunk-usage in CCS at increasing blocking levels (B.005L to B.10L) for bands of subgroup trunk sizes. A last trunk that continually appears as 36 CCS is most likely to be out-of-service.

For a five-day "quick test," any subgroup which exceeds B.02L is a candidate for corrective action. For 20 days of data, subgroups exceeding B.01L should be considered for correction. Lower blocking thresholds may be appropriate outside the busy season. In all cases, additional LTR measurements should be collected after any corrective action to ensure that the blockage is eliminated.

Table I—Average value of last-trunk usage in CCS for different blocking levels \*

Number of Trunks in Subgroup	Average Blocking (Percent)					
	0.5	1	2	3	5	10
4 to 9	0.5	1.5	2.5	3.5	5.0	10.0
10 to 14	1.1	2.0	3.5	5.2	7.8	13.0
15 to 19	1.4	2.5	4.6	6.3	9.3	15.5
20 to 24	1.6	3.0	5.3	7.2	10.6	17.2
25 to 29	1.8	3.2	5.7	7.8	11.5	18.2
30 to 34	1.9	3.6	6.2	8.5	12.4	19.5
35 to 39	2.1	3.8	6.7	9.1	13.1	20.5
40 to 45	2.4	4.2	7.3	9.8	14.1	21.7

\* Assumes low day-to-day variations.

#### 6.4 Corrective action

When LTU measurements detect congestion, additional investigation is necessary to find the cause of the blockage. Common problems, such as general overloads and load imbalances, were discussed in Section IV. Estimates of subgroup overload (in CCS) for a given average last-trunk-usage may be useful in determining the degree of corrective action for all major problems except general overloads on ROTS groups and maintenance-associated phenomena.

### VII. SUMMARY AND CONCLUSIONS

The last-trunk-usage procedures are an application of the general concept of observing a subset of the elements of a traffic system to estimate the performance of the entire system. The procedures are effective because all Bell System standard gradings have a common last-choice trunk and because the load carried on that trunk is directly related to the traffic congestion in the subgroup. This provides a direct measure of subgroup performance, since general overloads and imbalances between subgroups or within subgroups, as well as possible made-busy trunks that have significant impact upon service, cause increases in a subgroup's LTU. In fact, the average load carried on the last-choice trunk is directly related to the service level, and in the range of primary interest (B.01L to B.10L) is not very dependent upon the cause of the degradation. These results apply to both non-ROTS and ROTS applications, although in the latter case additional measurements are required on the outgoing trunks to completely diagnose a problem detected by LTU measurements.

A subgroup's mean blocking is estimated from the average of the last-trunk-usage measurements in the level busy-hour; an estimate of at least B.02L using only five days of data indicates that the subgroup has an average blocking greater than B.01L with 84-percent confidence. In addition, the cost of installing the measurement equipment and test leads is held to a minimum since only one lead is required per subgroup. Hence, the method has the combined advantage of rapid detection of subgroups with service-affecting problems and ease of implementation.

### VIII. ACKNOWLEDGMENTS

The authors are indebted to S. R. Neal for many helpful discussions and suggestions throughout the study. We also thank J. S. Hall for programming support and D. W. Hill for consultation.

### REFERENCES

1. M. M. Buchner, Jr., and S. R. Neal, "Inherent Load-Balancing in Step-by-Step Switching Systems," *B.S.T.J.*, 50, No. 1 (January 1971), pp. 135-165.

2. R. I. Wilkinson, "A Study of Load and Service Variations in Toll Alternate Route Systems," Proc. of the Second International Teletraffic Congress, The Hague, July 7-11, 1958, Document No. 29.
3. S. R. Neal, private communication.
4. S. R. Neal, and A. Kuczura, "A Theory of Traffic-Measurement Errors for Loss Systems with Renewal Input," B.S.T.J., 52, No. 6 (July-August 1973), pp. 967-990.
5. D. W. Hill, and S. R. Neal, "Traffic Capacity of a Probability-Engineered Trunk Group," B.S.T.J., 55, No. 7 (September 1976), pp. 831-842.
6. D. W. Hill, private communication.

## Contributors to This Issue

**Jacques A. Arnaud**, Dipl. Ing., 1953, Ecole Supérieure d'Electricité, Paris, France; Docteur Ing., 1963, Docteur Science, 1972, University of Paris; Assistant at E.S.E., 1953-1955; CSF, Centre de Recherche de Corbeville, Orsay, France, 1955-1966; Warnecke Elec. Tubes, Des Plaines, Illinois, 1966-1967; Bell Laboratories, 1967—. At CSF, Mr. Arnaud was engaged in research on high-power traveling-wave tubes and noise generators. He is presently studying the propagation of optical waves. Senior Member, IEEE; Member, Optical Society of America.

**Harry W. Astle**, A.A.S., 1966, Hartford State Technical College, Bell Laboratories, 1966—. Mr. Astle has worked with optical gas lenses and is presently engaged in the fabrication and evaluation of optical fibers.

**E. G. Bowen**, Assoc. Deg. (E.E.), 1963, Vermont Technical College, B.S. (E.E.), 1971, Newark College of Engineering, Bell Laboratories, 1963—. Mr. Bowen has worked on analog-to-digital magnetic coders, plasma display panels, and coding of video signals.

**Leonard G. Cohen**, B.E.E., 1962, City College of New York; Sc.M., 1964, and Ph.D. (Engineering), 1968, Brown University; Bell Laboratories, 1968—. At Brown University, Mr. Cohen was engaged in research on plasma dynamics. At Bell Laboratories, he has concentrated on optical fiber transmission studies. Member, IEEE, Sigma Xi, Tau Beta Pi, Eta Kappa Nu.

**Richard M. Derosier**, A.A.S.E.E., 1967, Hudson Valley Community College; Bell Laboratories, 1967—. Initially, Mr. Derosier's work concerned the fabrication and development of GaAs injection diodes. He is also associated with studies of mode conversion and radiation losses from various dielectric waveguides. He has worked with fiber joining techniques and polishing of fiber samples for interferometric work. Currently he is working on a transmission technique for the determination of fiber index profiles.

**Ivan P. Kaminow**, B.S.E.E., 1952, Union College (NY); M.S.E., 1954, University of California, Los Angeles; A.M., 1957, Ph.D., 1960, Harvard University; Bell Laboratories, 1954—. Mr. Kaminow has done research on microwave antennas, ferrites, ferroelectrics, non-

linear optics, raman scattering, electrooptic devices and optical fibers. Fellow, IEEE, APS, OSA. Author, *Introduction to Electrooptic Devices*; co-editor, *Laser Devices and Applications*.

**Barbara R. LaCava**, B.A. (Mathematics), 1965, St. Mary-of-the-Woods College; M.S. (Mathematics), 1969, Stevens Institute of Technology; Bell Laboratories, 1965—. Ms. LaCava has worked on traffic problems for ESS and electromechanical systems as well as specifying trunk engineering algorithms for BIS. She is currently engaged in traffic capacity studies for the No. 4A crossbar toll switch.

**Dietrich Marcuse**, Diplom Vorpruefung, 1952, Dipl. Phys., 1954, Berlin Free University; D.E.E., 1962, Technische Hochschule, Karlsruhe, Germany; Siemens and Halske (Germany), 1954-1957; Bell Laboratories, 1957—. At Siemens and Halske, Mr. Marcuse was engaged in transmission research and studying coaxial cable and circular waveguide transmission. At Bell Laboratories, he has been engaged in studies of circular electric waveguides and work on gaseous masers. He spent one year (1966-1967) on leave of absence from Bell Laboratories at the University of Utah. He is presently working on the transmission aspect of a light communications system. Mr. Marcuse is the author of three books. Fellow, IEEE; member, Optical Society of America.

**William D. Miller**, B.S. (E.E.) and M.S. (E.E.), 1971 and 1973, Pennsylvania State University; Bell Laboratories, 1973—. Mr. Miller has worked on problems related to measuring the performance of step-by-step switches and proposals for enhancing special communications networks. He is currently engaged in planning for new network services. Member, IEEE, Eta Kappa Nu, Phi Kappa Phi.

**F. W. Mounts**, E.E., 1953, M.S., 1956, University of Cincinnati; Bell Laboratories, 1956—. Mr. Mounts has been concerned with research in efficient methods of encoding pictorial information for digital television systems. Member, Eta Kappa Nu; Senior Member, IEEE.

**Arun N. Netravali**, B. Tech. (Honors), 1967, Indian Institute of Technology, Bombay, India; M.S., 1969, and Ph.D. (E.E.), 1970, Rice University; Optimal Data Corporation, 1970-1972; Bell Laboratories, 1972—. Mr. Netravali has worked on problems related to filtering, guidance, and control for the space shuttle. At Bell Laboratories, he has worked on various aspects of signal processing. Member, Tau Beta Pi, Sigma Xi.

Herman M. Presby, B.A., 1962, and Ph.D., 1966, Yeshiva University; Research Scientist, Columbia University, 1966-1968; Assistant Professor Physics, Belfer Graduate School of Science, Yeshiva University, 1968-1972; Bell Laboratories, 1972—. Mr. Presby is engaged in studies on the properties of optical fiber waveguides.

Bernard Yaged, Jr., B.S., M.S., 1964; E.E., 1965; Massachusetts Institute of Technology; Ph.D. (OR), 1971, Brooklyn Polytechnic Institute; Bell Laboratories, 1965—. Mr. Yaged has worked on projects related to communications facilities network planning, traffic network performance measurements, and the economics of project evaluation and introduction of new technology. He is presently engaged in financial modeling and analysis projects. Associate Editor, Networks. Member, ORSA, Institute of Management Sciences, American Finance Association.



# Abstracts of Papers by Bell System Authors Published in Other Journals

## CHEMISTRY

**The Chemistry of Pd-Sn Colloid Sensitizing Processes.** R. L. Cohen and R. L. Meek, *J. Colloid Interface Sci.*, *55* (1976), pp. 156-162. This research uses Rutherford backscattering and Mössbauer spectroscopy to characterize the catalytic surface produced by commercial "sensitization" processes used for electroless plating of plastics. The active agent is shown to be a colloidal Pd-Sn alloy with a particle size of about 20 Å.

**Dissociative Excitation of H<sub>2</sub>: Spectral Lineshapes and Electron Impact Cross-Sections of the Balmer Lines.** R. S. Freund, J. A. Schiavone, and D. F. Brader,\* *J. Chem. Phys.*, *64*, No. 3 (February 1, 1976), pp. 1122-1127. The Balmer lines of H, when produced by electron impact dissociative excitation of low pressure H<sub>2</sub>, are much broader than the Doppler width of thermal H atoms. Excitation cross-sections show structure as a function of energy. This helps to identify two groups of dissociative states. \*Work done while a participant in the Summer Research Program at Bell Laboratories in 1975.

**Sensitization with Palladium-Tin Colloids, I: Role of Rinse and Accelerator Steps.** R. L. Cohen, R. L. Meek, and K. W. West, *Plat. Surf. Finish*, *63* (1976), pp. 52-55. In the commercial "sensitization" processes used in the manufacture of printed wiring boards, a step called "acceleration" is normally used. We show that the purpose of this step is to dissolve away a layer of stannic hydroxide, which otherwise coats and passivates the catalytic sites on the surface.

**Tropospheric Halocarbons: Estimates of Atmospheric Chemical Production.** T. E. Graedel and D. L. Allara, *Atmos. Environ.*, *10* (1976), pp. 385-388. Selected thermal and photochemical atmospheric reactions have been evaluated as potential sources for the family of halocarbons recently detected in tropospheric air. Formation of CH<sub>3</sub>Cl is extremely slow and that of CCl<sub>4</sub>, CHCl<sub>3</sub>, CH<sub>3</sub>I, CH<sub>2</sub>CCl<sub>2</sub>, and the chlorinated ethylenes is negligible, implying that direct emission is responsible for the presence of these compounds.

## COMPUTING

**A Survey of Techniques for the Display of Continuous Tone Pictures on Bilevel Displays.** J. F. Jarvis, *Comput. Graph. Image Process.*, *6* (1976), pp. 13-40. Many displays are basically bilevel in nature with individual display elements, all of the same size, arranged in a rectangular array. We present a survey of processing techniques for presenting continuous tone still images on such displays. Four techniques are covered in detail while several others are covered briefly. All the techniques achieve the subjective effect of continuous tone by properly controlling only the spatial density of bilevel display states.

## ELECTRICAL AND ELECTRONIC ENGINEERING

**The Effects of Gold and Nickel Plating Thicknesses on the Strength and Reliability of Thermocompression Bonded External Leads.** N. T. Panousis and P. M. Hall, *Proc. IEEE 26th Electron. Comp. Conf.* (1976), pp. 74-79. Copper leads intended for thermocompression bonding are typically plated with Au or a combination of Ni and Au. Optimum strength and reliability with the Ni/Au system were obtained for a Ni thickness of 0.25 to 1.3 μm, a Au thickness minimum of 2.5 μm, and a Au-to-Ni ratio of  $\geq 2.5$ . For Au-plated Cu leads, acceptable bonds were obtained with 0.6 μm of Au.

**Transmission Electron Microscopy of Cross-Sections of Large Scale Integrated Circuits.** T. T. Sheng and C. C. Chang, *IEEE Trans. Electron. Dev.*, *ED-23* (June 1976), pp. 531-533. Accurate cross-sectional views of large scale integrated

circuits are useful for failure analysis and process evaluation. We have successfully prepared thin sections of finished devices cut perpendicular to the plane of the chip and examined them using transmission electron microscopy. We describe the sectioning procedure and show some cross-sectional views from memory cells of a CMOS RAM with poly-Si gates and tungsten second metal.

**Planar Isolated GaAs Devices Produced by Molecular Beam Epitaxy.** W. C. Ballamy and A. Y. Cho, *IEEE Trans. Electron. Dev.*, *ED-23* (1976), pp. 481-484. This paper reports the fabrication of low parasitic capacitance planar beam leaded mixer diodes. The material for low parasitic structure is produced by the simultaneous deposition of single crystal and polycrystalline gallium arsenide utilizing the molecular beam epitaxial process. Diodes measured in a double-balanced downconverter circuit showed a conversion loss of 5.3 dB at 51.5 GHz and 8.5 dB at 103 GHz. These devices exceed the performance of structurally identical devices fabricated on conventional n on n<sup>+</sup> material by about 2 dB.

## GENERAL MATHEMATICS AND STATISTICS

**Estimating Item and Order Information.** G. Sperling and M. J. Melchner, *J. Math. Psychol.* *15*, No. 2 (April 1976), pp. 192-213. In a common psychological procedure, a subject is presented a sequence of items and asked to recall them in order. His response is scored for items reported correctly in their correct positions (position score) and for items reported correctly independently of their position (item score). Equations are derived to estimate the effects of guessing and thereby to estimate "true item" and "true position" scores from observed scores.

## MATERIALS SCIENCE

**Compound-Glass Waveguides Fabricated By a Metal Evaporation Technique.** S. R. Nagel, A. D. Pearson, and A. R. Tynes, *J. Amer. Chem. Soc.*, *59* (January 1976), pp. 47-49. Glass fiber optical waveguide preforms consisting of a potassium silicate glass core and SiO<sub>2</sub> cladding were produced by a potassium metal evaporation technique. Fibers drawn from such preforms exhibit moderately low optical loss. The fabrication technique is described, and a representative loss spectrum is presented.

**The Deep Blue Maxixe-Type Color Center in Beryl.** K. Nassau, B. E. Prescott, and D. L. Wood, *Amer. Mineral.*, *61* (1976), pp. 100-107. Irradiation produces a deep blue color center in some natural beryl. Narrow band absorption in the ordinary ray and fading on heating or on light exposure distinguished this Maxixe-type beryl from aquamarine. Similar, but not identical, beryl was found in 1917 in the Maxixe mine in Brazil.

**Investigations of an Electrodeposited Tin-Nickel Alloy: I. Thermal Stability by Differential Thermal Analysis and X-Ray Diffraction.** J. E. Bennett and H. G. Tompkins, *J. Electrochem. Soc.*, *123*, No. 7 (July 1976), pp. 999-1003. Electrodeposited equiatomic tin-nickel is a metastable phase which transforms to a mixture of the equilibrium compounds Ni<sub>3</sub>Sn<sub>2</sub> and Ni<sub>3</sub>Sn<sub>4</sub>. The transition temperature can be a deciding factor for certain applications. DTA and XRD showed that on heating the alloy decomposed exothermally over the range 350 to 380°C with a maximum at 365°C.

**Origin of Surface Defects in Fe = Co/3%V Wire.** M. R. Pinnel, J. E. Bennett, and K. M. Olsen, *Wire J.*, *9* (April 1976), pp. 73-79. Good glass-to-metal vacuum seals are essential to the performance of remreced contacts. Surface defects in the magnetic wire at the seal caused problems. The source of the defects was traced to the rod surface finish prior to wire drawing. Methods to improve the finish were evaluated.

**Ternary Phase Relations in the Vicinity of Chalcopyrite Copper Gallium Sulfide:** M. Kokta, \* J. R. Carruthers, M. Grasso, H. M. Kasper, and B. Tell, *J. Electron. Mater.*, *5*, No. 1 (1976), pp. 69-89. Some of the ternary phase relations relevant to the growth of Cu<sub>1-x</sub>Ga<sub>1+x/2</sub>S<sub>2</sub> chalcopyrite crystals have been determined. Conditions necessary for the growth of stoichiometric crystals which are free of cupric sulfide precipitates and the associated green coloration are given. Such compositions

are necessary for the generation of luminescence in this compound. \* Work performed while at Bell Laboratories. Present address: Allied Chemical Corporation, Morristown, New Jersey.

## PHYSICS

**Chemisorption of Atomic Hydrogen on the Silicon (110)5×1 Surface (Ups and Leed).** T. Sakurai, K. C. Pandey, and H. D. Hagstrum, *Phys. Lett.*, *56A* (March 22, 1976), pp. 204-206. Chemisorption experiments show that the Si(110)5×1 surface when saturated with H leads to two distinct 1×1 phases depending on temperature during exposure. We suggest that while both phases are characterized by the saturation of surface dangling orbitals, additional hydrogen atoms chemisorbed weakly at nontetrahedral sites are present in the room temperature phase.

**Greater Surface Sensitivity of Ion Neutralization Spectroscopy with Respect to UV Photoemission Spectroscopy.** T. Sakurai and H. D. Hagstrum, *J. Vacuum Sci. Technol.*, *13* (January/February 1976), p. 196. Ultraviolet photoemission spectroscopy showed that the dangling-bond surface state disappears when the clean surface is exposed to atomic hydrogen. Chemisorbed hydrogen produces two sharp peaks in the surface density of states at -10 and -12 eV from the vacuum level, in good agreement with the recent theoretical works.

**Spectroscopic Observation of Very Low Energy Excitations in Glasses.** P. A. Fleury and K. B. Lyons, *Phys. Rev. Lett.*, *36*, No. 20 (May 17, 1976), pp. 1188-1191. A new experimental technique for high resolution, very high contrast light scattering spectroscopy has permitted the direct observation of very low energy excitations (0-1 K) in a variety of glassy solids. These excitations may be responsible for the anomalous specific heat, thermal conductivity, and acoustic absorption previously observed in glasses at very low temperatures (<1 K).

